DIRECT NUMERICAL SIMULATION OF TURBULENT DISPERSION OF BUOYANT PLUMES IN A PRESSURE-DRIVEN CHANNEL FLOW

Memòria presentada per

Alexandre Fabregat Tomàs

per optar al grau de doctor en Enginyeria Química

Tarragona, octubre del 2006

Els Professors titulars de mecànica de fluids de l'Escola Tècnica Superior d'Enginyeria Química de la Universitat Rovira i Virgili, Dr. Jordi Pallarès Curto i Dr. Ildefonso Cuesta Romeo,

Fan constar:

Que el present treball, amb títol:

Direct Numerical Simulation of Turbulent Dispersion of Buoyant Plumes in a Pressure-driven Channel Flow

que presenta en Alexandre Fabregat Tomàs per optar al grau de doctor en Enginyeria Química ha estat realitzat sota la nostra immediata direcció i que tots els resultats obtinguts són fruit dels experiments i anàlisis realitzats per l'esmentat doctorand.

I, perquè en prengueu coneixement i tingui els efectes que correspongui, signem aquesta certificació.

Tarragona, octubre del 2006

Dr. Jordi Pallarès i Curto

Dr. Ildefonso Cuesta Romeo

A Caro,
a muns pares
i, especialment, a muns iaios

Contents

Abstract

The main goal of this work is to study the turbulent heat transfer in a developed channel flow using Direct Numerical Simulations (DNS). These simulations solve explicitly all the scales present in the turbulent flow so, even for moderate Reynolds numbers, the discretization grids need to be fine enough to capture the smallest structures of the flow and, consequently, DNS demands large computational resources. The flow, driven by a mean constant pressure gradient in the streamwise direction, is confined between two smooth, parallel and infinite walls separated a distance 2δ.

The turbulent heat transport is studied for three different flow configurations. Some of them are used as benchmark results for this work. The three cases reported can be summarized as:

- case A: Scalar plume from a line source in a horizontal channel.
- case B: Mixed convection with the gravity vector aligned with the streamwise direction (vertical channel).
- case C: Buoyant plume from a line source in a horizontal channel.

In addition, preliminary results for a turbulent reacting flow in a fully developed channel are also presented in section 7.

In the case B heat flux results from a temperature difference between the channel walls. The gravity vector is aligned with the streamwise direction and the Grashof, Reynolds and Prandtl numbers are $Gr = 9.6 \cdot 10^6$, $Re_\tau = 150$ and $Pr = 0.71$ respectively. Close to the *hot* wall, buoyancy acts aligned to the flow direction imposed by the mean pressure gradient so velocities are generally increased in comparison with a purely forced convection flow. Oppositely, near the *cold* wall, buoyancy is opposed to the flow and consequently velocities are decreased.

Cases A and C are similar because in both cases a *hot* fluid is released within a *cold* background flow through a line source vertically centered in the wall-normal direction located at the inlet. The height of the source is 0.054δ. The injected *hot* fluid disperses forming a hot plume that is convected downstream between the two adiabatic walls of the channel.

The difference between cases A and C lies in the fact that for case A heat and momentum are decoupled and temperature acts as an scalar. Advection and diffusion are the only phenomena responsible for the evolution of the plume. On the other hand, in case C, buoyancy couples heat and momentum and, consequently, the plume floats drifting upward as it advances in the channel due to its lower density. In case C, the streamwise direction is not homogenous because of the coupling between heat and momentum. To guarantee developed conditions at the inlet of the channel it has been necessary to attach a buffer domain just before the computational domain. In this buffer domain, the momentum transport equations for a fully developed channel are solved with the same resolution used in the main domain.

The results of cases A and B have been used to validate the 3DINAMICS CFD code by comparison with data reported in the literature. This code is written in FORTRAN 90 and parallelized using the Message Passing Interface (MPI-CH library). It uses the second order in time Crank-Nicholson scheme to integrate numerically the transport equations which are discretized spatially using the centered second-order finite volume approach.

The analysis of averaged turbulent quantities and the contributions of the different terms of the time-averaged transport equations is used to show how buoyancy affects the turbulent transport of momentum and heat along the channel.

Finally, following a similar configuration than that of case A, a chemical reactant A released through line source reacts with a background reactant B following a second order chemical reaction with Damkhöler number of 1. Preliminary results for turbulent species transport are also included in this work.

Special attention have been devoted to the discretization of the advective terms to avoid non-realistic values of the variables because of the non-linearities of the transport equations. The conservative non-reflecting boundary conditions have been implemented at the outlet to simulate the convected outflow when the streamwise direction can not be considered homogeneous, as in case C. For homogeneous directions, periodic boundary conditions have been used.

Large grid resolutions (up to 8 million grid nodes for case C including the buffer region) demand important computational resources. A parallel Multigrid solver has substituted the previous conjugate gradient method to solve the Poisson equation in the pressure calculation. This step was the most expensive in terms of CPU costs. The Multigrid method efficiency has been compared with two different versions of the conjugate gradient approach and it has been demonstrated that this method is the most efficient in terms of CPU time although the current algorithm can be improved to enhance the scalability in multiprocessor computers.

Agraïments

El treball presentat en aquesta memòria ha estat desenvolupat dins del grup de recerca d'Experimentació, Computació i Modelització en Mecànica de Fluids i Turbulència (ECoMMFiT) adscrit al Departament d'Enginyeria Mecànica de l'Escola Tècnica d'Enginyeria Química de la Universitat Rovira i Virgili sota la direcció conjunta dels Drs. Jordi Pallarès i Ildefonso Cuesta.

Desitjo fer palès el meu immens agraïment a tots dos per haver acceptat la direcció d'aquest treball. La seva dedicació en la direcció, el constant suport i els seus coneixements i paciència han estat determinants per a dur a bon port aquesta tesi doctoral.

Voldria fer extensiva la meva gratitud vers tots els altres membres de l'equip docent, tècnic i administratiu del Departament d'Enginyeria Mecànica, especialment vers al professor Francesc Xavier Grau i als doctors Anton Vernet i Clara Salueña. L'entusisme, les dissertacions i els millors moments durant tots aquests anys els han aportat els meus companys Gabriel Usera, Guillaume Novelli, Vincent Bourdette, Marwan Hussin, Obai Younis i la resta de doctorands. La inestimable ajuda dels doctors Àngel Jiménez i Leonardo Valencia durant els meus primers anys de feina feren la tasca més fàcil i engrescadora. David Losada posà tots els seus coneixements i moltes hores en l'apartat tècnic.

La realització d'aquest treball no hagués estat mai possible sense el suport dels meus pares que sempre han estat al meu costat i m'han animat des del principi a continuar aprenent, així com la resta de la família. No podré agrair mai la extraordinària paciència i el suport de Caro durant tots aquests anys en que sempre ha estat al meu costat.

Finalment agrair l'ajut econòmic rebut per part del Departament d'Enginyeria Mecànica al concedir-me la beca URV per realitzar aquesta tesi doctoral, el finançament de la comunitat europea per fer l'estada al Edinburgh Parallel Computing Center així com el Projecte Europeu IMPULSE que ha finançat part d'aquest treball.

Només em queda agrair als membres del tribunal per acceptar judicar aquesta tesi doctoral i a totes aquelles persones que, directa o indirectament, han participat en la seua elaboració.

List of Figures

List of Tables

Chapter 1

Introduction

Turbulence is a phenomenon that occurs commonly in nature and its modeling is one of the key issues in Computational Fluid Dynamics (CFD). Compared with molecular diffusion, turbulence improves dramatically the transport of momentum, heat and species. A turbulent flow is generally three dimensional and time dependent and its complete description requires an enormous amount of information although in most practical situations only it is needed to know the mean flow properties.

Numerical simulations of turbulent flows may be accomplished using different levels of approximations yielding more or less detailed description of the state of the flow. One of the simplest methods is to use semi-empirical correlations. More sophisticated methods involve the numerical integration of the time averaged transport equations, the well-known Reynolds averaged Navier-Stokes equations (RANS) approach. The Reynolds stress terms, $\overline{u_i'u_j'}$, appear in the RANS equations as a consequence of the turbulent fluctuations. Theses terms need to be modeled to close the system of equations. The principal drawback of this approach is that the model represents the *mean* turbulence using averaged scales. While the small scales of the turbulent flows tend to be universal and flow-independent, the large scales are very strongly affected by the boundary conditions. Thus, there is no universal RANS model to solve accurately different turbulent flows.

The Direct numerical simulation (DNS) of turbulence is the most straightforward approach to the solution of turbulent flows. These simulations solve explicitly all the scales of the flow so numerical grids have to be fine enough to capture all the structures including the smallest where the energy taken from the mean flow is dissipated by the viscosity. Also, the time step for the time integration has to be small enough to resolve properly the minimum time scale of the flow. If the mesh is fine enough to resolve even the smallest scales of motion and the numerical scheme is designed to minimize the numerical dispersion and dissipative errors, then an accurate three-dimensional, time-dependent solution of the governing equations completely free of modeling assumptions can be obtained. DNS allows to compute any quantity of interest including those that are difficult or even impossible to measure in experiments. The main limitation for the DNS approach is that the number of grid points N required is proportional to $N \sim Re^{9/4}$ so the increase of the Reynolds number by a factor of two implies an increase of the computational effort by at least a factor of eight. An alternative to overcome this limitation is the Large-Eddy Simulation (LES) technique which can be considered to be between DNS and RANS. In a LES the contribution of the large energy-carrying structures to momentum and energy transfer is computed directly in the computational grid while the effect of the smallest scale of turbulence is modeled. This allows to use coarser grids reducing the computational requirements.

The code 3DINAMICS [1] has been used to solve numerically the transport equations for an incompressible fluid using the finite-volume approach over a staggered grid. All terms are discretized using second-order central differencing. The second-order Crank-Nicolson is used for time-discretization and a fractional step with multigrid as a Poisson solver is used for pressure calculation. For some of the simulations performed in this work it was necessary to develop accurate and robust discretization scheme to deal with the large gradient regions where non-physical results may be obtained due to the non-linearity of the advective terms.

Multigrid techniques have replaced the previous conjugate gradient methods for solving the pressure calculation. This step is the most costly in terms of CPU time. The multigrid approach has demonstrated to be faster in solving Poisson-like systems of equations compared with other methods. A parallel Full-Multigrid subroutine for different type of boundary conditions has been implemented in the 3DINAMICS code to speed-up this step and to improve the overall computational performance. The code is written in FORTRAN 90 with Message Passing Interface (MPI-CH) libraries. The cluster of the ECoMMFiT research group that consists in 24 bi-processor AMD Opteron nodes has been used to perform the simulations.

1.1 Background

Dispersion and mixing in turbulent flows is important to a variety of scientific and engineering phenomena including heat transport, chemical reaction and combustion, meteorology, oceanic sciences and environmental pollutant dispersion. A thorough understanding of scalar mixing in a turbulent flow is required. Reviews on the subject have been compiled by Sreenivasan [2], Shraiman and Siggia [3] and Warhaft [4].

The simulation of the dispersion from concentrated sources is an interesting topic because it may allow to predict, for example, the dispersion of a contaminant released from a smokestack in the atmospheric boundary layer.

The first works carried out by Taylor [5,6], Uberoi and Corrsin [7] and Townsend [8] dealt with scalar dispersion in turbulent homogeneous and isotropic turbulence. After that, the problem became more complex when non-isotropy was included. Scalar transport in a developed channel is an example of such type of flows. Difficulties are increased even more when flow inhomogeneities are taken into account.

The contaminant is released into a turbulent background at a scale usually much smaller than the integral scale of the velocity field. The released scalar is dispersed forming a plume that grows as it is convected downstream. The first studies on scalar dispersion in homogeneous and isotropic turbulence carried out by Taylor [5, 6], Uberoi and Corrsin [7] and Townsend [8] showed that the time-averaged temperature profiles were Gaussian and that the development of the plume can be divided into three stages: the molecular diffusive range, the turbulent convective range and the turbulent diffusive range. Although the mean temperature profiles are Gaussian, the r.m.s. profiles of the temperature turbulent fluctuation are not as it was demonstrated by Wrahaft [9] and Stapountzis et al. [10].

Sawford and Hunt [11] developed a Lagrangian stochastic model and their results were compared with the experimental data of Stapountzis [10] demonstrating that molecular diffusion and viscosity affect the development of the thermal plume (particularly the intensity of the temperature fluctuations) in all stages. This flow was also studied numerically by Anand and Pope [12] using Probability Density Functions (PDF) methods and Livescu et al. [13] used DNS to study the dispersion from line sources in homogeneous isotropic turbulence.

The analysis of the dispersion of a line source placed in an homogeneous turbulent shear flow would help to study the effect of this anisotropy on the scalar dispersion. Experimental works were carried out by Stapountzis and Britter [14], Karnik and Tavoularis [15] and Chunk and Kyong [16] providing mean and r.m.s. results and detailed information about the velocity-temperature correlations, the temperature PDFs and the joint velocity-temperature PDFs. Numerical results for similar experiments were carried out by Wilson et al. [17] and Cho and Chung [18].

Dispersion form line sources in boundary layers has been considered by Shlien and Corrsin [19]. These authors found that normalized mean temperature profile downstream the source approached an asymptotic form when normalized adequately. Paranthoën [20] deduced a rescaling scheme based on the temporal Lagrangian scale of the vertical velocity fluctuations collapsing the mean temperature profiles in a simple curve although temperature fluctuations did not scale well. Fackrell and Robins [21] measured variance, intermittency, peak concentration values, PDF and spectra of scalar concentration for ground and elevated locations in a turbulent boundary layers studying also the balance of terms in the variance and turbulent flux transport equations. Additional experimental work in dispersion in turbulent boundary layers were undertaken by Legg et al. [22] Veeravalli and Warhaft [23], Bara et al. [24], Tong and Warhaft [25] and Vincont et al. [26]. Scalar transport in low-Reynolds-number channel was simulated by Lyons and Hanratty [27], Papavassiliou and Hanratty [28] and Na and Hanratty [29]. Kontomaris and Hanratty [30] studied the effects of molecular diffusivity on a point source located at the centerline of a turbulent channel flow. Direct numerical simulations of dispersion from point sources in fully developed pipe have been performed by Brethouwer et al. [31]. Single and double line sources in fully developed flow were studied by Vrieling and Nieuwstadt [32]. Flows at higher Reynolds numbers and high aspect-ratio channels were studied experimentally by Lavertu and Mydlarski [33]. In other works, the passive scalar was released and absorbed at walls [34] or the scalar fluxes were imposed at the walls [27] providing additional information about the turbulence statistics of temperature. DNS in combination with Lagrangian methods has been used to study heat transport from sources at walls [35], [36]. Experiments of dispersion from line sources for conserved and reactive scalars have been carried out in homogeneous turbulence [37], [9], [10]. Other authors performed numerical simulations for released non-conserved passive scalars through line sources obtaining information about the influence of the mixing process on the chemical reaction rates [32], [38].

Other inhomogeneous turbulent flows have been studied by Bernard and Rovelstad [39], Wang and Komori [40] and Iliopoulos and Hanratty [41].

1.2 Objectives

The main objective in this work is to study the heat turbulent transport in a channel flow. The basic channel flow configuration consists in a flow driven by a mean pressure gradient between two parallel, smooth and infinite walls. Far from any entrance region, the flow becomes fully developed. Under such condition the streamwise and spanwise directions can be considered as homogeneous so periodic boundary conditions can be implemented in both directions.

The fully developed channel flow results obtained with the CFD code 3DINAMICS including mean and r.m.s. profiles and mean momentum equation balance have been validated by comparison with data available in literature and it constitutes the basic configuration for the different cases where turbulent heat transfer have been studied.

The first case studied involving turbulent heat transport corresponds to the transport of an scalar released from a source line located in the center of the channel forming a plume. Advection and diffusion are the only phenomena responsible for the dispersion from the concentrated source. In the near region, where inhomogeneities derived from the wall effect are not important, the mean profiles of temperature in the wall-normal direction are Gaussian-shaped. Once the plume approaches walls the Gaussian shape is lost. The larger the Reynolds number is the smaller plume width is obtained. Results are compared with avaliable data in literature of experimental and computational works.

The buoyancy forces appear when there are temperature differences within the fluid producing density variations. The buoyancy term is included in the momentum transport equation so velocity and temperature become coupled. Mixed convection in vertical channel simulations were performed to study the effect of buoyancy forces acting along the streamwise direction imposed by a mean pressure gradient. The goal of this simulation is to validate the code for the cases where forced convection induced by the mean pressure gradient acts simultaneously with buoyancy. The comparison of results obtained with the centered and the QUICK schemes for the discretization of the advective terms shows the effect of the numerical diffusion on the flow introduced by the upstream approach.

If the source line releases *hot* fluid within a *cold* background in a horizontal channel, the buoyancy forces drift the plume towards the top wall of the channel. The effect of the buoyancy on the heat transport is studied comparing the results obtained for the buoyant plume with those for the scalar (or neutrally buoyant) case. Symmetry obtained in the neutrally buoyant flow for mean quantities with respect to the channel midplane is lost when buoyancy aligned with the wall-normal direction is included.

The comparison in terms of computational efficiency between different solvers for Poisson equations is also another objective in this work. Such type of equations appear in the pressure calculation and usually represent one the most time consuming steps in the algorithm. Reducing this step by using a parallel multigrid solver allows to reduce significantly the total CPU time costs. Multigrid and two versions of the conjugate gradient methods are used to solve two synthetic cases with analytical solution and the coupling between pressure and velocity for a fully developed channel. The results in terms of CPU time and scalability are shown for different type of discretization grids and different boundary conditions.

Finally, some simulations are performed for a turbulent reactive flow where a reactant is released through the line source within a background containing another diluted reactant. The product is formed when these two species react following a second order chemical reaction. The Damkhöler number has been set to 1 and the reaction takes place under isothermal conditions.

1.3 Transport equations

The equations governing the conservation of mass, momentum, energy and species concentration in a Newtonian fluid flow can be written as [1] :

$$\frac{\partial \rho}{\partial t} + \frac{\partial}{\partial x_i}(\rho u_i) = 0 \tag{1.1}$$

$$\frac{\partial}{\partial t}(\rho u_i) + \frac{\partial}{\partial x_j}(\rho u_i u_j) = -\frac{\partial p}{\partial x_i} + \frac{\partial}{\partial x_j}\left[\mu\left(2S_{ij} - \frac{2}{3}\delta_{ij}S_{kk}\right)\right] + S_M \tag{1.2}$$

---

[1] All equations are written in Cartesian tensor notation

$$\frac{\partial(\rho h)}{\partial t}+\frac{\partial}{\partial x_j}\left(\rho u_j h\right)=\frac{\partial}{\partial x_j}\left[\kappa\left(\frac{\partial T}{\partial x_j}\right)\right]+\xi+\frac{\partial\left(u_j p\right)}{\partial x_j}+S_H \tag{1.3}$$

$$\frac{\partial(\rho Y_\alpha)}{\partial t}+\frac{\partial}{\partial x_j}\left(\rho Y_\alpha u_j\right)=-\frac{\partial}{\partial x_j}J_{\alpha j}+S_\alpha \tag{1.4}$$

where x_i are the space coordinates, u_i is the vector velocity, p is the pressure, T is the temperature, h is the enthalpy, ρ is the density, ν is the kinematic viscosity, μ is the dynamic viscosity and κ is the thermal conductivity.

The term S_{ij} in the momentum transport equation is defined as:

$$S_{ij}=\frac{1}{2}\left(\frac{\partial u_i}{\partial x_j}+\frac{\partial u_j}{\partial x_i}\right) \tag{1.5}$$

S_M represents a source term in the momentum transport equations and can include effects like gravity, Coriolis forces or buoyancy. In an analogous way, S_H is the source term for the energy transport equation and may take into account the heat released or absorbed during a chemical reaction. Finally, chemical reactions can be taken into account through the term S_α which can be interpreted as a source term in the mass transport equations.

The Kronecker delta δ_{ij} is defined as equal to 1 if $i=j$ and 0 otherwise. ξ is the dissipation function defined as $\tau_{ij}\partial u_i/\partial x_j$ which is usually omitted. For perfect gases the enthalpy can be expressed as $h=C_pT$ where C_p is the heat capacity.

The mass fraction of species α is defined as the ratio between the density of that species and the density of the mixture (constant for incompressible fluids) $Y_\alpha=\rho_\alpha/\rho$, S_α is the rate of creation of species α and $J_{\alpha j}$ is the molecular flux of species α in x_j-direction. In many applications one can assume that reactive species are dissolved in an inert carrier fluid. Furthermore, it is assumed that the mass fractions of the reactive species are small, i.e. dilute mixture is considered. In that case the mass molecular flux may be modeled with Fick's law which reads:

$$J_{\alpha j}=-\rho\mathcal{D}_\alpha\frac{\partial Y_\alpha}{\partial x_j} \tag{1.6}$$

where $\mathcal{D}_\alpha$ is the binary diffusion coefficient between species α and the carrier fluid. These parameters have been assumed constant for all the chemical compounds. Component density ρ_α can be replaced by C_α to denote the concentration of species α. The concentration C_α can either be regarded as an amount of mass per unit volume amount of fluid. i.e. $\sim \rho_\alpha$ or one can divide by the molar mass to obtain a concentration in terms of moles per unit volume amount of fluid. In this case, units of $\mathcal{D}_\alpha$ and S_α change accordingly.

Finally the transport equations assuming that all the physical properties are constant can be rewritten as:

$$\frac{\partial u_i}{\partial x_i} = 0 \tag{1.7}$$

$$\frac{\partial u_i}{\partial t} + \frac{\partial}{\partial x_j}\left(u_i u_j\right) = -\frac{1}{\rho}\frac{\partial p}{\partial x_i} + \nu \frac{\partial^2 u_i}{\partial x_j \partial x_j} + S_M \tag{1.8}$$

$$\frac{\partial T}{\partial t} + \frac{\partial\left(u_j T\right)}{\partial x_j} = \alpha_T \frac{\partial^2 T}{\partial x_j \partial x_j} + S_H \tag{1.9}$$

$$\frac{\partial C_\alpha}{\partial t} + \frac{\partial\left(C_\alpha u_j\right)}{\partial x_j} = \mathcal{D}_\alpha \frac{\partial^2 C_\alpha}{\partial x_j \partial x_j} + r_\alpha \tag{1.10}$$

where the term $\frac{\partial}{\partial x_j}\left(2S_{ij}\right)$ in equation 1.2, using continuity, $\frac{\partial}{\partial x_j}\left(\frac{\partial u_j}{\partial x_i}\right) = 0$, has been simplified as:

$$\frac{\partial}{\partial x_j}\left(\frac{\partial u_i}{\partial x_j} + \frac{\partial u_j}{\partial x_i}\right) = \frac{\partial^2 u_i}{\partial x_j \partial x_j} \tag{1.11}$$

and α_T represents the thermal diffusivity defined as $\alpha_T = \kappa/\rho C_p$.

In absence of chemical reactions between species, the reaction term is equal to zero so $r_\alpha = 0$. If density only depends on temperature, for an isothermal situation and in the absence of any other external force, no source term exists, so $S_M = 0$. On the other hand, temperature differences may induce density differences and this gives rise to buoyancy. This effect is taken into account through the source term using the Boussinesq [42] approximation [2] for its modellization:

$$S_M = -g_i \beta \left(T - T_{ref}\right) \tag{1.12}$$

where β is the thermal expansion coefficient defined as:

---

[2] g_i is the gravity vector

$$\beta = \frac{-1}{\rho}\left(\frac{\partial \rho}{\partial T}\right)_P \tag{1.13}$$

For ideal gases, $P = \rho R T$, and the equation 1.13 can be simplified as follows:

$$\beta = \frac{1}{T} \tag{1.14}$$

where T is expressed as an absolute temperature. Finally, T_{ref} is a reference temperature. If $T = T_{ref}$ no buoyancy effects are present.

By choosing an adequate set of characteristic scales, a set of non-dimensional variables can be obtained:

$$x_i^* = \frac{x_i}{\delta} \qquad u_i^* = \frac{u_i}{u_\tau} \tag{1.15}$$

$$p^* = \frac{p}{\rho\, u_\tau^2} \qquad t^* = \frac{t\, u_\tau}{\delta} \tag{1.16}$$

$$T^* = \frac{T - T_c}{\Delta T} \qquad C_\alpha^* = \frac{C_\alpha}{C_0} \tag{1.17}$$

where C_0 is the injection concentration for the reference reactive, δ is the channel half-width, $\Delta T = T_H - T_C$ is the difference between hot and cold wall temperature, T_H and T_C respectively, and u_τ is the friction velocity defined as $u_\tau = \sqrt{\tau_w/\rho}$ where τ_w is the shear stress at the wall defined as $\tau_w = \mu \left(\partial \langle u \rangle / \partial n\right)|_{wall}$. The brackets $<>$ are used to denote *ensemble averaged* quantities. The averaging procedure is used to obtain the time averaged transport equation that are explained in detail in section 3.3.

Including the source terms for buoyancy, for a second order chemical reaction and for the heat of reaction, equations 1.7, 1.8, 1.9 and 1.10 can be rewritten as (from now on $*$ notation have been omitted for sake of simplicity):

$$\frac{\partial u_i}{\partial x_i} = 0 \tag{1.18}$$

$$\frac{\partial u_i}{\partial t} + u_j \frac{\partial u_i}{\partial x_j} = -\frac{\partial p}{\partial x_i} + \frac{1}{Re_\tau}\frac{\partial^2 u_i}{\partial x_j \partial x_j} + \frac{Gr}{8Re_\tau^2}\left(T - T_{ref}\right) \tag{1.19}$$

$$\frac{\partial T}{\partial t}+u_j\frac{\partial T}{\partial x_j}=\frac{1}{PrRe_\tau}\frac{\partial^2 T}{\partial x_j \partial x_j}+Da\Upsilon C_A C_B \tag{1.20}$$

$$\frac{\partial C_\alpha}{\partial t}+u_j\frac{\partial C_\alpha}{\partial x_j}=\frac{1}{ScRe_\tau}\frac{\partial^2 C_\alpha}{\partial x_j \partial x_j}\pm DaC_A C_B \tag{1.21}$$

where the new dimensionless parameters appearing in equations 1.18, 1.19, 1.20 and 1.21 are defined in table 1.1.

Table 1.1: Dimensionless parameters

Reynolds number	$Re_\tau = \frac{u_\tau \delta}{\nu}$
Grashof number	$Gr = \frac{\Delta T(2\delta)^3}{\nu^2} g\beta$
Prandtl number	$Pr = \frac{\nu}{\alpha_T}$
Schmidt number	$Sc = \frac{\nu}{\mathcal{D}_{AB}}$
Damkhöler number	$Da = \frac{k\delta C_0}{u_\tau}$

The definition of the Damkhöler number and the units of the reaction rate, k, depend on the order of reaction:

$$[k]=\left[\frac{1}{s}\left(\frac{m^3}{mol}\right)^{n-1}\right] \tag{1.22}$$

$$Da=\frac{k\,\delta\,C_0^{n-1}}{u_\tau} \tag{1.23}$$

where n is the order of reaction. For $n=2$ the Damkhöler number is presented in table 1.1. The chemical reaction can be expressed as $A+B\longrightarrow P$. The ± sign in the source term of the mass transport equation is used to indicate that this term will be negative for reactants and positive for products provided that reaction rates are expressed as:

$$r_A = -Da\,C_A C_B \tag{1.24}$$

$$r_B = -Da\,C_A C_B \tag{1.25}$$

$$r_R = Da\,C_A C_B \tag{1.26}$$

Finally Υ is a dimensional quantity that relates the heat released or consumed in the chemical reaction with the sensible heat of the fluid. It is defined as:

$$\Upsilon = \frac{\Delta \hat{H}_r^0 \, C_0}{\rho \, Cp \Delta T} \tag{1.27}$$

This nondimensional quantity is similar to the Jakob number used to relate the sensible to the latent heats in a boiling fluid.

Chapter 2

Physical model

The main objective of this work is to analyze the turbulent heat transport in a channel flow where a hot fluid is released in the channel through a line source. If the line source and the background carrying fluid have different temperatures, the formed plume can be affected by buoyancy forces. The flow configurations considered are based on the fully developed pressure driven channel flow between two parallel, infinite and smooth walls placed a distance 2δ apart. The streamwise, spanwise and wall-normal directions are denoted as x, y and z respectively. A sketch of the domain including the coordinate system origin (tagged O) is shown in figure 2.1.

The cases considered in this work are summarized in table 2.1 including the grid resolution, the Reynolds number based on the friction velocity and the half width of the channel, the Reynolds number based on the bulk velocity and the width of the channel and the Grashof number and the reference temperature for cases B and C where buoyancy forces are present.

The dimensions of the channel are $8\pi\delta \times 2\pi\delta \times 2\delta$. The two walls of the channel are located at $z = -\delta$ and $z = \delta$ and are considered adiabatic for cases A and C and at fixed temperatures for case B.

The validation of the code involved the simulation of two flow configurations

Table 2.1: Summary of flow configurations

Case	Description	Grid resolution	Re_τ	$Re_{2\delta}$	Gr	T_{ref}	Buoyancy
A	Passive plume	$258 \times 130 \times 130$	180	5452	–	–	None
B	Mixed convection	$131 \times 101 \times 101$	150	2725	$9.6 \cdot 10^5$	0.5	x
C	Buoyant plume	$258 \times 130 \times 130$	180	5472	10^7	0.0	z

Figure 2.1: Sketch of the channel configuration

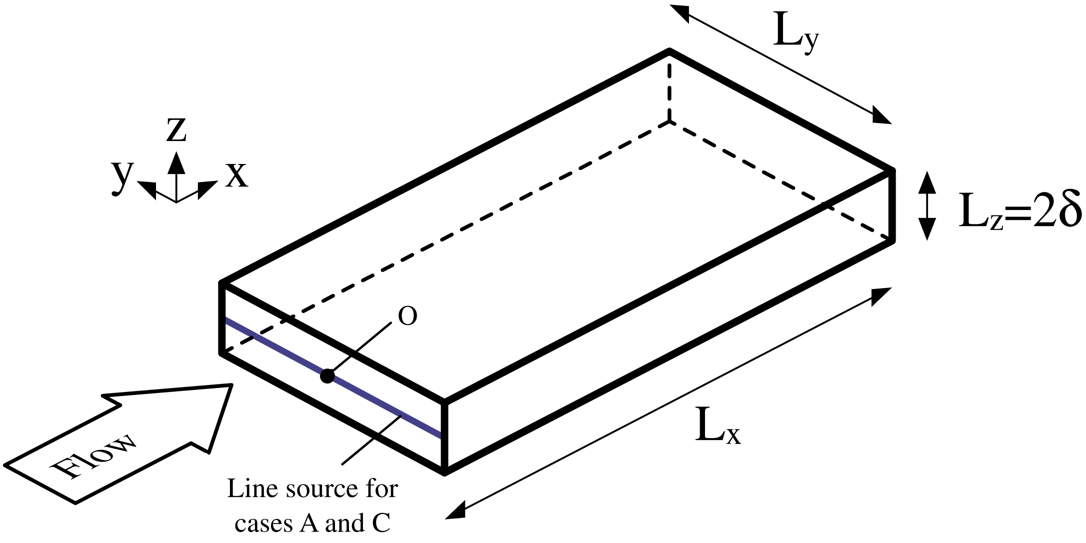

named case A and B for which there are results avaliable in the literature. The first one, case A, considers the dispersion of a passive scalar released in a channel flow through a line source centered in the vertical direction as indicated in figure 2.1. In this case the temperature can be considered as a passive scalar. The second one, case B, is a mixed convection configuration with the buoyancy force aligned with the streamwise direction. The buoyancy force is produced by a temperature difference imposed at the two walls of the channel. All the results obtained for cases A and B show good agreement with data avaliable in the literature as shown in section 6. The difference between cases A and C is that in case C the velocity and the temperature fields are coupled by the buoyancy forces acting in the wall-normal direction.

2.1 Case A: Temperature line source in a channel at $Re_\tau = 180$

The first flow configuration considers the heat transport in a fully developed channel flow where temperature is released from a line source. In this case, named A, there is no buoyancy and temperature acts as a passive scalar. The Reynolds number is $Re_\tau = 180$. The molecular Prandtl number is $Pr = 0.71$. The spanwise direction is considered homogeneous for all variables. In the streamwise direction homogeneity is considered for the hydrodynamic field but not for the temperature where non-reflecting boundary conditions are applied at the outlet. At the inlet the source line is implemented as a spanwise band centered in the middle of the channel ($z = 0$) with a size of $2H_S$ where $H_S = 0.054\delta$. Thus, the temperature distribution is $T(0,y,z,t) = T_0 = 1 \ \forall z \in [-H_S, H_S]$ and $T(0,y,z,t) = T_\infty = 0, \ \forall z \ni [-H_S, H_S]$.

2.2 Case B: Mixed convection at $Re_\tau = 150$ and $Gr = 9.6 \cdot 10^5$

The configuration for the case B corresponds to a mixed convection fully developed flow in a vertical channel with the gravity vector aligned with the streamwise direction where the momentum and heat transport are coupled by the buoyancy force. The molecular Prandtl number is 0.71, the Grashof number is $9.6 \cdot 10^5$ and the Reynolds number based on the friction velocity is $Re_\tau = 150$. The streamwise and spanwise directions are considered as homogeneous and periodic boundary conditions are applied for the velocity, pressure and temperature fields. Both walls have no-slip boundary conditions. The dimensionless temperatures on the top and bottom walls are prescribed to be $T(x,y,-\delta,t) = T_H = 1$ and $T(x,y,\delta,t) = T_C = 0$, respectively. The dimensionless reference temperature is $T_{ref} = (T_H + T_C)/2 = 0.5$.

The hydrodynamic variables have been initialized using instantaneous fields from previous fully developed channel flow results. The temperature has been initialized with a constant distribution at T_{ref} (no buoyancy). It was found that the simulations are very sensitive to the initial conditions for temperature. Difficulties in achieving steady statistics were experienced when temperature was initialized using a linear profile form the cold wall to the hot wall. It was found that for the mixed convection cases, a very large domain along the streamwise direction was needed. If a smaller box is used no quasi-steady conditions were obtained and the bulk velocity and temperature varied with a very low frequency [43].

2.3 Case C: Buoyant source line in a channel at $Re_\tau = 180$ and $Gr = 10^7$

Case C is similar to case A where a line source is vertically centered at the channel inlet but, as it happened in case B, momentum and heat are coupled through the buoyancy term. However, in this case, the gravity vector is aligned with the z direction (perpendicular to the walls of the channel). The plume formed by the source line is hotter than the background colder fluid and, due to the density differences, the buoyancy forces deflect the plume towards the top wall.

Streamwise direction for case C is not homogeneous due to the coupling between momentum and heat equations and periodic boundary conditions are no valid in this case. To solve this issue, a buffer region has been attached at the inlet of the channel section where the line source is considered. This buffer region allows to obtain the hydrodynamic fields at the inlet of the main domain. Non-reflecting boundary conditions are implemented at the outlet for hydrodynamic and temperature variables. A sketch of the computational domain including the buffer is shown in figure 2.2. The size of the computational domain and the mesh distribution of the buffer are the same as in the main domain. At each time step the flow in the buffer region is computed and the velocity and pressure distributions at the outlet of the buffer region are used as the boundary conditions for the computation of the flow in the main domain where the plume develops.

The coupling between the velocity and the temperature equations and the consequent non-homogeneity in the streamwise direction requires to implement convective boundary conditions for the hydrodynamic field at the outlet of the domain. These boundary conditions, called non-reflecting, were introduced by Jin and Braza [44] for two dimensional incompressible flows.

In this work, these non-reflecting boundary conditions results have been extended to a three-dimensional case using an analogous procedure.

Considering the characteristics of the present viscous elliptic flow, an anisotropic propagation wave equation on the outlet boundary for any transported quantity Θ (velocity component, temperature, concentration...) can be written as:

$$\frac{\partial^2\Theta}{\partial t^2} - c_x\frac{\partial^2\Theta}{\partial x^2} - c_y\frac{\partial^2\Theta}{\partial y^2} - c_z\frac{\partial^2\Theta}{\partial z^2} = 0 \tag{2.1}$$

where c_x, c_y and c_z are the characteristic velocities of the wave propagation in the

Figure 2.2: Buffer domain

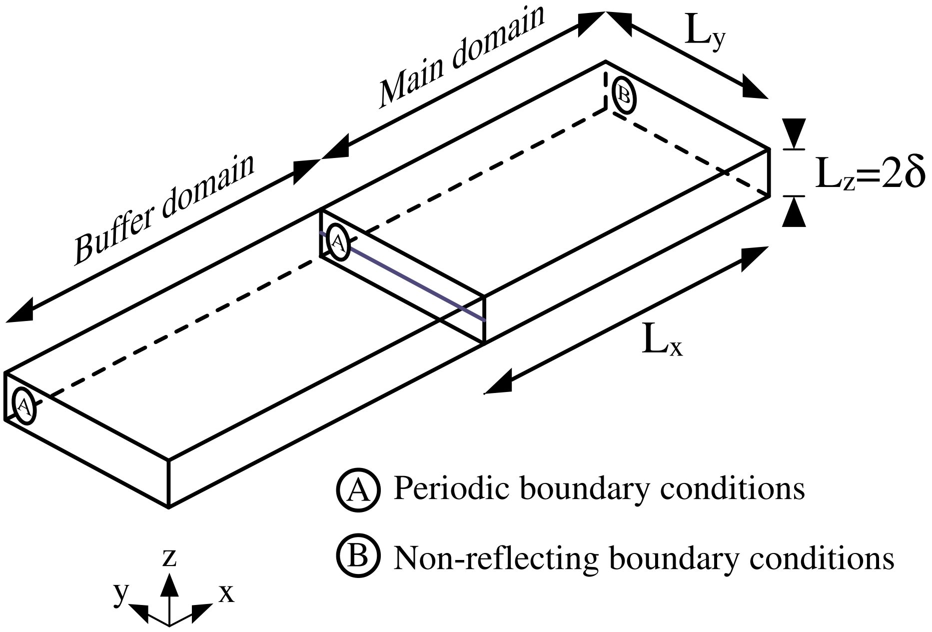

x, y and z directions respectively. The pseudo-differential operators are introduced:

$$L\Theta \equiv c_x^2 D_x^2 \Theta + c_y^2 D_y^2 \Theta + c_z^2 D_z^2 \Theta - D_t^2 \Theta = 0 \tag{2.2}$$

where D_x, D_y, D_z designate the partial derivatives with respect to x, y and z, respectively and D_t to denote partial derivative with respect to time. Factorization of the wave operator, L, gives:

$$L\Theta = L^+ L^- \Theta = 0 \tag{2.3}$$

where

$$L^+ \equiv c_x D_x + D_t \sqrt{1 - a^2 - b^2} \tag{2.4}$$

and

$$L^- \equiv c_x D_x - D_t \sqrt{1 - a^2 - b^2} \tag{2.5}$$

where

$$a = \frac{c_y D_y}{D_t} \tag{2.6}$$

$$b = \frac{c_z D_z}{D_t} \tag{2.7}$$

The relation:

$$L^+ \Theta = 0 \tag{2.8}$$

applied to the outlet boundary condition is a total absorption (non-reflecting) condition [45]. As the pseudo-differential operator is nonlocal in both time and space variables, the following Padé approximation of the square root $\sqrt{1-a^2-b^2}$ is used:

$$\sqrt{1-a^2-b^2} \approx 1 - \frac{1}{2}\left(a^2+b^2\right) \tag{2.9}$$

and then equation 2.8 can be approximated as:

$$\left(c_x D_x + D_t - \frac{c_y^2}{2D_t} D_y^2 - \frac{c_z^2}{2D_t} D_z^2\right)\Theta = 0 \tag{2.10}$$

The coefficients c_y and c_z appear because of the anisotropic character of the present analysis.

Comparison of equation 2.10 with the Navier-Stokes equations 1.19, shows that the diffusion term in equation 2.10 is reasonably set as $(1/Re_\tau)\left(\partial^2\Theta/\partial y^2 + \partial^2\Theta/\partial z^2\right)$ and the propagation velocity c_x is made equal to the u component in order to match this equation to the Navier-Stokes equations. In a similar way, if Θ represents the temperature or the concentration of a species C_α, the coefficient multiplying the diffusive term is $(1/Re_\tau Pr)$ or $(1/Re_\tau Sc)$ respectively.

Finally the equations for the outlet boundary can be written as:

$$\frac{\partial u_i}{\partial t} + u\frac{\partial u_i}{\partial x} - \frac{1}{Re_\tau}\left(\frac{\partial^2 u_i}{\partial y^2} + \frac{\partial^2 u_i}{\partial z^2}\right) = 0 \tag{2.11}$$

$$\frac{\partial T}{\partial t} + u\frac{\partial T}{\partial x} - \frac{1}{Re_\tau Pr}\left(\frac{\partial^2 T}{\partial y^2} + \frac{\partial^2 T}{\partial z^2}\right) = 0 \tag{2.12}$$

$$\frac{\partial C_\alpha}{\partial t} + u\frac{\partial C_\alpha}{\partial x} - \frac{1}{Re_\tau Sc}\left(\frac{\partial^2 C_\alpha}{\partial y^2} + \frac{\partial^2 C_\alpha}{\partial z^2}\right) = 0 \tag{2.13}$$

These equations keep a convective/advective term for the main component of velocity (the streamwise component u for the channel).

The pressure correction Φ has Neumann boundary conditions for all boundaries (inlet, walls and homogeneous y direction) except for the outlet where no correction is applied to obtain convergence in the iterative procedure to solve the coupling between the velocity and the pressure fields. This non-consistent boundary condition would introduce anomalous values for the velocity at the outlet. To correct this and ensure continuity, the convective velocity at the outlet is recalculated after the pressure correction step.

Chapter 3

Mathematical analysis

3.1 The finite volume method

Transport equations are discretized on a staggered grid with the pressure, temperature and concentrations (scalars) calculated in the center of a cell and the velocity components defined at the cell faces.

To introduce the discretization of the transport equations using the finite-volume approach, the conservation law for the transport of a scalar quantity ϕ in a unsteady flow in its general form is used:

$$\frac{\partial}{\partial t}(\rho\phi) + div(\rho\vec{u}\phi) = div(\Gamma\, grad\,\phi) + S_\phi \tag{3.1}$$

By using Gauss' divergence theorem:

$$\int_{CV} div\,\vec{a}\,dV = \int_A \vec{n}\cdot\vec{a}\,dA \tag{3.2}$$

where $\vec{n}$ is the vector normal to surface element dA.

By changing the order of integration in the time derivate term, the integration of equation (3.1) over a control volume (CV) and a time step Δt, gives:

$$\int_{CV}\left[\int_t^{t+\Delta t}\frac{\partial}{\partial t}(\rho\phi)\,dt\right]dV + \int_t^{t+\Delta t}\left[\int_A \vec{n}\cdot(\rho\vec{u}\phi)\,dA\right]dt = \int_t^{t+\Delta t}\left[\int_A \vec{n}\cdot(\Gamma\, grad\,\phi)\,dA\right]dt + \int_t^{t+\Delta t}\left[\int_{CV} S_\phi dV\right]dt \tag{3.3}$$

where Γ is a diffusion coefficient.

To demonstrate the integration, the following one-dimensional equation can be used.

$$\int_w^e \left[\int_t^{t+\Delta t} \frac{\partial}{\partial t}(\rho\phi)\,dt\right] dV + \int_t^{t+\Delta t} \left[(\rho u A\phi)_e - (\rho u A\phi)_w\right] dt = \int_t^{t+\Delta t} \left[\left(\Gamma A\frac{\partial\phi}{\partial x}\right)_e - \left(\Gamma A\frac{\partial\phi}{\partial x}\right)_w\right] dt + \int_t^{t+\Delta t} \bar{S}\Delta V\,dt \tag{3.4}$$

The diffusive flux term is evaluated as:

$$\begin{aligned}\left(\Gamma A\frac{d\phi}{dx}\right)_e &= \Gamma_e A_e\left(\frac{\phi_E - \phi_P}{\delta x_{PE}}\right)\\ \left(\Gamma A\frac{d\phi}{dx}\right)_w &= \Gamma_w A_w\left(\frac{\phi_P - \phi_W}{\delta x_{WP}}\right)\end{aligned} \tag{3.5}$$

Here the upper-case letters ($N \rightarrow$ *north*, $E \rightarrow$ *east*, etc) subindices refer to the node point and the lower case letters indicate the face points. The Navier-Stokes equation 1.19 can now be integrated over a time step Δt and a control volume (CV). Figure 3.1 shows a staggered grid arrangement for a two-dimensional domain indicating the scalar, the u-component and the v-component control volumes (dotted lines, red pattern and blue pattern respectively). The use of staggered grids, introduced by Harlow and Welch [46], prevents unrealistic pressure fields [47].

3.2 Temporal integration

3.2.1 Momentum transport equations

The numerical integration of the Navier-Stokes equations demands special attention due to the fact that it is needed to solve the coupling between pressure and velocity. There are different methods described in literature to solve this coupling. Some popular solutions are MAC [46], SIMPLE [48] and PISO [49]. In this work, a multistep procedure has been used [50–53]. In the first step, the transport equation is solved using velocities and pressure from the current time step. The velocity field obtained, u_i^*, may not satisfy the continuity equation. In the second correction step,

Figure 3.1: Staggered grid for the finite volume approach

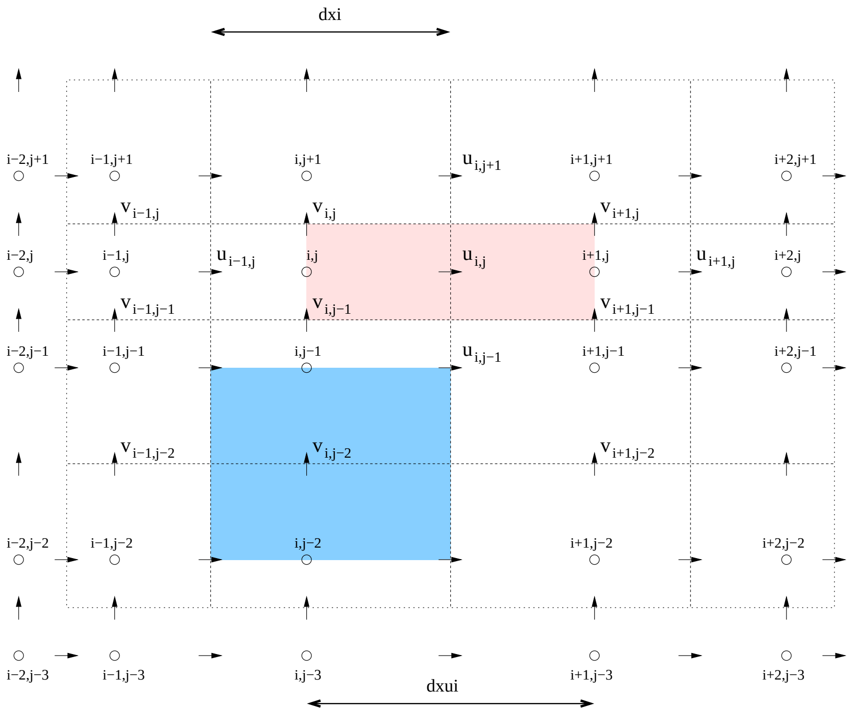

continuity is forced and new pressure and velocity fields are obtained after solving a Poisson equation involving the pressure correction Φ and the divergence of the intermediate velocity field u_i^*.

The Navier-stokes equations without buoyancy are used to illustrate this step:

$$\int_{CV}\left(\int_t^{t+\Delta t}\frac{\partial u_i}{\partial t}dt\right)dV+\int_t^{t+\Delta t}\left(\int_{CV}\frac{\partial}{\partial x_j}\left(u_iu_j\right)dt\right)dV=$$
$$-\int_t^{t+\Delta t}\left(\int_{CV}\frac{1}{\rho}\frac{\partial p}{\partial x_i}dt\right)dV+\int_t^{t+\Delta t}\left(\int_{CV}\nu\frac{\partial^2 u_i}{\partial x_j\partial x_j}dt\right)dV \tag{3.6}$$

Integration of each term Ψ_P with respect to time can be written as:

$$I_T=\int_t^{t+\Delta t}\Psi_P dt=\left[\alpha\Psi_P^{n+1}+(1-\alpha)\Psi_P^n\right]\Delta t \tag{3.7}$$

where Ψ_P^n refers to the value at time t, and Ψ_P^{n+1} at time $t+\Delta t$ and where the weighting parameter α is $\frac{1}{2}$ for Crank-Nicholson, which is the time integration scheme that has been used in this work for the momentum transport equations. The explicit time integration scheme is given by $\alpha = 0$ and the fully implicit integration is obtained with $\alpha = 1$.

Finally equation (3.6) can be discretized as:

$$\frac{u_i^{n+1} - u_i^n}{\Delta t} = \alpha \left[-\frac{\partial}{\partial x_j} \left(u_i^{n+1} u_j^{n+1} \right) + \nu \frac{\partial^2 u_i^{n+1}}{\partial x_j \partial x_j} \right] - \frac{1}{\rho} \frac{\partial p^{n+1}}{\partial x_i} + (1 - \alpha) \left[-\frac{\partial}{\partial x_j} \left(u_i^n u_j^n \right) + \nu \frac{\partial^2 u_i^n}{\partial x_j \partial x_j} \right] \tag{3.8}$$

Using an intermediate velocity u_i^* one can write similarly:

$$\frac{u_i^* - u_i^n}{\Delta t} = \alpha \left[-\frac{\partial}{\partial x_j} \left(u_i^* u_j^* \right) + \nu \frac{\partial^2 u_i^*}{\partial x_j \partial x_j} \right] - \frac{1}{\rho} \frac{\partial p^n}{\partial x_i} + (1 - \alpha) \left[-\frac{\partial}{\partial x_j} \left(u_i^n u_j^n \right) + \nu \frac{\partial^2 u_i^n}{\partial x_j \partial x_j} \right] \tag{3.9}$$

Equation (3.9) is solved iteratively for u_i^*. This velocity field does not ought to satisfy the continuity equation.

By subtracting (3.9) from (3.8):

$$\frac{u_i^{n+1} - u_i^*}{\Delta t} = \alpha \left[-\frac{\partial}{\partial x_j} \left(u_i^{n+1} u_j^{n+1} \right) + \nu \frac{\partial^2 u_i^{n+1}}{\partial x_j \partial x_j} \right] - \frac{1}{\rho} \frac{\partial p^{n+1}}{\partial x_i} - \alpha \left[-\frac{\partial}{\partial x_j} \left(u_i^* u_j^* \right) + \nu \frac{\partial^2 u_i^*}{\partial x_j \partial x_j} \right] + \frac{1}{\rho} \frac{\partial p^n}{\partial x_i} \tag{3.10}$$

By rearranging the previous equations using $H(u_i)$ for the convective and diffusive terms as:

$$H(u_i) = \left[-\frac{\partial}{\partial x_j}\left(u_i u_j\right) + \nu \frac{\partial^2 u_i}{\partial x_j \partial x_j} \right] \tag{3.11}$$

the error of replacing $H(u_i^*)$ by $H(u_i^{n+1})$ is of second order in time [54] and thus consistent with others errors. Equation (3.10) can be written as:

$$\rho \frac{\left(u_i^{n+1} - u_i^*\right)}{\Delta t} = -\frac{\partial p^{n+1}}{\partial x_i} + \frac{\partial p^n}{\partial x_i} \tag{3.12}$$

By applying the divergence operator to equation (3.12) with $\frac{\partial u_i^{n+1}}{\partial x_i} = 0$ one obtains:

$$-\frac{\rho}{\Delta t}\frac{\partial u_i^*}{\partial x_i} = -\frac{\partial^2 p^{n+1}}{\partial x_i^2} + \frac{\partial^2 p^n}{\partial x_i^2} \tag{3.13}$$

The pressure correction Φ is defined as

$$\Phi = p^{n+1} - p^n \tag{3.14}$$

so equation (3.13) can be rewritten as:

$$\frac{\rho}{\Delta t}\frac{\partial u_i^*}{\partial x_i} = \frac{\partial^2 \Phi}{\partial x_i^2} \tag{3.15}$$

This Poisson equation is solved using the multigrid procedure. Once Φ is obtained, one can calculate the new pressure p^{n+1} using the relation (3.14) and go back to equation (3.12) to find the new velocities u_i^{n+1}.

3.2.2 Heat and mass transport equations

The numerical integration of the transport equations has to guarantee the conservation of heat and mass. The non-linearity of the convective terms can lead to spurious oscillations of the temperature or concentration fields in regions of the computational domain with sharp gradients. Such oscillations may produce values out of the range prescribed by the inherent limits imposed by the boundary conditions. In this work, these large values of the scalar gradients are expected to appear due to the implementation of a discrete line source at the inflow boundary for cases A and C.

For reacting flows, the reaction rates, appearing in the conservation equations for the different chemical species involved, are expressed as a product of concentrations and the sign of this term indicates if the species is a reactant that is being consumed (negative) or a product that is being generated (positive). In this scenario, non-physical oscillations are specially important since the out of range values lower than zero may invert the reaction rate sign.

Some authors overcome this problem related with the large values of the gradients, at least partially, by setting a smooth concentration distribution at the source [32].

It has been observed that the temporal integration of the scalar transport equations using the Crank-Nicholson scheme produces such oscillations for cases A and C. The direct cutting off of these values leads to the non-conservation of the quantities. To overcome this drawback for these two cases, the fully explicit and second-order in time Adams-Bashforth scheme was tested:

$$I_T = \int_t^{t+\Delta t} \Psi_P dt = \left[\frac{3}{2}\Psi_P^n - \frac{1}{2}\Psi_P^{n-1}\right]\Delta t \tag{3.16}$$

The explicit Adams-Bashforth temporal integration, used in combination with a robust advection term discretization scheme, avoids these oscillations. In this work two discretization methods for the convective term have been tested: the QUICKEST scheme with the ULTIMATE correction [55] and the Total Variation Diminishing with (TVD) $\kappa = \frac{1}{3}$ [56].

The use of the QUICKEST discretization scheme produces some scalar values out of range (< 0.001 %) which are removed by simply filtering their values to the adequate limit value. Some multidimensional approaches have been developed following the ULTIMATE correction [57]. These techniques improve the flow-to-grid angle dependence and the anisotropic distortion, but require additional CPU and communication resources. Even though, this procedure requires larger computational effort compared with the Total Variation Diminishing and problems with the symmetry of the time averaged temperature profiles were experienced.

The Total Variation Diminishing approach guarantees accuracy and monotonicity by an adequate limiter function in the upwind advection operator. In this work the $\kappa = \frac{1}{3}$ [56] is used where κ is the weighting parameter ranging form -1 for the second-order accurate fully one-sided upwind scheme to 1 for the second-order accurate central scheme. A value between these limits represents a blend between these two schemes. Monotonicity is guaranteed using a limiter function that is inside of Sweby's monotonicity domain. The argument for this function is the upwind ratio of consecutive gradients, r. As example, for the east face of a control volume, it can be written as:

$$r_E = \frac{\phi_{i+1} - \phi_i + \varepsilon}{\phi_i - \phi_{i-1} + \varepsilon} \tag{3.17}$$

where r_E is the upwind ratio of consecutive gradients at the east face of a control volume for a ϕ variable. The constant ε is set to a very small number ($1 \cdot 10^{-10}$) and it is introduced to avoid division by zero in uniform flow regions.

The limiter function $\Phi(r)$ reads:

$$\Phi(r) = max\left(0, min\left(2r, min\left(\frac{1}{3} + \frac{2}{3}r, 2\right)\right)\right) \tag{3.18}$$

3.3 Averaged transport equations

In time dependent flows the mean of a property at time t is taken to be the average of the instantaneous values of the property over a large number of repeated identical experiments: the so called *ensemble average*. Brackets are used to denote ensemble averaged quantities. For a instantaneous quantity ϕ, $<\phi>$ is its ensemble averaged value.

Flows with steady statistics are also called time-independent, i.e. mean values are not a function of time. It is obvious that in this case both averages (ensemble and time averages) should give the same results. The time averaged value of an instantaneous quantity ϕ is defined as:

$$\Phi = \frac{1}{\Delta t}\int_0^{\Delta t} \phi(t)dt \tag{3.19}$$

where Φ is the mean value and Δt is supposed to be much larger than the largest time scale of the flow (that corresponding to the largest flow scale). Thus, any quantity can be expressed as the sum of a mean and a fluctuating term as $\phi(\vec{x},t) = \Phi(\vec{x}) + \phi'(\vec{x},t)$ where ϕ' is the time-varying fluctuation. This fluctuation has, by definition, a mean value equal to zero:

$$\overline{\phi'} = \frac{1}{\Delta t}\int_0^{\Delta t} \phi'(t)dt = 0 \tag{3.20}$$

where an overbar $\overline{\phi'}$ have been used to denote time-averaging operation. Another important statistical parameter is the root-mean-square (r.m.s.) of the fluctuations defined as:

$$\phi_{rms} = \sqrt{\overline{(\phi')^2}} = \left[\frac{1}{\Delta t}\int_0^{\Delta t} (\phi')^2\, dt\right]^{1/2} \tag{3.21}$$

This statistic which gives indication of the intensity of the fluctuations is in practice evaluated as:

$$\phi_{rms} = \sqrt{\overline{\phi^2} - \overline{\phi}^2} \tag{3.22}$$

Following this approach for the pressure and the velocity components, they can be written as $p = P + p'$, $u = U + u'$, $v = V + v'$, $w = W + w'$, and the time averaged momentum equations (without source terms) leads to:

$$\frac{\partial U_i}{\partial t} + U_j \frac{\partial U_i}{\partial x_j} = -\frac{\partial P}{\partial x_i} + \frac{1}{Re_\tau}\frac{\partial^2 U_i}{\partial x_j \partial x_j} - \frac{\partial \overline{u_i' u_j'}}{\partial x_j} \tag{3.23}$$

The averaging of the momentum equations gives rise to new extra terms: six new additional stresses $\overline{u_i' u_j'}$. These terms are the *Reynolds stresses* and equations 3.23 are called the *Reynolds equations*.

The time averaged momentum equations governing the fully developed turbulent channel flow without buoyancy can be written as:

$$0 = \frac{\partial P}{\partial x} - \frac{\partial \overline{u'w'}}{\partial z} + \frac{1}{Re_\tau}\frac{\partial U^2}{\partial z^2} \tag{3.24}$$

$$0 = \frac{\partial P}{\partial z} - \frac{\partial \overline{w'^2}}{\partial z} \tag{3.25}$$

The integration of 3.25 yields:

$$P + \overline{w'^2} = P_0 \tag{3.26}$$

where P_0 is a function of x only. Because $\overline{w'^2}$ is independent of x (by the fully developed assumption), $\partial P/\partial x$ is equal to dP_0/dx. These two gradients have to be independent of x to avoid streamwise acceleration of the flow. Integrating equation 3.24 from $z = -\delta$, it yields:

$$0 = z + \delta + \frac{1}{Re_\tau}\frac{\partial U}{\partial z}\bigg|_z - \tau_w - \overline{u'w'}\Big|_z \tag{3.27}$$

where τ_w is the wall shear stress defined as $\tau_w = \rho {u_\tau}^2$.

The overall force balance for the mean flow shows that the mean pressure gradient is balanced by the mean shear stress on the walls (see figure 3.2). Taking a differential volume of fluid $\Delta V = \Delta x L_y 2\delta$ the force balance can be written as:

Figure 3.2: Global force balance in a channel

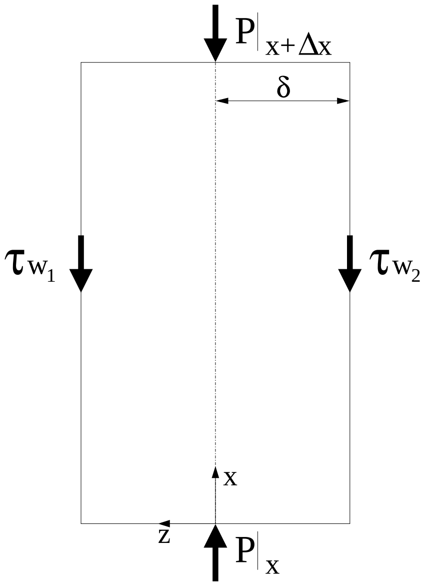

$$P|_x L_y 2\delta - P|_{x+\Delta x} L_y 2\delta = \tau_w \Delta x L_y \tag{3.28}$$

And dividing by ΔV and taking the limit one obtains:

$$\lim_{\Delta x \to 0} \frac{P|_x - P|_{x+\Delta x}}{\Delta x} = \frac{\tau_w}{2\delta} \tag{3.29}$$

Finally, taking into account that $\tau_w = \tau_{w_1} + \tau_{w_2} = 2\rho {u_\tau}^2$ and adimensionalizing, the resulting global balance, can be written as,

$$\frac{-\rho {u_\tau}^2}{\delta}\frac{dP^*}{dx^*} = \frac{\rho {u_\tau}^2}{\delta} \tag{3.30}$$

$$\frac{dP^*}{dx^*} = \frac{dP_0}{dx} = -1 \tag{3.31}$$

The non-dimensionalization of the transport equations with the bulk velocity U_b in the channel configuration would leave two dimensionless parameters: the Reynolds number, Re, and a mean pressure gradient $d\hat{p}/dx$ where $\hat{p}$ is the pressure adimensionalized with the bulk velocity. The use of the friction velocity u_τ as a velocity scale allows to reduce the number of parameters to one: Re_τ. In this case the mean pressure gradient dP^*/dx^* is equal to minus one.

The relation between the Reynolds number based on bulk velocity, Re, and Reynolds number based on friction velocity, Re_τ, is:

$$Re = \frac{U_b\,\delta}{\nu} \tag{3.32}$$

$$Re_\tau = \frac{u_\tau\,\delta}{\nu} \tag{3.33}$$

$$\frac{Re}{Re_\tau} = \frac{U_b}{u_\tau} = \frac{1}{A^*}\int_{A^*} U^* dA^* = \frac{1}{L_y L_z}\int_0^{L_y}\int_0^{L_z} U^* dz^* dy^* \tag{3.34}$$

The periodicity of the pressure field at the streamwise boundaries of the domain allows the decomposition of the pressure into a periodic contribution and a linearly varying term along the streamwise direction. The linearly varying term is the mean pressure gradient dP_0/dx and the periodic term includes only the fluctuation p'. Using this decomposition, the pressure is now expressed as:

$$p(\vec{x},t) = p'(\vec{x},t) + \frac{dP_0}{dx}x \tag{3.35}$$

where $\frac{dP_0}{dx} = -1$. The pressure term in the momentum equation 1.8 can be written as:

$$-\frac{\partial p}{\partial x} = -\frac{\partial p'}{\partial x} + \delta_{i1} \tag{3.36}$$

The mean shear stress over a wall can be calculated as:

$$\tau_w = \mu \left.\frac{\partial U}{\partial z}\right|_{wall} \tag{3.37}$$

The time-averaging procedure applied to the Navier-Stokes equations can also be applied to the other transport equations. To average the energy and the mass transport equations, 1.20 and 1.21 respectively, it is necessary to define the temperature and the concentration as the sum of a mean and a fluctuating term as it was done before, so $T = \overline{T} + T'$ and $C_\alpha = \overline{C_\alpha} + C'_\alpha$. The averaged energy transport equation follows:

$$\frac{\partial \overline{T}}{\partial t} + U_j \frac{\partial \overline{T}}{\partial x_j} = \frac{1}{Re_\tau Pr} \frac{\partial^2 \overline{T}}{\partial x_j \partial x_j} - \frac{\partial \overline{T' u'_j}}{\partial x_j} \tag{3.38}$$

In an analogous way, the averaged mass transport equation for the chemical specie α (without chemical reactions) follows:

$$\frac{\partial \overline{C_\alpha}}{\partial t} + U_j \frac{\partial \overline{C_\alpha}}{\partial x_j} = \frac{1}{Re_\tau Sc} \frac{\partial^2 \overline{C_\alpha}}{\partial x_j \partial x_j} - \frac{\partial \overline{C'_\alpha u'_j}}{\partial x_j} \tag{3.39}$$

Analogous to the *Reynolds stresses*, $\overline{T' u'_j}$ and $\overline{C'_\alpha u'_j}$ are the turbulent fluxes of heat and mass.

In what follows, the momentum and energy balances of the averaged momentum and heat transport equations for the cases stated in table 2.1 are presented.

3.3.1 Case A: Temperature line source in a channel at $Re_\tau = 180$

For case A (see figure 2.1), only the wall-normal direction is relevant for the mean flow, so the integration of the time averaged momentum equation can be expressed as:

$$0 = \underbrace{z+\delta}_{1} + \underbrace{\frac{1}{Re_\tau} \left.\frac{\partial U}{\partial z}\right|_z}_{2} - \underbrace{\tau_w}_{3} - \underbrace{\left.\overline{u'w'}\right|_z}_{4} \tag{3.40}$$

where τ_w is the shear stress on a wall of the channel and it can be written as (in nondimensional form):

$$\tau_w = \frac{1}{Re_\tau} \left. \frac{\partial U}{\partial z} \right|_{wall} \tag{3.41}$$

The numeration that appears at the bottom of the equation is used in the next chapters to identify the different terms of the balances.

Equation 3.40 indicates that locally the mean pressure gradient is balanced by the friction at the walls and by the Reynolds shear stress $\overline{u'w'}$.

For the heat transport equation, the streamwise direction is not homogeneous as shown in figure 2.1 and the time averaged thermal energy equation can be written as:

$$0 = \underbrace{-U\frac{\partial \overline{T}}{\partial x}}_{1} + \underbrace{\frac{1}{Re_\tau Pr}\frac{\partial^2 \overline{T}}{\partial x^2}}_{2} + \underbrace{\frac{1}{Re_\tau Pr}\frac{\partial^2 \overline{T}}{\partial z^2}}_{3} - \underbrace{\frac{\partial}{\partial x}\left(\overline{T'u'}\right)}_{4} - \underbrace{\frac{\partial}{\partial z}\left(\overline{T'w'}\right)}_{5} \tag{3.42}$$

3.3.2 Case B: Mixed convection at $Re_\tau = 150$ and $Gr = 9.6 \cdot 10^5$

In this case the momentum and energy transport equations are coupled through the buoyancy term. Both streamwise and spanwise directions are homogeneous as it can be deduced from figure 2.1 and the integration of the relevant terms of the time averaged momentum equation along the z direction can be expressed as:

$$0 = \underbrace{z+\delta}_{1} + \underbrace{\frac{1}{Re_\tau} \left.\frac{dU}{dz}\right|_z}_{2} - \underbrace{\tau_w}_{3} - \underbrace{\left.\overline{u'w'}\right|_z}_{4} + \underbrace{\frac{Gr}{8Re_\tau^2}\int_{-\delta}^{z}\left(\overline{T} - T_{ref}\right) dz}_{5} \tag{3.43}$$

Similarly, the integration of the thermal energy equation leads to:

$$0 = \underbrace{\frac{1}{Re_\tau Pr}\left.\frac{d\overline{T}}{dz}\right|_z}_{1} - \underbrace{\frac{1}{Re_\tau Pr}\left.\frac{d\overline{T}}{dz}\right|_{-\delta}}_{2} - \underbrace{\left.\overline{T'w'}\right|_z}_{3} \tag{3.44}$$

3.3.3 Case C: Buoyant source line in a channel at $Re_\tau = 180$ and $Gr = 10^7$

In case C, the buoyancy acts in the wall-normal direction and only the spanwise direction remains as homogeneous. This implies that the dynamic field in this case is not fully developed. The time averaged x -momentum, z -momentum and thermal energy equations can be written, respectively, as:

$$0 = -\underbrace{\frac{\partial UU}{\partial x}}_{1} - \underbrace{\frac{\partial WU}{\partial z}}_{2} + 1 - \underbrace{\frac{\partial \overline{P}}{\partial x}}_{3} + \underbrace{\frac{1}{Re_\tau}\frac{\partial^2 U}{\partial x^2}}_{4} + \underbrace{\frac{1}{Re_\tau}\frac{\partial^2 U}{\partial z^2}}_{5} - \underbrace{\frac{\partial}{\partial x}\left(\overline{u'u'}\right)}_{6} - \underbrace{\frac{\partial}{\partial z}\left(\overline{u'w'}\right)}_{7} \tag{3.45}$$

$$\begin{aligned} 0 = -\underbrace{\frac{\partial UW}{\partial x}}_{1} - \underbrace{\frac{\partial WW}{\partial z}}_{2} - \underbrace{\frac{\partial P}{\partial z}}_{3} \quad + \quad \underbrace{\frac{1}{Re_\tau}\frac{\partial^2 W}{\partial x^2}}_{4} + \underbrace{\frac{1}{Re_\tau}\frac{\partial^2 W}{\partial z^2}}_{5} - \\ \underbrace{\frac{\partial}{\partial x}\left(\overline{w'u'}\right)}_{6} \quad - \quad \underbrace{\frac{\partial}{\partial z}\left(\overline{w'^2}\right)}_{7} + \underbrace{\frac{Gr}{8Re_\tau^2}\left(\overline{T} - T_{ref}\right)}_{8} \end{aligned} \tag{3.46}$$

$$\underbrace{\frac{\partial U\overline{T}}{\partial x}}_{1} + \underbrace{\frac{\partial W\overline{T}}{\partial z}}_{2} = \underbrace{\frac{1}{Re_\tau Pr}\frac{\partial^2 \overline{T}}{\partial x^2}}_{3} + \underbrace{\frac{1}{Re_\tau Pr}\frac{\partial^2 \overline{T}}{\partial z^2}}_{4} - \underbrace{\frac{\partial}{\partial x}\left(\overline{T'u'}\right)}_{5} - \underbrace{\frac{\partial}{\partial z}\left(\overline{T'w'}\right)}_{6} \tag{3.47}$$

Chapter 4

Parallel approach

The 3DINAMICS code was developed at the Mechanical Engineering Department by the ECoMMFiT research group [1]. The code, written in Fortran 90, was initially used to simulate forced and natural convection in cubical cavities. This code evolved to deal with more complex geometries and configurations. Currently, it is used in the Direct Numerical Simulation (DNS) of turbulent channel flows. The DNS demands high requirements in terms of memory and CPU effort even for relatively small Reynolds numbers. In order to solve accurately all the scales of the flow it is necessary to use very fine grids, specially near solid boundaries where gradients and stresses are large. Parallel computers allow to deal with such large problems by splitting the computational work between several *nodes* or *processes* working in parallel. CFD is one of the fields in which the parallelization techniques have experienced major developments in recent years. This work started with an initial parallel version of the 3DINAMICS code. This version was modified to improve its memory efficiency and a parallel multigrid solver for massive systems of linear equations was implemented.

There are several ways to classify the parallel computers but there are two crucial categories depending on how memory is used from a set of CPUs: one can find shared memory and distributed memory computers. In the former case, all processes share a large common memory containing all the data. Every process can access this memory but only one can access the same data at the same time. On the other hand, in distributed memory computers, each process has its own independent memory containing only a part of the data. This memory can not be accessed directly by any other process. If a process requires data from another one, it needs to communicate to allow the transfer (a message) of this information. Information transfer from one process to another is called *message passing*.

There is a lot of literature discussing about the advantages and drawbacks of both computer paradigms. Shared memory computers facilitate an easy programming without any need for communication. However, their scalability is limited and it is difficult to increase the number of processes existing in a shared-memory machine. When the number of processes grows, data flow between processes and the unique memory, become a bottleneck. On the other hand, distributed memory machines allow to scale the computer by adding more processes easily. The price lie in the fact that programming become more complex and tedious due to the need of communication. This is the case of the popular low-cost clusters. Figure 4.1 contains simple sketches of these two architectures.

Figure 4.1: Distributed and shared memory

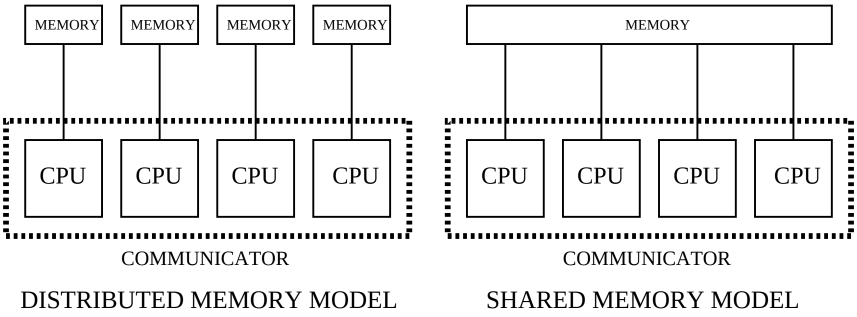

Nowadays, low cost and technological advances allow users to build relatively cheap clusters of computers mixing different type of architectures. This is the case of the cluster of the ECoMMFiT research group named *TROMA* which integrates 24 nodes AMD Opteron used for the numerical simulations presented in this study.

To develop the parallel version of the 3DINAMICS code, the MPI (Message Passing Interface) was chosen, specifically, the open source MPI-CH library. The algorithm used to solve the transport equations described in section 3 was parallelized by sharing the work load between the processes in a *communicator*.

In the domain decomposition approach the work sharing between processes is achieved by splitting a computational domain into sub-domains. Different sub-domains are then distributed over different nodes that work on its portion of data.

The processes or nodes that form a group inside which a communication occurs are called a *communicator*. Usually this parallel work can not be done in an autonomous way for every node because processes need data from other processes during calculations. So the nodes need to communicate during the work progress.

In figure 4.2 it is shown a sketch that illustrates a domain decomposition for a 2D computational grid. This can be a typical CFD case using the finite volume approach. Suppose that this domain is split into two sub-domain sharing an interface. Each node must be updated using data from the contiguous nodes in the discretization stencil. Nodes close to the interface will need data stored in the nodes in the adjacent process. It is necessary to communicate both processors through the interface to exchange their data and, consequently to create a buffer zone where transfered data is stored. The size of this zone, usually called *halo*, depends on the discretization stencil. The case shown in figure 4.2 has an halo of width 1 because it takes only one row in each sub-domain. Higher order discretization schemes make necessary to take larger halo regions in order to communicate all the values of the nodes of the halo.

Figure 4.2: Communication between processes

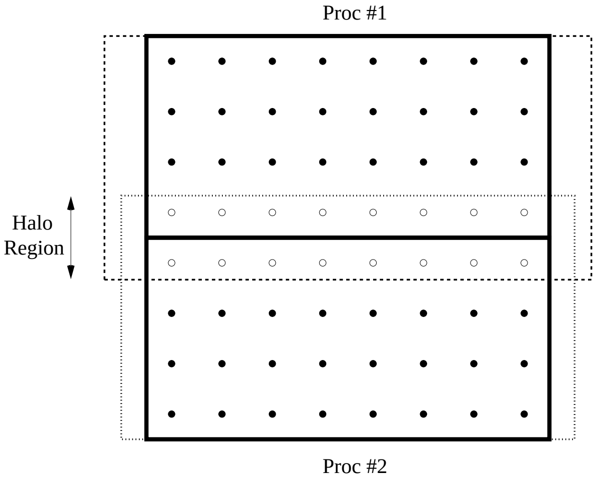

The computational domain considered in this study is Cartesian. The decomposition of the domain to assign equal work loads to each process is simply direct (small differences in the number of grid nodes in each sub-domain has no significant effect on the parallel efficiency). There are several ways to decompose the domain.

A one-dimensional decomposition was used to minimize the number of interfaces between processes although this approach requires the use of larger buffers during communications because of the larger interface. The splitting direction was chosen to avoid communications along the homogeneous directions of the flow.

To evaluate the parallel efficiency, the concept of *speed-up* needs to be introduced. This quantity is used to determine how scalable a code is. The *speed-up* is defined as:

$$S = \frac{t_{P_1}}{t_{P_n}} \tag{4.1}$$

where t_{P_1} is the computational time required by one process to perform a work load and t_{P_n} is the computational time required by n processes working in parallel to complete the same task.

A linear *speed-up* represents the ideal behavior for a parallel code. It would mean that the use of $2n$ processes to complete a task is half the time necessary to complete it using n processes. Taking into account that any communication, as a task, takes some time to complete, theoretically a linear *speed-up* is only possible if that task does not require communications to complete, so work can be completely parallelized and a process does not need any data from other processes.

Chapter 5

Multigrid techniques

The coupling between the pressure and the velocity fields in the momentum transport equations is solved in this study by using a multi-step procedure as it was presented in section 3.2. The key step of this procedure involves the solution of a Poisson-type equation (3.15). This type of equations can be rewritten in a matrix form as:

$$A\Phi = f \tag{5.1}$$

where A is the matrix coefficients and f is the source term (as it was shown in section 3, this term is proportional to the divergence of the intermediate velocity, u_i^*).

In the previous versions of the code 3DINAMICS, a Conjugate Gradient method was used to solve equation 5.1. This step took up to $50-60\%$ of the total computational time for Adams-Bashforth scheme and $35-40\%$ for Crank-Nicholson scheme. In both cases it was the most time consuming stage of the algorithm. The reduction of the CPU costs in this bottle-neck step has an important impact on the reduction of the total CPU time. In order to improve the computational efficiency of the code, a multigrid solver was implemented to substitute the conjugate gradient procedure. Multigrid methods have become very popular in scientific and engineering fields as a powerful solver for different type of massive systems of equations, specially for linear systems as those resulting from the discretization of partial differential equations using the finite-volume approach [58–61]. In addition it has been shown that multigrid techniques are less sensitive to the grid stretching [62] than other methods.

In order to introduce the multigrid methods, it is necessary to explain some definitions and concepts. The algebraic error and the residual of an approximate solution, Φ', to equation 5.1 can be defined as:

$$e = \Phi - \Phi' \tag{5.2}$$

$$r = f - A\Phi' \tag{5.3}$$

Obviously, the error is as inaccessible as the solution. The residual is a measure of the amount by which the approximation fails to satisfy the original problem $A\Phi = f$. It is also a vector and due to the uniqueness of the solution, $r = 0$ only if $e = 0$. However, it may not be true that when r is small in norm, e is also small in norm. Remembering the definition of r and e and $A\Phi = f$, it is possible to derive an important relationship:

$$Ae = r \tag{5.4}$$

Equation 5.4 indicates that the error satisfies the same set of equations as the unknown Φ when f is replaced by the residual r. This *residual equation* plays a vital role in the multigrid approach. To improve any approximation of the solution Φ', the residual equation can be solved for e and then compute a new approximation using the definition of the error:

$$\Phi = \Phi' + e \tag{5.5}$$

A large number of numerical methods to solve equation (5.1) can be found in the literature. The classical relaxation methods (Gauss-Seidel, SOR, etc) exhibit an important degradation in terms of convergence rates after a few iterations. This is due to the fact that these methods deal correctly with the high frequency components of the error vector but they experience difficulties to damp the low-frequency error components. Multigrid techniques overcome this drawback by projecting the error vector over coarser grids to convert the low frequency components to high frequency components in the coarse grids.

Thus, Multigrid techniques are based on two concepts:

- *Nested iteration*: Smoothers or relaxation solvers need an initial solution to start the iteration. In the nested iteration concept, this initial solution comes from a previous relaxation over a coarser grid for the same problem. At the same time this initial solution has been obtained from a previous relaxation on a even coarser grid.

- *Correction scheme*: Smoother or relaxation methods show a good convergence rate only for the first iterations. After that, this rate degradates as the iterative process advances. This is due to the fact that this type of smoothers deals correctly with the high frequency errors. This low amplitude errors are damped during first iterations. Low frequency errors are more difficult to reduce and the convergence rate diminishes. To correct this, the error vector is projected over a coarser grids transforming the low frequency error components in higher ones. After that, this low-level error solution can be projected back to the finer grid to obtain the final solution.

Sub-grid levels for multigrid can be generated in different ways depending on requirements. One can generate sub-grid levels from scratch taking into account that lower levels grids use to have half of nodes that the finer preceding grid [63]. On the other hand, it can be convenient to generate sub-grid levels taking the preceding grid as a reference. In 3DINAMICS, sub-grid levels have been generated by imposing a grid number of points P_N for level N as $P_N = 2^N + 2$. If the number of processes is an exact divisor of the number of grid points in a direction, this means that it is possible to build a grid hierarchy as that presented in figure 5.1. With this approach it is possible to avoid communication during the intergrid transfer steps (interpolation and projection) and only in the smoothing steps it is necessary to transfer information from neighbor processes. The drawback of this subgrid generation approach is that it is not possible to choose any arbritrary number of grid points for the original grid. It should be in the form of $2^N + 2$ and the number of processes should be an exact divisor of this number.

The iterative procedure is shown in figure 5.2. This case uses three grid levels where the top one (tagged as $N = 3$) represents the original finer grid. Level 1 represents the coarsest grid and level 2 is an intermediate grid resolution. The algorithm starts by projecting the original problem stated in equation 5.1 in the coarsest grid and solving it. Once this is done, the solution is projected to the upper level and relaxed. The residual is projected again to the coarsest level and it is solved again in terms of the residual equation 5.4. The solution is projected again to the upper level,

Figure 5.1: One-dimensional multigrid hierarchy

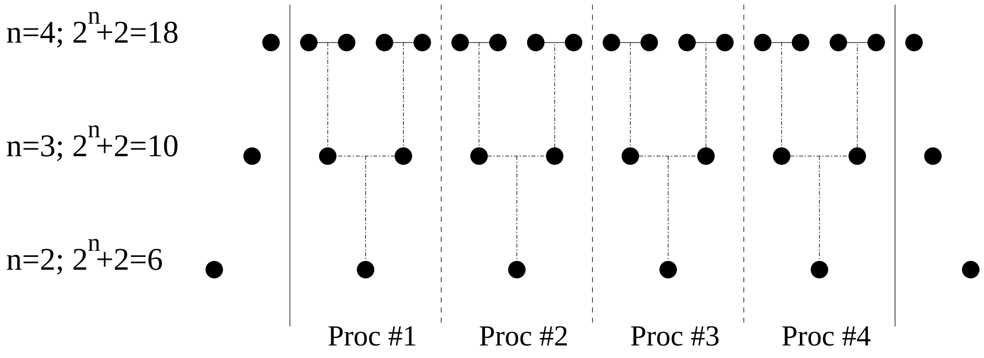

relaxed and projected finally to the finer grid level. The nested iteration provides an initial solution by relaxing the original problem on coarser levels where it has been projected. From here on, the solution is iteratively improved by relaxing over different levels of grids taking advantage of the correction scheme idea. There are different ways for visiting the grids. In figure 5.2, the *V-cycle* is illustrated. This name refers to the shape of the grid sequence path. Other common option is the *W-cycle*.

Figure 5.2: Full Multigrid with V-cycle for three levels

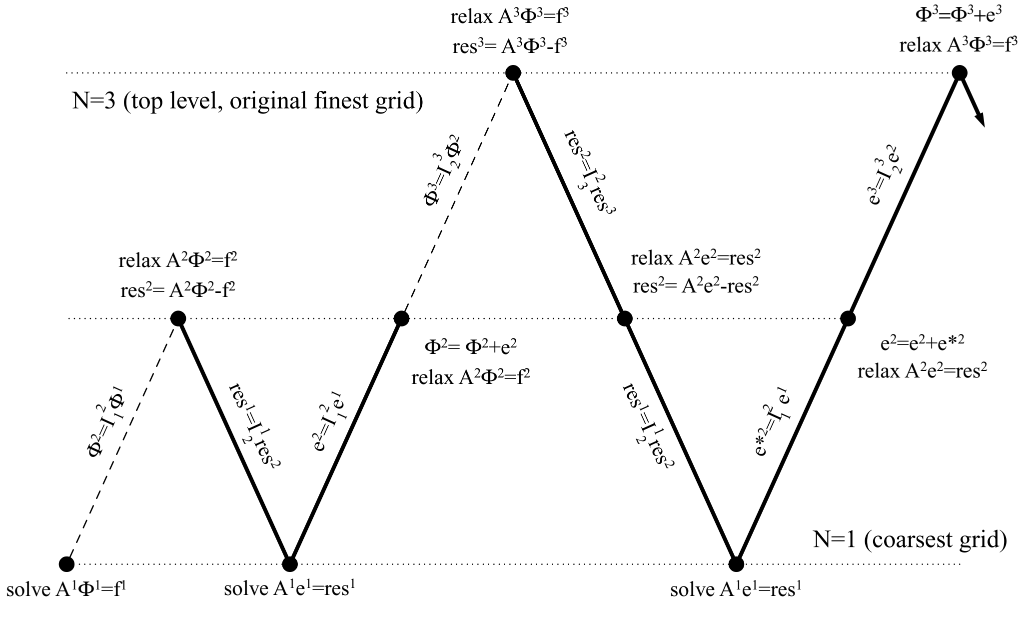

In multigrid techniques it is necessary to take some decisions. It is necessary to choose the *smoother*, the type of cycle (V, W, or even others), the number of grids, the number of relaxation sweeps to do in each grid (ν_1 and ν_2 for the downward and upward directions in the V-cycle respectively) and the transfer operators I_h^2h and I_{2h}^h (interpolation from fine-to-coarse and projection from coarse-to-fine operators respectively).

Multigrid efficiency has been compared with that of the Conjugate gradient solvers for the Poisson equation. The set of conjugate gradient solvers checked includes the standard one (henceforth CG) and the Bi-Conjugate stabilized version (Bi-CGSTAB) [64]. These solvers are conceptually very different from the *smoothers* as Gauss-Seidel or SOR. The last, finds the solution by solving iteratively the *j*th equation of the set indicated in equation 5.1 for the *j*th unknown using the current approximation for the neighbor unknowns. This is an example of *stationary linear iteration*. On the other hand, the conjugate gradient methods transform the problem stated in equation 5.1 into a minimization problem where the minimum value of the target function (derived from the quadratic form of the original problem) is equal to the solution of the linear system of equations. The basic idea in which CG is based deals with the finding of the steepest direction in the minimization function and to advance iteratively until the solution is reached. The key point is how to find such search direction and how large are the steps to advance towards the solution. The set of search directions are chosen to be *A*-orthogonal (where *A* refers to the coefficient matrix) or *conjugate* and can be generated by a *Conjugate Gram-Schmidt process*.

The CG method may not be suitable for non-symmetric systems because the residual vectors cannot be made orthogonal with short recurrences. The biconjugate gradient method (Bi-CG) uses another approach. It replaces the orthogonal sequence of residuals by two mutually orthogonal sequences. Few theoretical results are known about the convergence of the Bi-CG method. For symmetric positive definite systems, the method delivers the same results as the CG method, but with twice the cost per iteration. For non-symmetric matrices, it has been shown that in phases of the process where there is significant reduction of the norm of the residual, the method is more or less comparable to the full generalized minimal residual method (GMRES) in terms of numbers of iterations [65]. However, in practice, it has been observed that the convergence behavior may be quite irregular, and the method may even break down. Finally, the biconjugate gradient stabilized method (Bi-CGSTAB) appears as a suitable method to solve non-symmetric problems avoiding the irregular convergence patterns of other CG versions.

The convergence criteria for the comparison of the different methods can be written as,

$$\frac{||A\phi' - f||}{||f||} \leq 10^{-3} \tag{5.6}$$

The test has been performed considering two synthetic cases and the turbulent fully developed plane channel flow. The two synthetic cases correspond to a case with Dirichlet (fixed value) boundary conditions and another case with Neumann (null derivative) boundary conditions. In the synthetic cases the source terms f have been chosen in order to obtain analytical solutions for Φ. Those solutions have been obtained because of the simplicity and smoothness of the sources terms. On the other hand, the source term in a simulation of a turbulent flow resulting from the divergence of the intermediate velocity vector u_i^* is more complex.

The availability of analytic solutions for the synthetic cases allows to check the numerical results. Both synthetic cases have been solved for Cartesian uniform and non-uniform grids. The node locations for non-uniform grids in synthetic cases have been generated using a geometric progression which is controlled by a geometric parameter r. The larger the parameter, the larger degree of stretching on grid is obtained. Excessive stretching may lead to numeric instabilities and convergence problems so values $r < 1.2$ are recommended.

This geometric parameter r is defined as:

$$r = \frac{x_{i+1} - x_i}{x_i - x_i - 1} \qquad i = 2, 3, ..., ni - 1 \tag{5.7}$$

The grid resolution for these synthetic cases is 130 × 130 × 130 (almost 2.2 million grid points). Note that a much smaller grid resolutions lead to small work load/communication ratios. The fraction of the computational time devoted to communication between processes may represent a large fraction of the total time or even the most important part. Parallel computing only has sense when work loads are large enough to take advantage of the parallel work despite the lagging in communication.

Much larger grid resolutions would not be in the resolution range of the CFD problems currently solved and it would require prohibitive CPU and memory requirements.

For the fully developed channel flow it has been considered only the computational times used to solve the Poisson equation in the CFD code so it does not correspond to a complete time step but only to the pressure correction part. The grid resolution in this case is $258 \times 130 \times 130$ and the source term is generated with the divergence of the intermediate velocity as shown in equation 3.15. For this case, the solution of the linear system corresponds to the pressure correction field as explained in chapter 3.

- Synthetic case: Dirichlet boundary conditions

  In the case of Dirichlet boundary conditions the constant source term for the domain $\Omega[0,1]$ is:

  $$\frac{\partial^2\Phi}{\partial x^2}+\frac{\partial^2\Phi}{\partial y^2}+\frac{\partial^2\Phi}{\partial z^2}=Q=-1 \tag{5.8}$$

  where Q is the source term. All boundary values are set to zero.

  With these boundary conditions, the corresponding analytical solution is:

  $$\Phi(x,y,z)=\sum_{n=1}^{\infty}\sum_{m=1}^{\infty}\sum_{p=1}^{\infty} b_{nmp}\, sin\frac{n\pi x}{L_x} sin\frac{m\pi y}{L_y} sin\frac{p\pi z}{L_z} \tag{5.9}$$

  where L_x, L_y and L_z are the dimensions of the domain and the term b_{nmp} is defined as:

  $$b_{nmp} = \frac{-1}{\lambda_{nmp}}\frac{\int_0^{L_z}\int_0^{L_y}\int_0^{L_x} Q\,sen(n\pi x/L_x)sin(m\pi y/L_y)sin(p\pi z/L_z)dx\,dy\,dz}{\int_0^{L_z}\int_0^{L_y}\int_0^{L_x} sen^2(n\pi x/L_x)sin^2(m\pi y/L_y)sin^2(p\pi z/L_z)dx\,dy\,dz} \tag{5.10}$$

  where

  $$\lambda=\left(\frac{n\pi}{L_x}\right)^2+\left(\frac{m\pi}{L_y}\right)^2+\left(\frac{p\pi}{L_z}\right)^2 \tag{5.11}$$

  Finally the solution can be written as,

$$\Phi(x,y,z) = \sum_{n=1}^{\infty}\sum_{m=1}^{\infty}\sum_{p=1}^{\infty}\frac{8}{\lambda}\,\frac{\big(1-cos(n\pi)\big)\big(1-cos(m\pi)\big)\big(1-cos(p\pi)\big)}{nmp\pi^3}\; sin\frac{n\pi x}{L_x} sin\frac{m\pi y}{L_y} sin\frac{p\pi z}{L_z} \tag{5.12}$$

- Synthetic case: Neumann boundary conditions

  For the Neumann boundary conditions case, the source term for the domain $\Omega[-\frac{1}{2},\frac{1}{2}]$ was chosen as:

$$\frac{\partial^2\Phi}{\partial x^2}+\frac{\partial^2\Phi}{\partial y^2}+\frac{\partial^2\Phi}{\partial z^2} = 24x+24y+24z \tag{5.13}$$

  The corresponding analytical solution with $\frac{\partial\Phi}{\partial x_i}=0$ at $x_i = \frac{-1}{2},\frac{1}{2}$ is:

$$\Phi(x,y,z) = 4(x^3+y^3+z^3)-3(x+y+z) \tag{5.14}$$

  It is important to note that when all boundary conditions are Neumann-type the problem may be not well-posed [66]. If the problem has a solution, this is not unique because the system involves only derivatives of Φ. If a solution exist, then the source term f must satisfy:

$$\int_V f(x,y,z)dV = 0 \tag{5.15}$$

  This *compatibility condition* is necessary for a solution to exist [66]. This condition has been introduced in the multigrid approach to obtain a well-posed problem. This means that the term $f(x,y,z)$ must fit the compatibility condition expressed in equation 5.15 in its discrete form for a grid h:

$$\sum_{i,j,k}^{NI,NJ,NK} f_h(x_i,y_j,z_k)dx_i dy_j dz_k = 0 \tag{5.16}$$

  In each grid the term f_h can be substituted by $\overline{f_h}$:

$$\bar{f_h} = f_h - \sum_{i,j,k}^{NI,NJ,NK} f_h(x_i, y_j, z_k) dx_i dy_j dz_k = 0 \tag{5.17}$$

On the other hand, an integration constant must be set in order to found a unique solution. To save computational CPU time this procedure is only applied in the coarsest levels [66]:

$$\sum_{i,j,k}^{NI,NJ,NK} \Phi_h(x_i, y_j, z_k) dx_i dy_j dz_k = 0 \tag{5.18}$$

The results comparing the different solvers tested include the *speed-up* value and the CPU time in seconds.

Results in terms of *speed-up* are shown in figure 5.3 for equation 5.8 (a and b) and equation 5.13 (c and d) with an uniform grid (b and d) and with a non-uniform grid (a and c).

The linear *speed-up* has been introduced in figure 5.3 for comparison. This linear profile indicates the ideal situation where there is no loss of efficiency due to communication and the work load is perfectly shared between the processes. The communications between processes and, to a lesser extent, the network latency and the imbalanced work load between processes are responsible for deviations from this ideal approach.

It is important to note that there is a basic difference between the algorithms for the standard CG and the Bi-CGSTAB methods. The second one preconditionates the function matrix and this represents an additional matrix-vector product which implies additional operations per iteration and, consequently, additional communications. In other words, Bi-CGSTAB usually solves the same problem as CG with more CPU operations (and consequently communications) but the number of iterations can be smaller depending on the problem.

Results are presented in figure 5.4 in terms of CPU time (in seconds).

Using 8 processes to solve any of the synthetic cases, the value of *speed-up* for multigrid is between 2 and 3 while it is between 4 and 6 for the conjugate gradient methods (see figure 5.4). For uniform grids the CG requires smaller CPU times than the Bi-CGSTAB but in terms of *speed-up* the last one is better (see figures 5.3b,d

Figure 5.3: Speed-up for different Poisson solvers

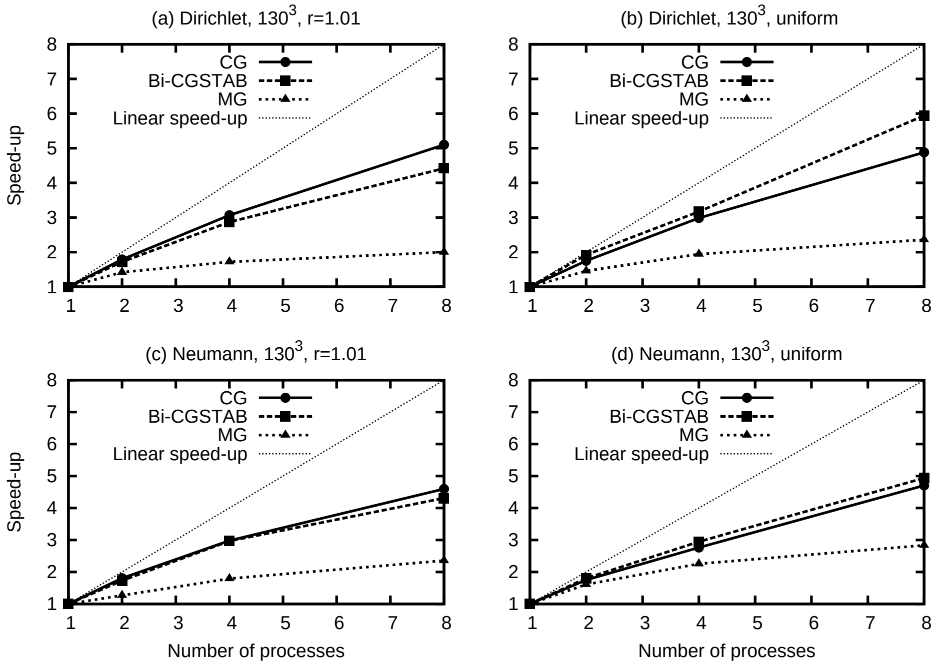

and 5.4b,d). In fact, a *speed-up* value of 6 for the Dirichlet case with uniform grid is the highest obtained in this analysis. This situation is opposite for the synthetic cases using non-uniform grids. The Bi-CGSTAB, more suitable for non-symmetric matrices, is between 1.1 and 1.7 times faster than the CG but its *speed-up* is not as good as that found for the CG (see figures 5.3a,c and 5.4a,c).

Scalability differences between the CG and the Bi-CGSTAB are small for the Neumann boundary conditions problems for uniform and non-uniform grids. For Dirichlet boundary conditions this differences are more significant. Note that CPU time scale in figure 5.4 is logarithmic, so results for these two methods have to be read carefully because differences may seem smaller.

For the channel flow case, the grid resolution corresponds to that used in cases A and C ($258 \times 130 \times 130$) so the comparison gives realistic and practical information about the computational costs of these simulations. It is important to note that this grid resolution is the double than that used in the synthetic cases. Another important difference between the channel flow case and the synthetic cases lies in the nature of the source term in equation 5.1. For the synthetic cases the source term is a

Figure 5.4: CPU time (seconds) comparison for different Poisson solvers

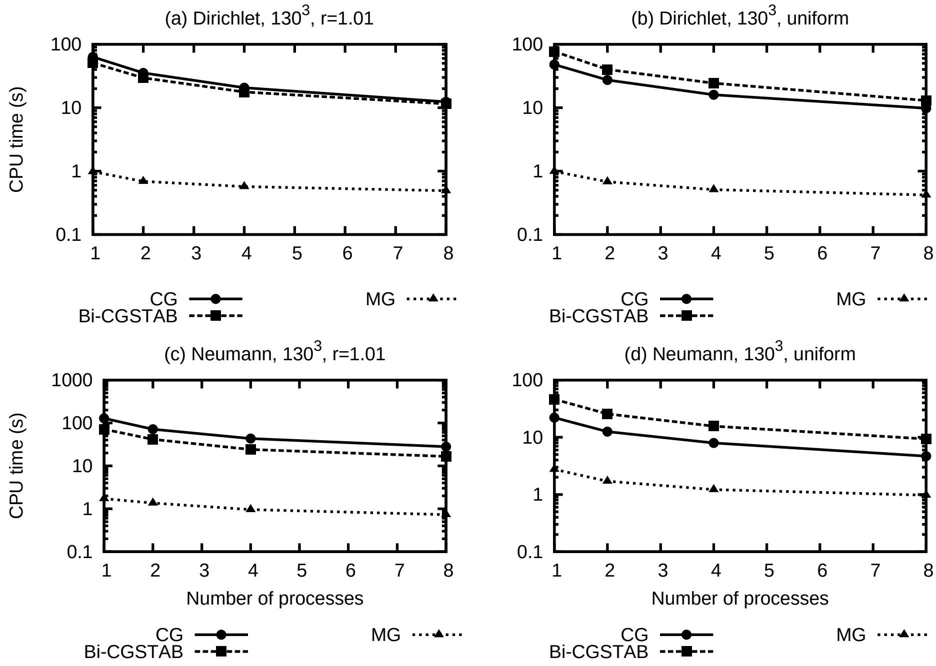

smooth function with very large scales while in the channel case it comes from the divergence of a turbulent velocity field with large range of scales. This is the reason because the computational CPU times are larger than in the synthetic cases (see figures 5.4 and 5.5b). For instance, for the synthetic case with Neumann boundary conditions and a non-uniform (which is the most similar to the pressure calculation in term of boundary conditions type and grid stretching), the CPU time required by Bi-CGSTAB was about 16 CPU seconds using 8 processes and 28 for CG). For the pressure calculation in the fully developed channel flow, the CPU times for these methods were approximately 25 and 129 seconds respectively. For multigrid, the synthetic case took 0.7 seconds of CPU time and the pressure calculation used 7 seconds approximately. In terms of *speed-up*, the results are quite similar to those obtained for the synthetic cases. The CG has the best scaling factors and multigrid is the fastest solver although it shows again the smallest scaling factors.

For all the cases studied, both conjugate gradient methods scale much better than multigrid. This is due to the fact that the number of calls for communication tasks is much larger in the multigrid algorithm than in the conjugate gradient solvers. The multigrid solver core is a *smoother* (SOR in this case [67]) so it needs to perform a sweep to update solution and it is required to communicate the data located in the halo regions. At the beggining of the nested iteration procedure, the problem has to be solved accurately at the coarsest grid. Although the number of grid points at this level is small, it still requires a large number of sweeps to meet the convergence criteria. The number of sweeps required at the next solver stages in the coarsest grid are continously smaller because the solution is progressively improved. The number of sweeps in the relaxing steps is very small (typically $\nu_1 + \nu_2$ is less than 10) but the grid resolutions are finer and consequently the communication buffers are larger. However, the CPU times for multigrid are smaller than those corresponding to conjugate gradient solvers as shown comparing figures 5.4 and 5.5b. Factors around 10 are common and larger factors are possible especially for Dirichlet cases. This means that solving a Poisson equation with multigrid is much more efficient than using conjugate gradient methods in terms of CPU time for a given communicator.

Figure 5.5: Comparison of different solvers for the pressure equation in the channel configuration

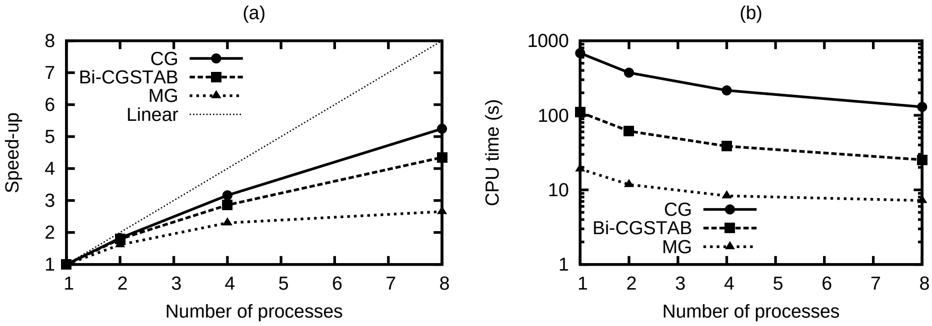

Previous results for this comparison showed *speed-up* values of multigrid smaller than one. For a certain number of processes, the CPU time required to perform a task was larger than that required for a smaller number of processes. The reason was that the communication time was extremely large. This was solved using the hierarchy shown previously in figure 5.1 because this approach allows to eliminate communications in the intergrid operations. The grid transfer of a vector from a fine to a coarse grid is clearly direct without any communication because all grid coarse nodes lie between fine grid nodes. However, in the inverse procedure, all fine grid nodes lie between coarse grid points except those in the halo region. To interpolate over this nodes one would require information from adjacent nodes implying communication. Such problem can be solved by assigning to this halo points in the fine grid the injected value coming from the closest coarse grid nodes. The error associated with this approximation is corrected in the relaxation stages.

Finally to summarize, multigrid solvers efficiency and robustness depend mainly on [68]:

- Number of grid levels and number of relaxation sweeps on each level
- Interpolation operators used in inter-grid transfers
- Type of *smoother* (points, lines, planes, over-relaxation, etc)
- Coarse grid generation strategy
- Grid anisotropy and type of boundary conditions

Chapter 6

Results and discussion

In this chapter, the numerical results for the different flow configurations considered in this study are presented and discussed. The validation of the code has been performed by comparison with data avaliable in the literature.

The turbulent flows considered in this study include:

- Base case: Fully developed channel flow at $Re_\tau = 150$
- Case A: Scalar line source in a channel at $Re_\tau = 180$
- Case B: Mixed convection at $Re_\tau = 150$ and $Gr = 9.6 \cdot 10^5$
- Case C: Buoyant source line in a channel at $Re_\tau = 180$ and $Gr = 10^7$

6.1 Base case: Fully developed channel flow at $Re_\tau = 150$

The size of the computational domain is $4\pi\delta \times 2\pi\delta \times 2\delta$ along the streamwise, spanwise and normal to the walls directions, respectively. The streamwise (x) and spanwise (y) directions are homogeneous so periodic boundary conditions have been applied for the hydrodynamic variables (velocity and pressure). No-slip and Neumann boundary conditions have been implemented on the walls for velocity and pressure respectively. The grid has a resolution of $129 \times 121 \times 121$ points and has been stretched near walls using a logarithmic transformation [69]. The minimum scalar finite volume size is $\Delta z^+_{min} = 0.3$ for the finite volumes located adjacent to the wall, where superscript '$+$' indicates non-dimensional wall coordinates defined in equation 6.1. The non-dimensional time step for time integration has been set to $\Delta t = 10^{-3}$.

$$x_i^+ = x_i \frac{u_\tau}{\nu} = x_i{}^* Re_\tau \tag{6.1}$$

Stretched grids allow to capture the smallest turbulent scales near the wall by using higher resolution inside the boundary layer where gradients and stresses are larger. The flow has been initialized using previous results for fully-developed channels.

The Reynolds number based on the bulk velocity and the channel width is $Re_{2\delta} = 4546$ and the friction factor (defined in equation 6.2) is $C_f = 0.0088$. These results are in agreement with DNS of Iwamoto [70] who reported $Re = 4560$ and $C_f = 0.0087$ at the same Reynolds number.

$$C_f = \frac{\tau_w}{\frac{1}{2}\rho U_b^2} = \frac{2}{Re_\tau U_b^{*2}} \left.\frac{\partial U^*}{\partial z^*}\right|_w \tag{6.2}$$

Figure 6.1 shows the mean streamwise velocity profile and the root-mean-square (r.m.s.) for the three velocity components. These results are compared with previous DNS [70] showing good agreement as can be seen in figure 6.1. It should be noted that Iwamoto [70] performed the simulations with a spectral code with a resolution of 128 modes along the homogeneous directions of the flow and a grid of 97 along the normal to the wall direction with a domain size of $5\pi\delta \times 2\pi\delta \times 2\delta$. This can explain the slight differences observed in figure 6.1b.

6.2 Case A: Scalar line source in a channel at $Re_\tau = 180$

This case is similar to the previous one with periodic boundary conditions for hydrodynamic variables along the homogeneous directions and no-slip boundary conditions on the walls. However, Re_τ is now 180 so the grid resolution has been increased. The scalar transport can be modeled using the energy equation 1.20 where temperature T stands for a passive scalar so the buoyancy effect is neglected. At the inlet of the computational domain the source line is implemented as a spanwise band centered in the vertical direction injecting the scalar on the horizontal

Figure 6.1: Mean (a) and (b) r.m.s. profiles for pressure-driven channel at $Re_\tau = 150$

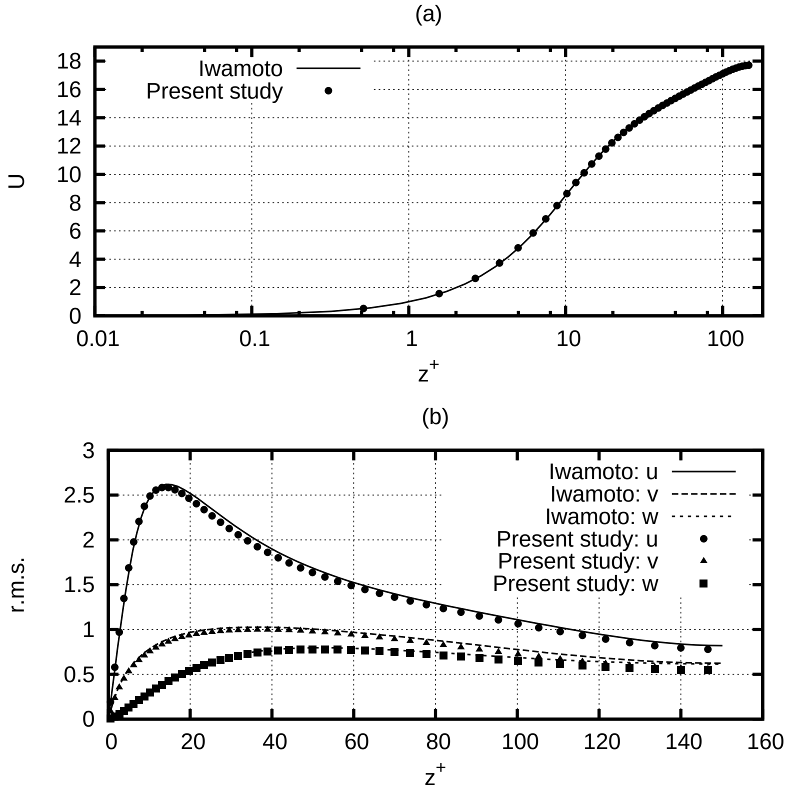

midplane of the channel.

The size of the domain is $8\pi\delta \times 2\pi\delta \times 2\delta$ with a grid resolution of 258 × 130 × 130 (4.360.000 points approximately). The Prandtl number is set to 0.71. The time step for integration has been set to $\Delta t = 5 \cdot 10^{-4}$. The statistical quantities have been obtained after averaging for a time period of $60t^*$.

Interpolated results from an instantaneous flow field at $Re_\tau = 150$ case have been used as initial conditions.

Figure 6.2 shows a slice at $x = 12$ with the instantaneous velocity field over the corresponding pressure field for the channel flow at $Re_\tau = 180$.

An instantaneous temperature field slice at $y = 0$ is shown in figure 6.3. It can be seen how the temperature is dispersed in the channel forming a non-buoyant plume. Close to the source, it can be observed clearly the meandering of the plume. At this stage the width grows as in an homogeneous flow. At large x positions, it is possible

Figure 6.2: Instantaneous velocity and pressure fields at $Re_\tau = 180$

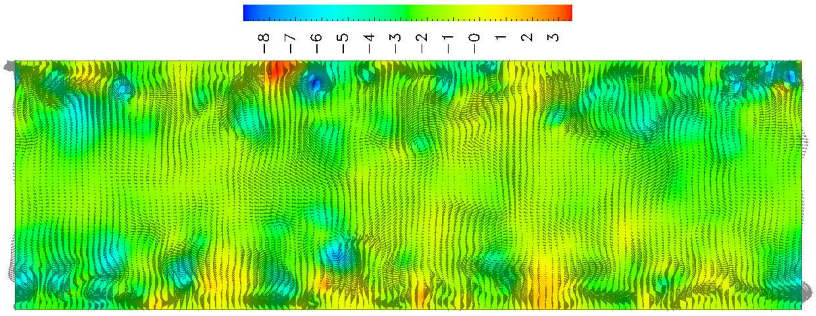

to see the effect of turbulent mixing forming complex structures and the effect of the inhomogeneity induced by the walls on the plume dispersion. Color range is not linear to highlight details.

Figure 6.3: Instantaneous temperature field from a line source at $Re_\tau = 180$

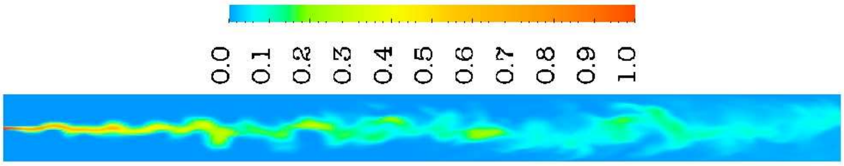

Figure 6.4 shows the mean velocity profile compared with DNS of a fully developed channel flow at $Re_\tau = 180$ reported by Iwamoto [70]. This author used a grid resolution of $128 \times 128 \times 128$ with a domain size of $12.8\delta \times 6.4\delta \times 2\delta$. Slight differences that can be observed in figure 6.4 can be explained due to the fact that Iwamoto [70] use spectral methods to solve the momentum equations in the homogeneous directions.

Figure 6.5 shows the comparison between the present predictions of the plume half-width and mean centerline scalar decay and DNS performed by Brethouwer and Nieuwstadt [38] and Vrieling and Nieuwstadt [32].

Figure 6.4: Mean (a) and r.m.s. (b) velocity profiles

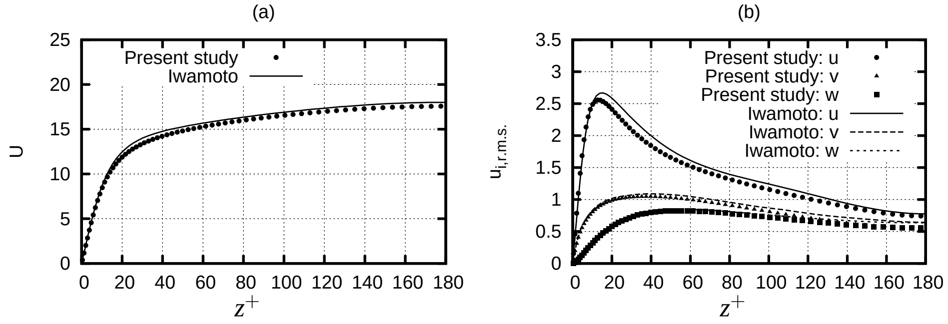

Brethouwer and Nieuwstadt [38] simulated the flow field in a fully developed channel flow with a vertically centered line source at $Re_\tau = 180$ and $Sc = 0.7$ with a grid resolution of $225 \times 120 \times 78$ in a computational domain with sizes $10\delta \times 6\delta \times 2\delta$ in the streamwise, spanwise and wall-normal directions respectively. These authors also considered the simulation of a scalar field with chemical reaction with a line source near the wall. In this case the computational domain was expanded up to $30\delta \times 6\delta \times 2\delta$ by periodic extension of the flow field.

Vrieling and Nieuwstadt [32] used a grid resolution of $150 \times 96 \times 150$ in a computational domain with sizes $10\delta \times 6\delta \times 2\delta$ in the streamwise, spanwise and wall-normal directions respectively to simulate dispersion and chemical reactions for a vertically centered single source in a fully developed channel at $Re_\tau = 180$ and $Sc = 1.0$. These authors used larger domain sizes and resolutions for the simulations considering two source lines.

It is important to note that Brethouwer and Nieuwstadt [38] considered a smaller size for the line source ($H_S = 0.028\delta$) than that used in this study ($H_S = 0.054\delta$). This would explain the smaller half-width predicted by Brethouwer and Nieuwstadt [38] for the formed plume in comparison with that of the present results as shown in figure 6.5b. However the evolution of the plume half-width agrees with that reported by Vrieling and Nieuwstadt [32] who considered a Gaussian line source with width $\sigma_0 = 0.04$. Also the similar grid resolution used along the wall normal direction of the present simulation and of Vrieling and Nieuwstadt [32] can explain the different trends of σ along the streamwise direction in figure 6.5b of these two simulations in comparison with that of Brethouwer and Nieuwstadt [38].

The mean centerline temperature decay rate for homogeneous turbulence is well described by a power law of the form $\overline{T}/T_0 \propto (x/h)^n$ according to Karnik and Tavoularis [15]. The fit of the present results to this power law, gives a value $n = -0.6$ which is the same than that reported by Lavertu and Mydlarsky [33]. This value is smaller than that obtained for homogeneous turbulence for which $n = -0.75$ to -1.0 for distances $x/M \geq 1$ where M is the mesh length of the turbulence-generating grid. These authors suggest that at larger values of x the exponent n should decrease to values of the order of -0.5 [9].

The present prediction of the rate of the decay of the mean centerline temperature shown in figure 6.5a differs slightly from that of Vrieling and Nieuwstadt [32] probably because these authors used a Gaussian profile for the source in order to avoid or minimize non-physical oscillations associated with large scalar gradient values near the source.

Figure 6.5: Mean centerline decay (a) and half-width plume (b) for temperature

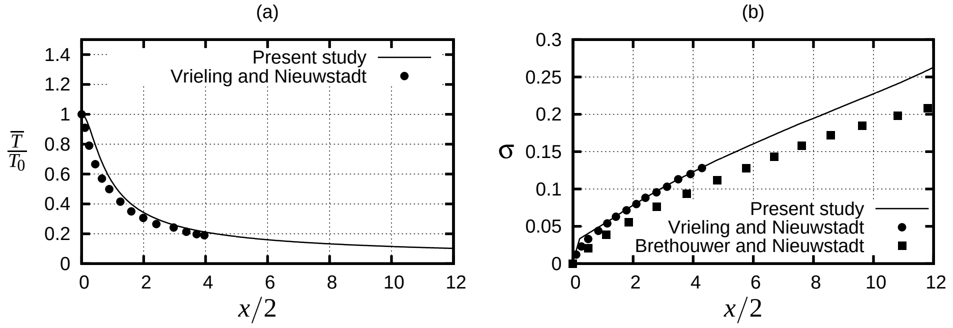

Figure 6.6 shows the comparison of the r.m.s. profiles with numerical results of Brethouwer and Nieuwstadt [38] and experiments carried out by Sawford and Sullivan [71]. These authors measured the dispersion in grid generated turbulence. The homogeneous turbulent flows (as those obtained using grid turbulence) show double peaks in the r.m.s. profiles far downstream as shown in figure 6.6. The non-homogeneity in wall-normal direction introduced in channel flows does not show this feature tending to exhibit a single peak in the r.m.s. profiles as the distance downstream increases [33]. On the other hand, the reason why Brethouwer and Nieuwstadt [38] r.m.s. profiles do not show peaks can be attributed to the fact that the size of their source is smaller (0.028δ) than that considered in this study

(0.054δ).

Figure 6.6: Temperature r.m.s. profiles

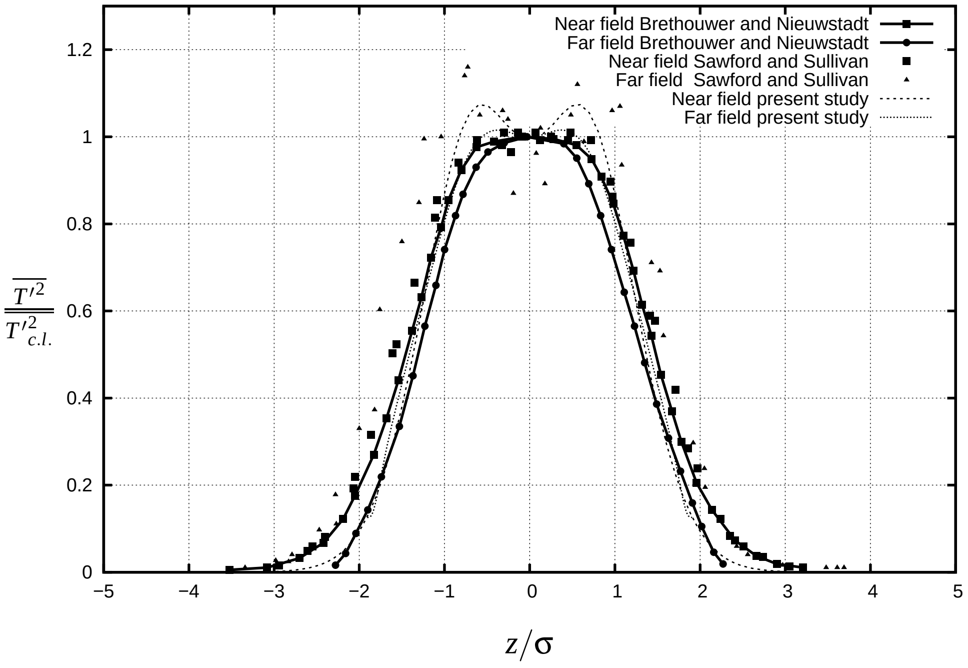

Figure 6.7 shows the mean profiles of the relevant terms of the time averaged x-momentum equation (3.40). The numbers in the label of this figure indicate the different terms of the equation 3.40. Note that the terms have been moved to the right hand side of the equation 3.40 to plot their contribution in figure 6.7. Without the buoyancy effect, the pressure gradient is balanced by friction on the walls as it can be seen from integration of the mean momentum equation over the channel width. Figures 6.8 to 6.10 show the budget of the time averaged thermal energy equation (3.42) at different three selected x positions. The mean temperature profiles scaled and shifted for clarity have also been included in these figures. It is important to note that all the relevant terms of the balance equations have been written on the right hand side so the signs have changed accordingly (see equations 3.40 to 3.47).

The contribution of the different terms to the thermal energy budget at $x = 6.0$ are shown in figure 6.8. This streamwise position corresponds to the zone where inhomogeneities from the walls are not important. The main terms are the streamwise convective transport and the wall-normal turbulent transport with only a relatively small contribution of the conductive term along the wall-normal direction. This last term decreases in magnitude as the distance from the source is increased along the streamwise direction because the mean temperature gradient decreases as well.

Far from the walls, the turbulent term in the wall-normal direction, $\partial\left(\overline{w'T'}\right)/\partial z$, is zero at $z = \pm 0.17$ as shown in figure 6.8. The turbulent heat flux $\overline{w'T'}$ has zero value at the walls because there the velocity fluctuations are zero. As it can be seen in figure 6.8, the gradient of $\overline{w'T'}$ along the wall-normal direction is negative from the lower wall up to $z = -0.17$. This means that, starting from the lower wall where its flux value is zero, $\overline{w'T'}$ decreases continously reaching a minimum at $z = -0.17$. For $z > -0.17$ the gradient is positive so the turbulent flux grows reaching a maximum at $z = 0.17$. At the upper wall its value in again zero.

This is explained because in the lower half of the channel a positive fluctuation of w implies the entrainment of fresh cold fluid in the plume and the consequent decrease in temperature. Inversely, in the upper half a positive velocity fluctuation of w produces an increase of the temperature. The streamwise convective term is also zero at $z = \pm 0.17$. This corresponds to the positions where the mean temperature gradient along the streamwise direction is zero.

The wall-normal diffusion term also vanishes at location $z = \pm 0.17$. This imply that the second derivative for the mean temperature in the wall-normal direction is zero indicating the inflection point of the profile.

This behavior can also be observed at the other two streamwise positions considered, $x = 12.5$ and $x = 24.0$, and shown in figures 6.9 and 6.10 respectively. However, as the plume disperses downstream, this position shifts towards the walls. It is located at $z = \pm 0.26$ and $z = \pm 0.4$ for $x = 12.5$ and $x = 24.0$, respectively.

Figure 6.9 shows the profiles located at the middle of the streamwise dimension of the computational domain. At this position, $x = 12.5$, the plume reaches the walls as can be deduced from the temperature profile as well as the profiles of the turbulent transport term. The distribution of the different terms is similar to the previous one profiles but profiles are wider in the wall-normal direction and their intensity has decreased.

Figure 6.10 shows the profiles at a streamwise position where the walls affect considerably the plume structure. The streamwise convection and turbulent transport terms are again the most important contributions to the thermal energy budget.

It is possible to observe two peaks near walls for the normal diffusive term in figure 6.10. This can be explained because near the walls, as it can be observed in figure 6.10, the molecular conduction is responsible for the decrease of the turbulent wall-normal transport and, consequently, the conductive transport becomes more important in the overall balance. This peak of the diffusive wall-normal term is greater in magnitude than the values found within the flow of the channel.

Figure 6.7: Mean x-momentum transport balance

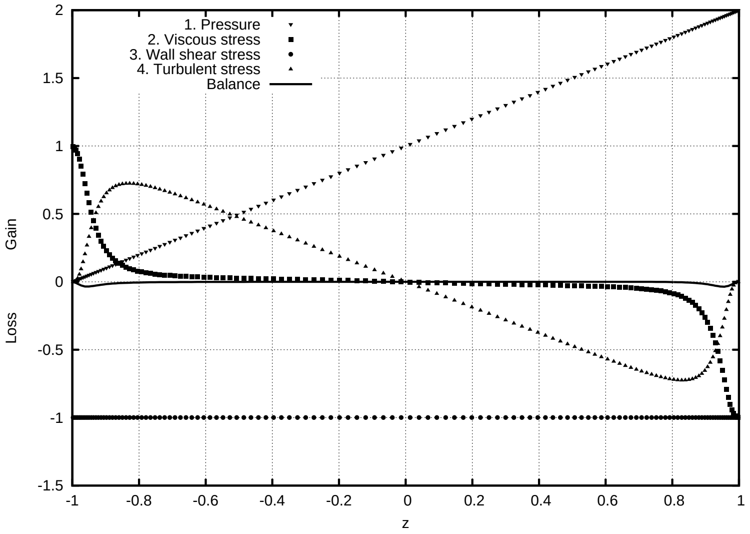

Figure 6.8: Mean heat transport balance at x=6.0

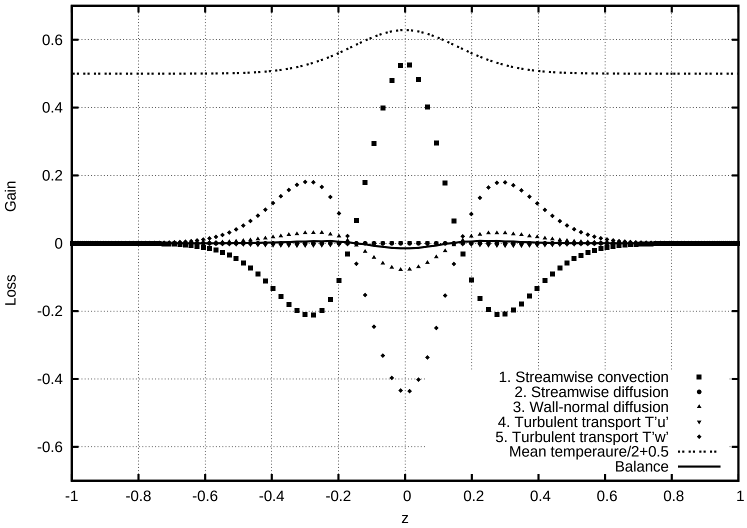

Figure 6.9: Mean heat transport balance at x=12.5

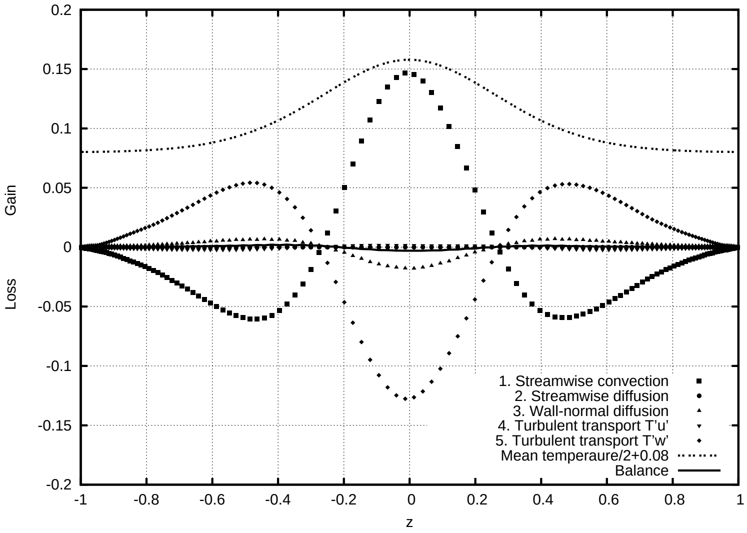

Figure 6.10: Mean heat transport balance at x=24.0

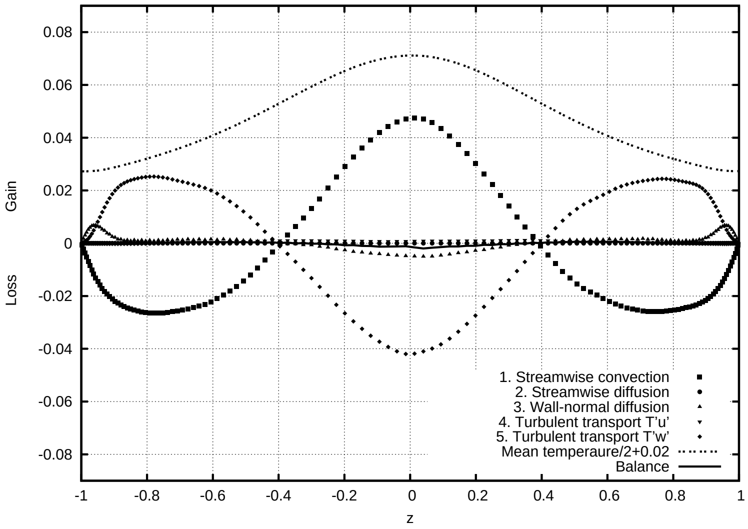

6.3 Case B: Mixed convection at $Re_\tau = 150$ and $Gr = 9.6 \cdot 10^5$

This flow is also a fully developed turbulent channel flow with the gravity vector oppositely aligned with the streamwise direction in a vertical channel. In this case, the buoyancy term in equation 1.8 is not zero. The reference temperature corresponds to the average between the hot and the cold walls fixed at $T(x,y,-\delta,t) = T_H^* = 1$ and $T(x,y,\delta,t) = T_C^* = 0$ respectively. The buoyancy effect aids or opposes to the mean pressure gradient depending on the location within the fluid. The molecular Prandtl number is 0.71 and the Grashof number is $Gr = 9.6 \cdot 10^5$. The size of the domain is $8\pi\delta \times 2\pi\delta \times 2\delta$ along the streamwise, spanwise and normal to the walls directions respectively. The boundary conditions for velocity and pressure fluctuation are the same as in case A.

The grid resolution is $131 \times 101 \times 101$ with a minimum finite volume size $\Delta z^+_{min} = 0.3$ near the walls of the channel. The time step for time integration has been set to $\Delta t = 1 \cdot 10^{-3}$. The flow statistics have been averaged when the flow was fully developed during a period of 200 non-dimensional time units.

Figure 6.11: T_{ref} isosurface

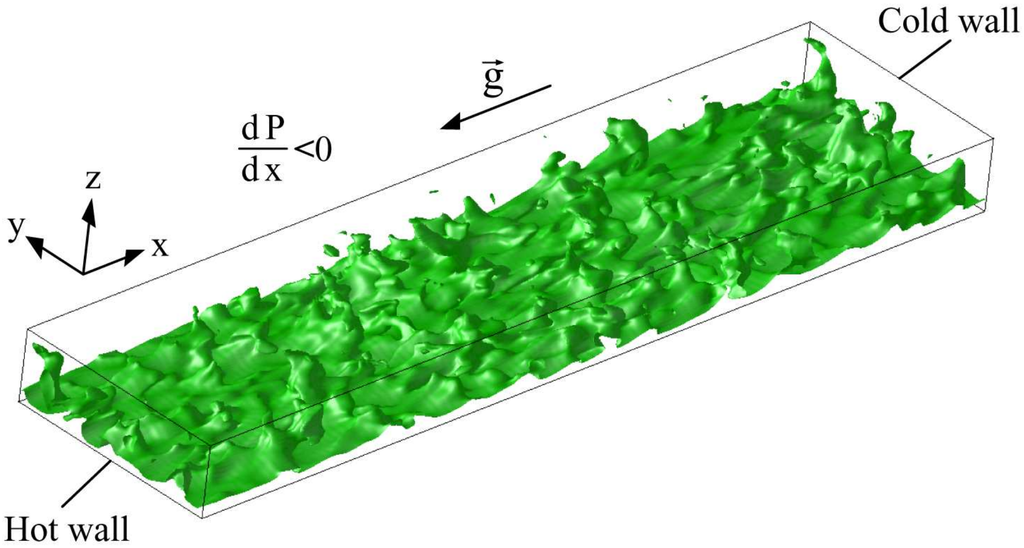

The hydrodynamic variables have been initialized using instantaneous fields of case A. The temperature field is initialized as a constant temperature field at T_{ref}. The initialization of temperature field with a linear mean profile between walls has been observed to demand high computational resources. It has been found that for mixed convection cases a very large domain is needed in the vertical (streamwise) direction. If a smaller box is used no quasi-steady conditions are obtained, and the bulk velocity varies with a very low frequency [43]. The mean temperature also fluctuates at a very low frequency. The computational requirements increase with the Grashof number [72]. Among all benchmark cases considered, this one is the most costly in terms of CPU time since it took a long time to achieve the fully developed flow conditions. As an example of the instantaneous temperature field, figure 6.11 shows the isosurface of T_{ref} and figure 6.12 shows instantaneous temperature contours at $y = 0$. It can be seen in figure 6.12 the hot region in red (buoyancy aided flow) and the cold in blue (buoyancy opposed flow). It also can be seen in the central region of the channel the different effect of buoyancy near the two walls. Note that the color scale is not linear to enhance the details of the temperature distributions in the central region of the channel where the temperature differences are small because of the turbulent mixing.

Figure 6.12: Instantaneous temperature field for mixed convection at $Re_\tau = 150$ and $Gr = 9.6 \cdot 10^5$

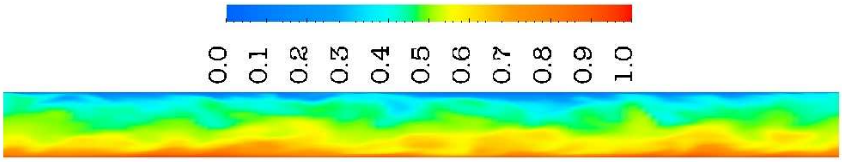

Results for the mean and r.m.s. temperature profiles are shown in figure 6.13 and the mean streamwise velocity and r.m.s. profiles are shown in figure 6.14.

The results show a good agreement with those of avaliable literature [73] as shown in figures 6.13 and 6.14. The mean temperature gradients at the walls are the same and thus the macroscopic heat balance is satisfied. Some relevant mean quantities are presented in table 6.1. The values in parentheses correspond to DNS results reported by Davidson et al. [73]. The largest differences between these values are

Figure 6.13: Mean (a) and r.m.s. (b) temperature profiles

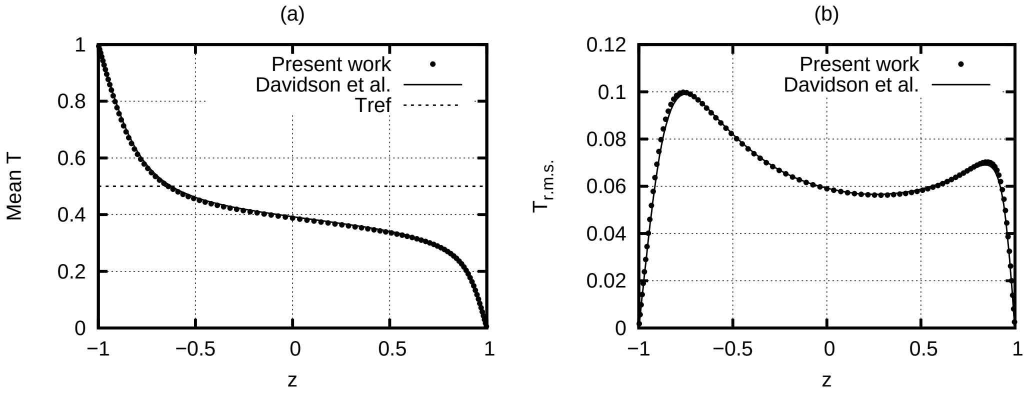

Table 6.1: Mixed convection relevant quantities

$\tau_{w,-\delta}$	$\tau_{w,\delta}$	U_b	T_b	u_*	$-\left(\partial\overline{T}/\partial z\right)_w$	Re_b
0.68 *(0.71)*	0.40 *(0.42)*	9.08 *(9.8)*	0.41	0.74 *(0.75)*	2.42 *(2.31)*	2725

smaller than 10% and are found in the bulk velocity (7.9%) and in the averaged heat flux at the walls (4.8%). The Reynolds number based on the bulk velocity is defined as $Re_b = U_b 2\delta/\nu$.

The time averaged profiles of the mixed convection case, such as mean temperature and velocity shown in 6.13a and 6.14a respectively, are non-symmetric with respect to the channel center $z = 0$. This implies that buoyancy is not zero at the center of the channel ($z = 0$). As it can be seen in figures 6.12 and 6.13a, T_{ref} is located closer to the hot wall. The velocity profiles are also non-symmetric so the wall shear stresses at walls are different as indicated in table 6.1.

The hot fluid region located at $z < -0.6$, experiences a larger velocity associated with a positive buoyancy force. Inversely, cold fluid moves slower due to negative buoyancy. The velocity fluctuations are larger near the cold wall as it can be seen in figure 6.13 while the temperature fluctuations are larger near the hot wall (see figure 6.13b).

To study the effect of numerical diffusion, simulations of the mixed convection case have been performed using the QUICK scheme [74] for the discretization of

Figure 6.14: Mean (a) and r.m.s. (b) velocity profiles

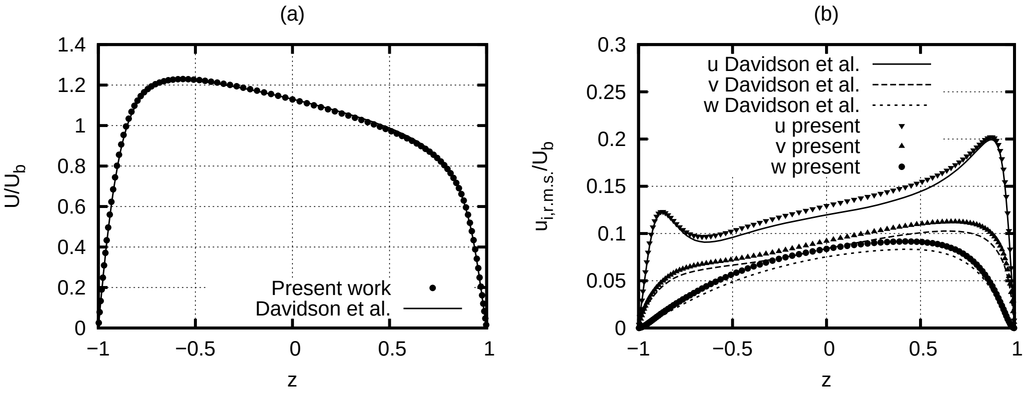

the advective terms. Results are shown in figures 6.15 and 6.16. Numerical diffusion problems are specially important on r.m.s. profiles (figure 6.15b) because unphysical additional diffusion produces the reduction of the turbulent fluctuation intensities.

Figure 6.17 shows the contribution of the different terms of the time averaged x-momentum budget (equation 3.43).

Figure 6.15: Mean (a) and r.m.s. (b) temperature profiles obtained with QUICK

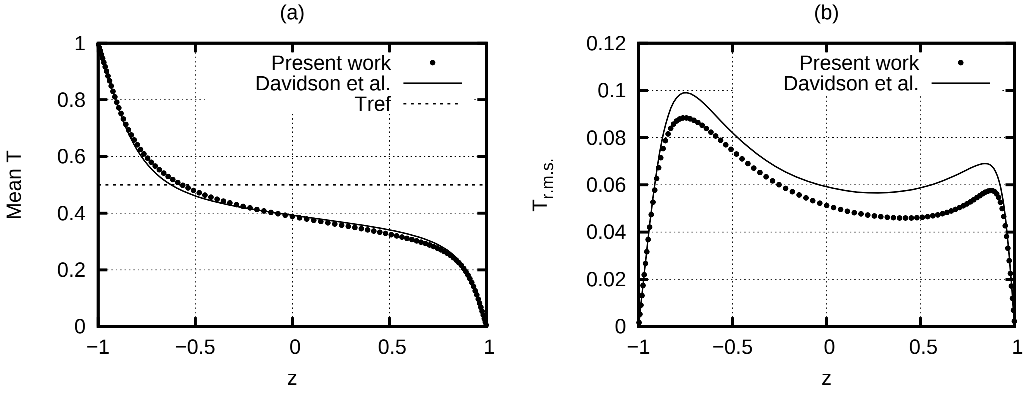

The friction at the walls is balanced by the sum of mean pressure gradient and buoyancy. Whereas the nondimensional mean wall shear stress τ_w is 1 for the non-buoyant case, this quantity for the mixed convection case needs to be reformulated

Figure 6.16: Mean (a) and r.m.s. (b) velocity profiles obtained with QUICK

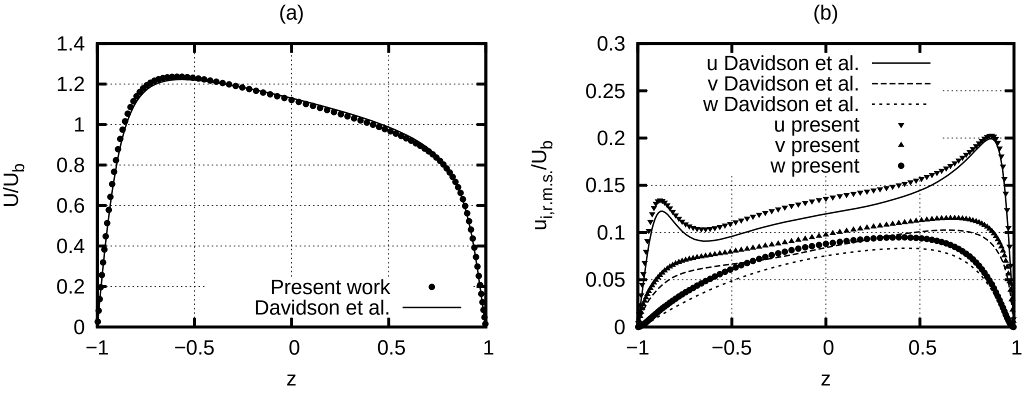

as $\tau_w = 0.5\left(\tau_{w,-\delta} + \tau_{w,\delta}\right) = \rho u_*^2 \neq 1$ because of the contribution of the buoyancy term to the x-momentum equation. Furthermore, whereas without buoyancy, the turbulent shear stress is linear in the region where viscous effects are negligible, this is not valid when buoyancy is included. For comparison, results for the developed channel flow at $Re_\tau = 150$ without buoyancy are shown in figure 6.18. The contributions of the time averaged momentum equations for this fully developed channel at $Re_\tau = 150$ and case A are the same so the numbers used to identify the different terms in figure 6.18 correspond to those used in equation 3.40.

The symmetry with respect to the centerline of the channel ($z = 0$) for the different terms in the x-momentum equation for the mixed convection case has been lost in comparison with a non-buoyant case. In order to compare both cases, figure 6.18 shows the profiles for a pressure-driven fully developed channel at Reynolds number $Re_\tau = 150$. The wall-shear stress value has decreased because the pressure gradient is balanced not only by the friction on walls but by both friction and buoyancy. This is also reflected in the decreasing of the mean viscous stress term. The mean streamwise velocity profile for case B is asymmetric. Velocity increases from the hot wall and it reaches its maximum value at $z \approx -0.65$. The maximum is reached at the centerline of the symmetric isothermal fully developed channel. Mean velocity decreases continuously from $z \approx -0.65$ to the cold wall.

The turbulent flux produced by $\overline{u'w'}$ is significantly reduced near the hot wall (6.17) in comparison with the isothermal case (6.18). It can be seen that the turbulent flux vanishes at the position where the maximum of velocity occurs.

The mean buoyancy aids the flow close to the hot wall while opposes it close the cold wall.

Figure 6.17: Mean momentum transport balance for the mixed convection case

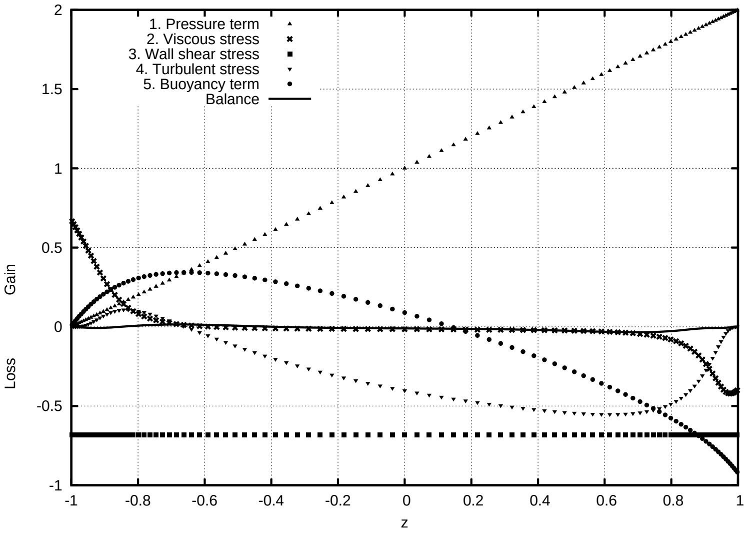

Figure 6.19 shows the contribution of the different terms of the mean temperature equation (3.44). In this case only the turbulent heat flux and the convective transport of heat have relevance. The first one becomes more important near the centerline of the channel. Inversely, the convective term is more important near the walls where the temperature gradient along the wall-normal direction is larger.

Figure 6.18: Mean momentum transport balance for isothermal fully developed channel flow at $Re_\tau = 150$

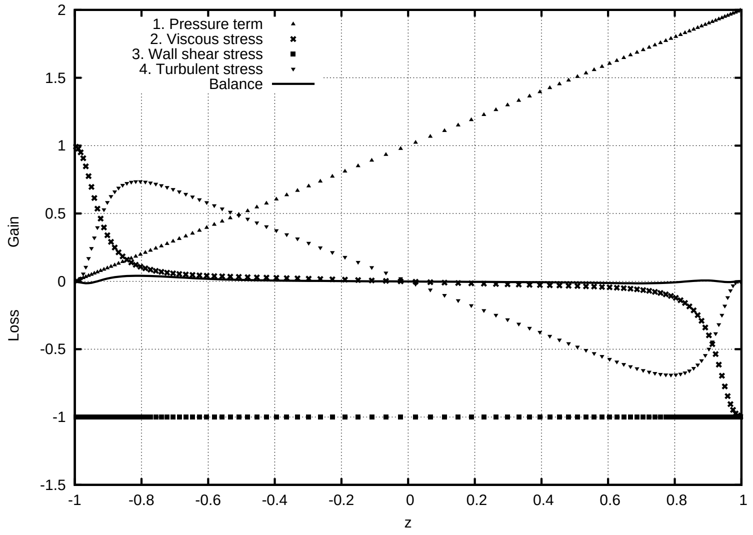

Figure 6.19: Mean heat transport balance for the mixed convection case

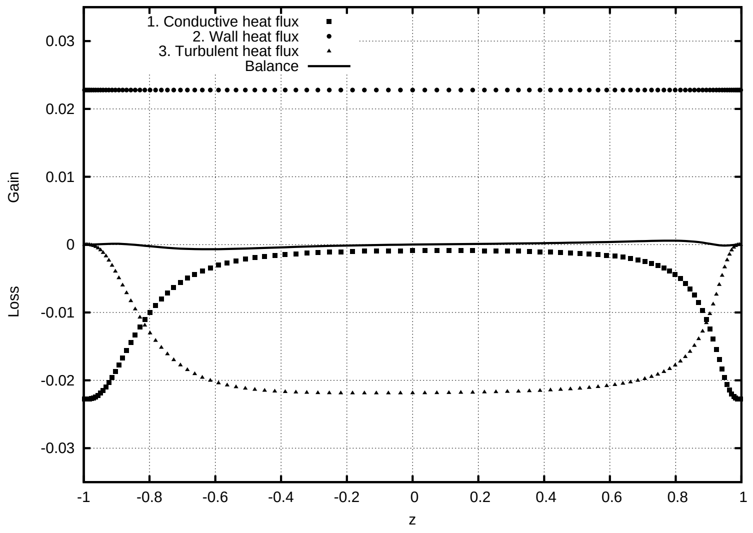

6.4 Case C: Buoyant source line in a channel at $Re_\tau = 180$ and $Gr = 10^7$

The physical model of this case is shown in figure 2.2. The grid used is the same as that in case A: $258 \times 130 \times 130$. Similarly the minimum finite volume size is $\Delta z^+_{min} = 0.2$ near the walls of the channel and the time step for time integration has been set to $\Delta t = 5 \cdot 10^{-4}$ with an averaging period of $70\delta/u_\tau$ for the calculation of the statistics.

This is the same grid resolution of the buffer zone attached at the inlet of the main domain. The buffer zone is used to generate inlet velocity and pressure fields for the computational domain of case C because the streamwise direction is not homogenous. Although this resolution may seem excessive, it allow to optimize the memory usage by assigning the same memory resources for both domains. Note that in the buffer zone, only continuity and momentum equations are solved.

Case C differs from the case A because momentum and heat are coupled through the buoyancy effect produced by the hot plume region in a colder background fluid. The lower density of the plume region forces the flow to rise as it advances along the channel. The hydrodynamic variables are no longer homogeneous along the streamwise direction and, consequently, the periodic boundary conditions are not suitable. To solve this, the buffer region shown in figure 2.2 has been attached at the inlet of the main domain. In this buffer domain, momentum equations for a developed pressure-driven channel flow are integrated and its outlet velocity field is used as the inlet boundary condition for the main domain where the buoyant plume develops.

As an example of the instantaneous temperature field figure 6.20 shows contours of temperature at different streamwise positions. The mean and r.m.s profiles for the streamwise component of the velocity vector in δ-scaled and wall coordinates are shown in figure 6.22 for three selected locations along the streamwise direction; near the inlet at $x = 6.0$, in the middle of the channel length at $x = 12.5$ and near the outlet at $x = 24.0$. The mean velocity and r.m.s. profiles for the case A (non-buoyant case) are included in figure 6.22 for comparison purposes. It is important to note that when the buoyancy is considered, symmetry is lost and different friction velocities and wall-coordinate scales are obtained for the two walls.

Table 6.2: Friction velocity and wall shear stress for case C

Wall	$\langle u_\tau \rangle$	$\langle \tau_w \rangle$
Top	1.07	1.14
Bottom	0.99	0.97

Table 6.2 shows the averaged friction velocities at the top and bottom walls. It can be seen that the wall shear stress is larger at the top wall than at the bottom wall because of the deflection of the plume towards the top wall. It can be seen in figure 6.22a that the averaged velocity profile for $z < 0$ scaled with the local friction velocity at the bottom wall agrees with the isothermal velocity profile while near the top wall ($z > 0$), where buoyancy considerably affects the flow, the profile exhibits lower values of the mean velocity. In δ-scaled coordinates it can be seen in figure 6.22b how the mean velocity decreases in the center of the channel (the maximum value has drifted towards the top wall) while it increases near the top wall.

Figure 6.20: Instantaneous temperature contours at different streamwise positions

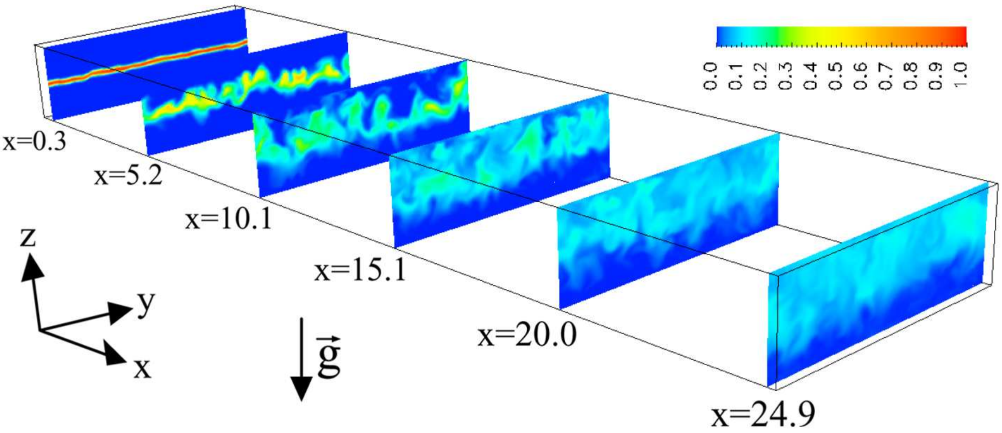

The mean wall-normal velocity component is shown in figure 6.23a. The w-component has very small values compared with its r.m.s. (figure 6.23b). In the mean field the flow is moving upwards very slowly and consequently the variation of the u-component mean profile along the channel is also small. However, it is important to note how r.m.s. values for the u-component grow near the upper wall as the streamwise position is increased as shown in figure 6.22c. Fluctuation intensities of u and w are larger in the middle of the channel ($x = 12.5$) than close to the outlet ($x = 24.0$). See for example figure 6.20. A similar tendency can be observed in the mean w component. This can be explained considering that at $x = 12.5$ the plume is moving upwards to the top wall and its development is very intense (see figure 6.20). Close to the outlet ($x = 24.0$), the plume is attached to the upper wall and the mean vertical velocity w is lower as it can be seen in figure 6.23a.

To clarify this point, the mean temperature field and the three selected positions are shown in figure 6.21. The mean temperature field identifies clearer the different stages of the buoyant plume along the channel. Close to the inlet, $x = 6.0$, buoyancy starts to deflect the plume towards the upper wall. At the middle of the channel, $x = 12.5$, buoyancy effects moves the plume upwards but it is not completely attached to the wall. Finally, at $x = 24.0$, the plume reaches the top wall and approaches to its developed regime.

Figure 6.21: Mean temperature field for case C

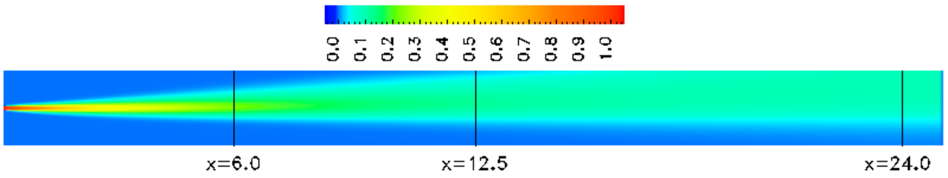

The mean temperature profiles for the selected locations are shown on figure 6.24a. The typical Gaussian bell profile associated with the mean scalar concentration (without wall effects) can be seen here for locations close to the inlet but displaced to the top wall due to the buoyancy effect.

The profiles of the temperature fluctuation intensities (see figure 6.24b) show a similar tendency with to respect the centerline. Two peaks are present even for advanced locations but symmetry with respect to $z = 0$ is not found. Compared with case A, buoyancy affects the mean temperature profile by deflecting the plume towards the upper wall while reduces the maximum intensities and increases its width. In a similar way, the two peaks in the fluctuation intensity profiles are not symmetrically distributed as they were in the case A. In the upper zone of the plume the r.m.s. values are of the same order of magnitude in case A while they decrease in the lower region. At $x = 12.5$ the behavior of the r.m.s. is similar but at $x = 24.0$ the r.m.s. values are higher in the lower part of the plume. This can be explained by the damping effect of the wall on the turbulence intensity.

Figure 6.22: Mean (a) and r.m.s. (b) u-component profiles

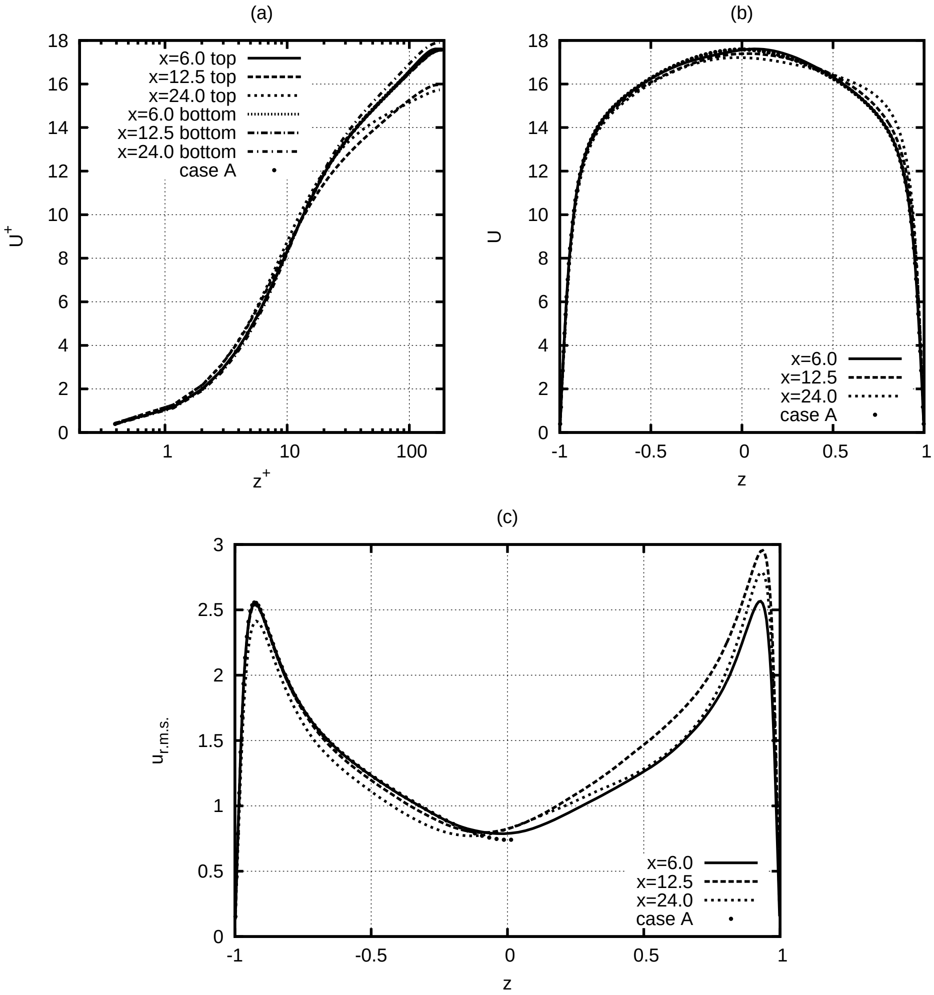

The figures 6.25 to 6.33 show the profiles of the different terms of the time averaged x-momentum, z-momentum and heat transport equations 3.45, 3.46 and 3.47 respectively. Figures 6.25, 6.26 and 6.27 show the terms of the x-momentum equation at the streamwise positions $x = 6.0$, $x = 12.5$ and $x = 24.0$ respectively. The number in the labels of these figures identifies the different terms of equation

Figure 6.23: Mean (a) and r.m.s. (b) w-component profiles

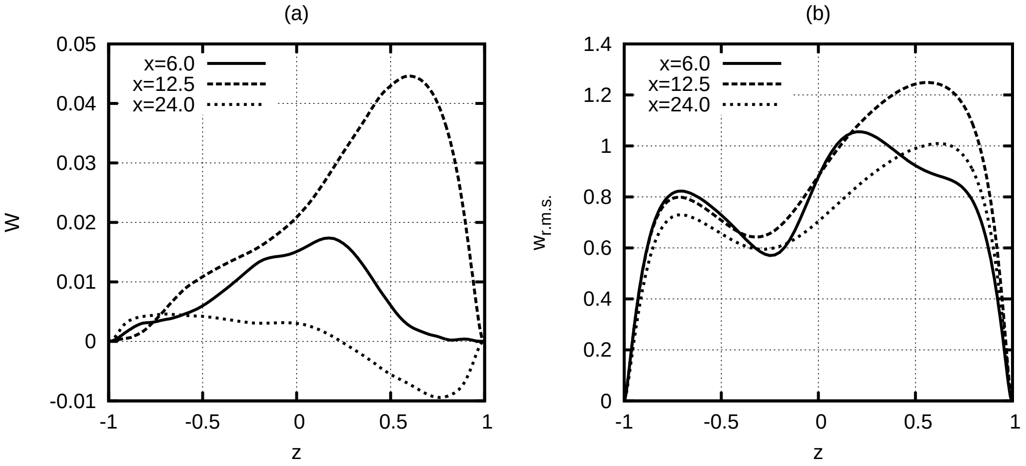

3.45

Unlike cases A and B, the momentum and heat transport equations of case C are not homogeneous along the streamwise direction and the integration along the wall-normal direction is not possible. Consequently, profiles correspond to the different terms of equations 3.45 to 3.47.

Near the inlet, at $x = 6.0$ (figure 6.25), the pressure gradient is balanced mainly by the streamwise convection and the wall-normal turbulent terms in the central region of the flow. Near the walls, the wall-normal diffusion contributes to balance the wall-normal turbulent transport and the pressure gradient.

At $x = 12.5$ (figure 6.26), the situation is similar to that corresponding to $x = 6.0$. However, the two main contributions, the wall-normal diffusion and the wall-normal turbulent flux, increased in magnitude close to the top wall. Furthermore, in the upper region both the contributions of the convective terms in the streamwise and wall-normal directions are increased because of the plume defection. As it was seen for the mean velocity and r.m.s. profiles, at this position the plume development is very intense. The mean streamwise velocity component is slightly larger close to the top wall and the vertical mean velocity component exhibit a small positive value.

At $x = 24.0$ (figure 6.27), the plume has already reached the upper wall and the contribution of the convective terms decrease but they have still significative values. The two main contributions (the wall-normal diffusion and the wall-normal

Figure 6.24: Mean (a) and r.m.s. (b) temperature profiles

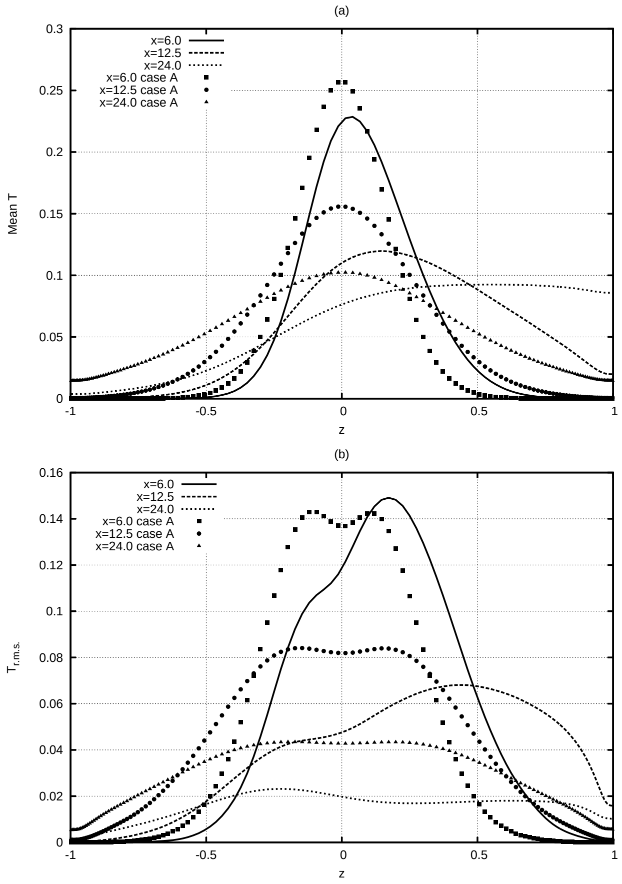

turbulent flux) profiles are similar to those found at $x = 6.0$ but their magnitude has increased near the top wall and decreased slightly near the bottom one.

Figures 6.28, 6.29 and 6.30 show the contribution of the terms of the time averaged z-momentum equation. The number in the labels of these figures identifies the different terms of equation 3.46.

The main terms in the budget are the pressure gradient, the wall-normal turbulent flux and the buoyancy. The convective and diffusive terms in the normal and streamwise directions are insignificant compared with the previous contributions. It is important to remember that the mean positive value of w is relatively small.

It should be noted that the buoyancy term is proportional to the mean temperature profile. The plume drifts towards the top wall as the position in the streamwise direction is increased and the buoyancy term profile maximum moves upwards ac-

Figure 6.25: Mean x-momentum transport balance at x=6.0

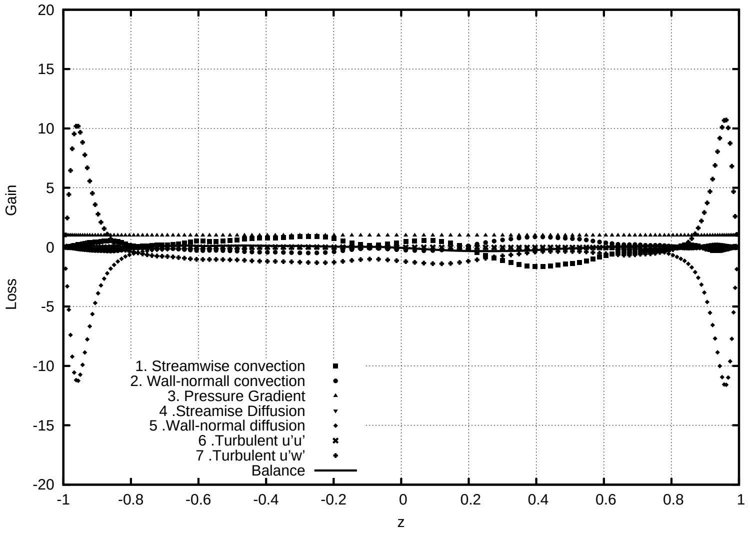

cording to this. At $x = 6.0$ the plume deflection is not important and the buoyancy term has a maximum close to the center of the channel ($z = 0$) while its value close to the walls is insignificant. In the central region of the channel the pressure gradient is the main contribution balancing the buoyancy and, close to the walls, it balances the wall-normal turbulent contribution. For locations farther from the wall the wall-normal turbulent profile in the center of the channel become smoother in comparison with $x = 6.0$. The maximum value for the buoyancy, according to the mean temperature profile, has shifted upwards reaching the wall at $x = 12.5$. The pressure gradient term is antisymmetric respect to the buoyancy term because the wall-normal turbulent contribution is small compared with the other two in the central region of the channel. Close to the source, at $x = 24.0$, the plume is already attached to the top wall. The wall-normal turbulent term profile is very smooth and is significant only close to the walls. The buoyancy contribution, proportional to the mean temperature, is always zero near the bottom wall.

Figures 6.31 to 6.33 show the contribution of the different terms of the time averaged heat equation.

The contributions of the mean terms to the heat equation near the inlet are similar to those corresponding to the case A but deflected towards the top wall. The most important contributions are the streamwise convective and the wall-normal

Figure 6.26: Mean x-momentum transport balance at x=12.5

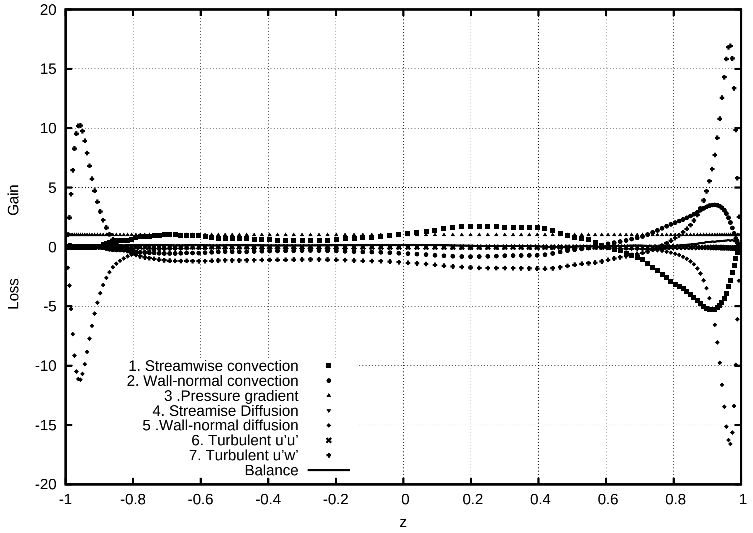

turbulent heat flux.

Close to the source, at $x = 6.0$, the two main contributions profiles are very similar to those found in the case A (non-buoyant) in the central region of the channel. However, their magnitude increases close to the top wall and decreases close to the bottom one. This can be explained because of the plume deflection and the increase of the mean streamwise velocity near the top wall. The turbulent flux contribution in the upper zone of the channel has to be larger than that at the lower one since this quantity is zero at walls and its gradient in the wall-normal direction have to be larger in the upper zone. There is a small contribution of the wall-normal diffusion term specially significant in the central region of the channel. Once the plume reaches the top wall, at approximately $x = 12.5$, the absolute magnitude of the streamwise convective and the wall-normal turbulent flux terms in the region close to the top wall are as large as in the center of the channel. As it is observed in the non-buoyant case, the wall-normal diffusive term become significant near the top wall. The plume never reaches the bottom wall, so this term is not significant there. It is important to note that the position at which the buoyant plume reaches the top wall is smaller than that for the non-buoyant case. Close to the outlet, the wall-normal conductive contribution becomes more important and the wall-normal convective term become significant as well.

Figure 6.27: Mean x-momentum transport balance at x=24.0

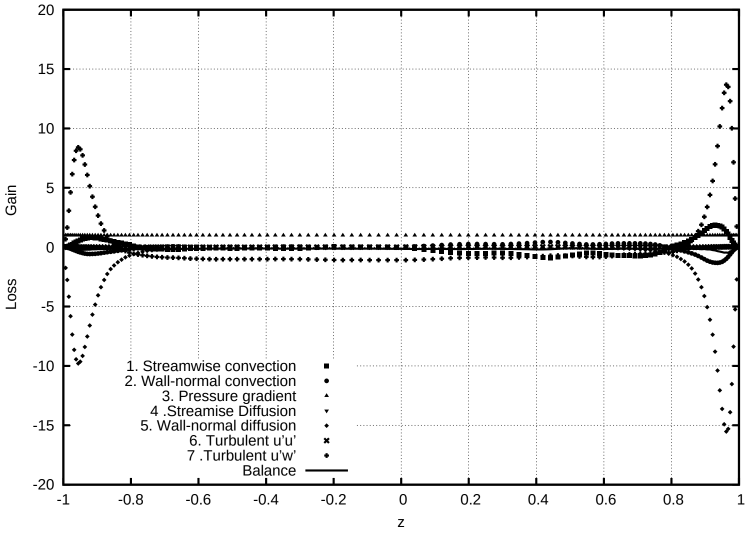

Due to the buoyancy forces acting in the wall-normal direction, case C is the only case considered with a non-fully developed dynamic field. Along the streamwise direction the pressure forces resulting from the mean pressure gradient are balanced by friction at walls. For case C, the term corresponding to the non-developed mean pressure gradient along the streamwise direction may be different from zero because of the development of the plume (see term 3 in the equation 3.45 for a decomposition of the mean pressure gradient into a developed and a non-developed contributions). The values for this term are less than 7% of the mean pressure gradient. Therefore this evolution has to be reflected on the quantities related with the friction on walls. Figure 6.34 shows the profiles of the local friction velocity on both walls along the streamwise direction.

When the plume reaches the top wall at $x \approx 16$, the shear stress and consequently its friction velocity, increase. The position for the maximum in this profile points out the location where the plume experiences the most intense evolution. After attaching the wall, the flow decelerates and the friction velocity decreases. On the other hand, on the lower wall the shear stress and the friction velocity decrease slightly. It can be seen that the size of the domain along the streamwise direction is not long enough for the flow to reach the fully developed state. At this stage, both shear stresses at the two walls would be constant and their mean would permit

Figure 6.28: Mean z-momentum transport balance at x=6.0

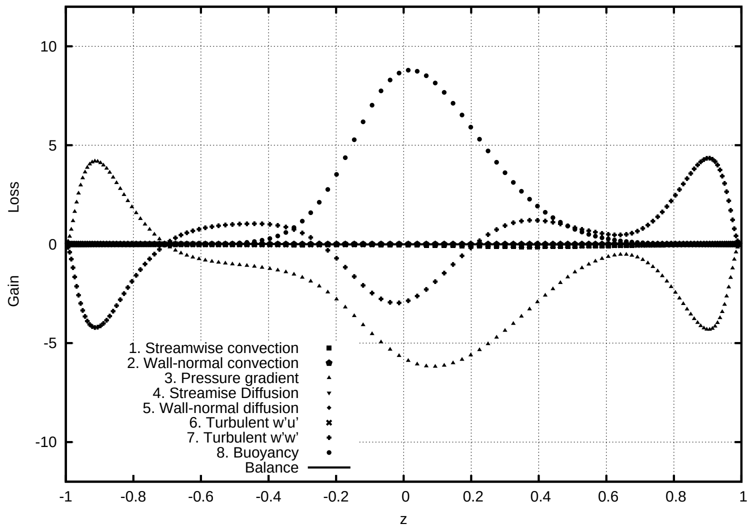

to obtain the corresponding friction velocity value that would balance the constant mean pressure gradient. That friction velocity can be expressed as:

$$u_\tau^* = \sqrt{\frac{1}{2Re_\tau}\left(\left.\frac{\partial U^*}{\partial z^*}\right|_b + \left.\frac{\partial U^*}{\partial z^*}\right|_t\right)} \tag{6.3}$$

where subscripts *b* and *t* stand for *bottom* and *top* walls.

Figure 6.29: Mean z-momentum transport balance at x=12.5

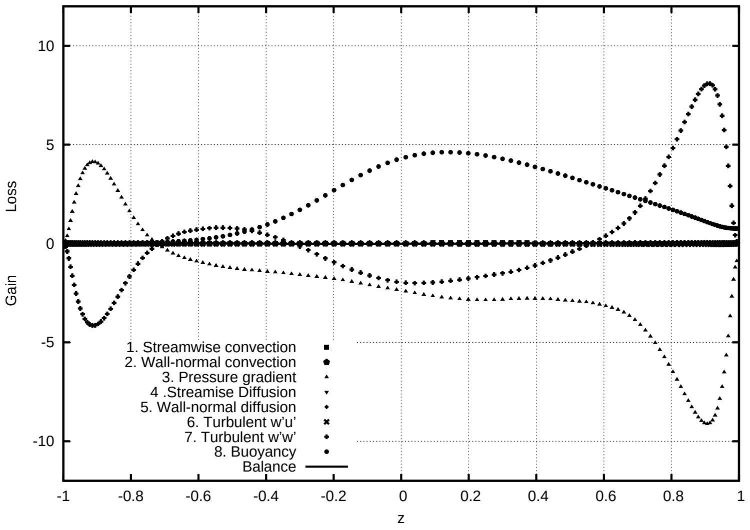

Figure 6.30: Mean z-momentum transport balance at x=24.0

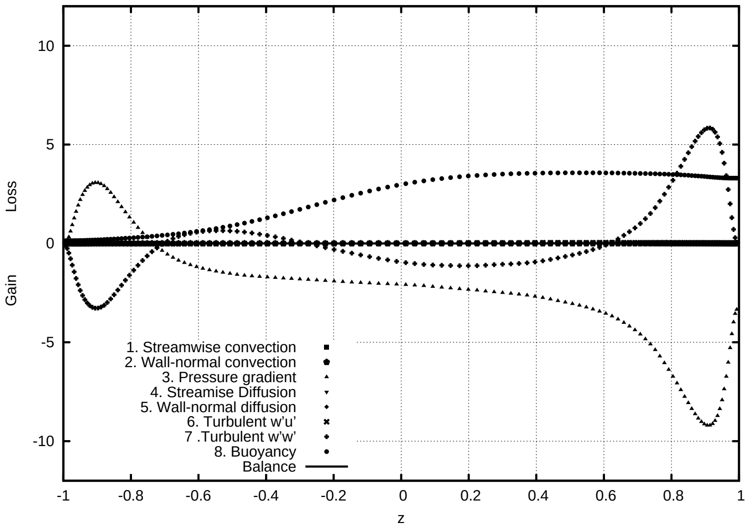

Figure 6.31: Mean heat transport balance at x=6.0

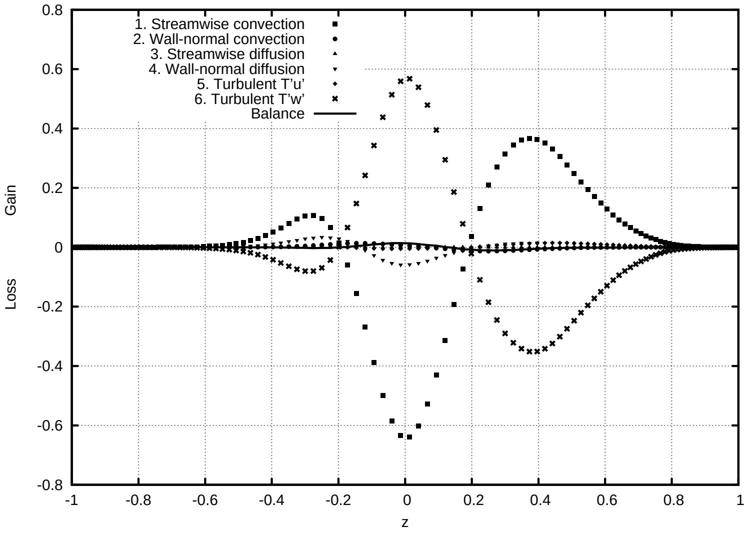

Figure 6.32: Mean heat transport balance at x=12.5

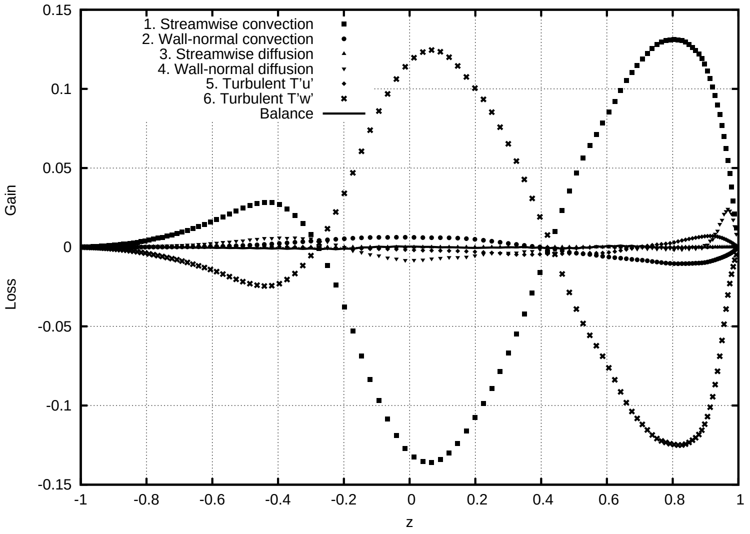

Figure 6.33: Mean heat transport balance at x=24.0

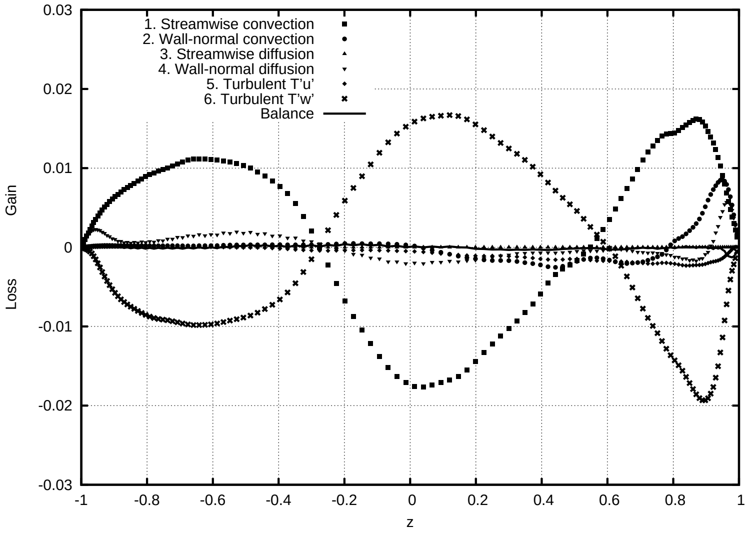

Figure 6.34: Profile of u_τ on both walls

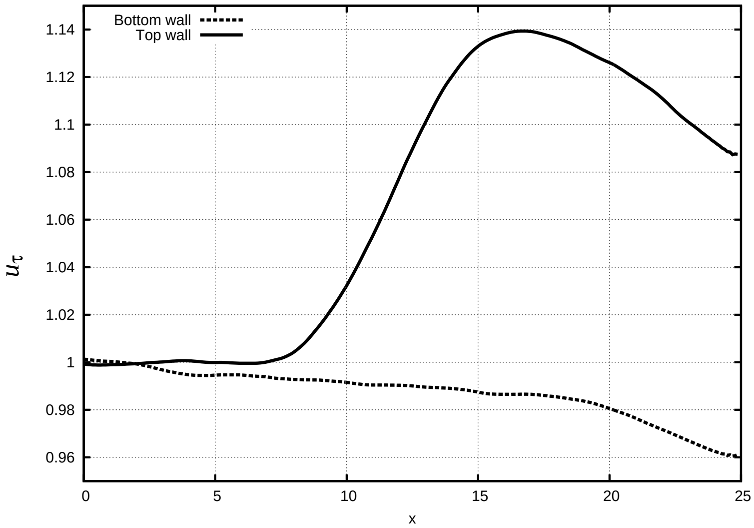

Chapter 7

Preliminary results of a turbulent reacting flow

The configuration presented in case A was used to study the turbulent dispersion in a channel where a reactive is released through the line source within a background flow carrying another reactive. Both species react to produce the product P following a second order reaction ($A+B \longrightarrow P$). Such reaction is assumed to occur under isothermal conditions (the heat of reaction is zero) so there are no buoyancy forces. The concentration at the inlet (the source line) for the reactant A is set to $C_A(0,y,\pm H_S,t) = 1 \;\; \forall\, z \in [-H_S, H_S]$ and $C_A(0,y,z,t) = 0 \;\; \forall\, z \ni [-H_S, H_S]$ with $H_S = 0.054\delta$. The concentration of B in the background flow is $C_B(0,y,z,t) = 0.05$ while the product P concentration at the inlet is zero $C_P(0,y,z,t) = 0$. Reactants enter the channel premixed so the chemical reaction takes place from the inlet of the channel.

The grid resolution used in this case is the same that was used for case A.

The concentration fields have been initialized with a constant background concentration of $C_B(x,y,z,0) = 0.05$ and $C_A(x,y,z,0) = C_P(x,y,z,0) = 0$. When the reactive plume is developed, the sampling procedure to compute the flow statistics has been started. The time-averaged quantities have been obtained with a sampling period of $23\delta/u_\tau$ and consequently the mean results shown in this section have not completely converged.

The time averaged equation 1.21 for a second-order chemical reactive system can be written as:

$$\frac{\partial\overline{C_\alpha}}{\partial t}+U_j\frac{\partial\overline{C_\alpha}}{\partial x_j}=\frac{1}{Re_\tau Sc}\frac{\partial^2\overline{C_\alpha}}{\partial x_j\partial x_j}-\frac{\partial\overline{C'_\alpha u'_j}}{\partial x_j}\pm Da\left(\overline{C_A C_B}+\overline{C'_A C'_B}\right) \tag{7.1}$$

The symbol α denotes any of the species involved in the chemical reaction. A and B are the reactants so the sign of the last term on the right hand side of the equation 7.1 which is the reaction term, is negative so that species are being consumed. When α refers to the product P, the sign of this term is positive, so P is generated. The Schmidt number is $Sc = 1$ for all the species. The reaction term is constituted by the mean reaction rate $Da\overline{C_A C_B}$ and the turbulent contribution $Da\overline{C'_A C'_B}$. This turbulent contribution appears for orders of reaction larger than 1.

The Damkhöler number has been set to 1 so the turbulent and the reactive temporal scales are of the same order. When the Damkhöler number is small, the reaction rate is slow compared to the large scale processes of turbulent mixing and the system can be considered premixed. In this case the reaction takes place distributed over the whole domain and reaction rates are determined purely by the chemical kinetics. On the other hand, when the Damkhöler number is large, even with respect to the Kolmogorov time scale of the flow, the reaction occurs instantaneously as soon as the reactants meet each other at the molecular scale. When the reactants are introduced segregated, the reaction usually occurs in form of thin reacting sheets, which form the interface between regions of reactants. These sheets are moved around and strained by the turbulent flow. The rate of reaction is, in this case, determined by the amount of mixing at the molecular scale and for this reason it is said that the reaction is diffusion limited. Intermediate values of the Damkhöler number produce reaction rates determined both by the turbulent mixing and by the chemical kinetics.

Figures 7.1, 7.2 and 7.3 show contours of the averaged concentration fields for the three species involved in the reaction. The color scales have been chosen to enhance the details of the concentration interfaces. As it can be seen, the reactant B or the product P mean concentration fields (see figure 7.2 and 7.3 respectively), reaction takes place from the channel inlet because reactants enter the domain premixed. The values of the chemical conversion, defined in equation 7.2, at the channel outlet are around 10%.

$$X(\%)=\frac{\overline{F_A}\big|_{x=0}-\overline{F_A}\big|_{x=Lx}}{\overline{F_A}\big|_{x=0}}\times 100 \tag{7.2}$$

where $\overline{F_\alpha}$ is the time averaged mass flow defined as:

$$\overline{F_\alpha} = \frac{1}{2\delta}\int_{-\delta}^{\delta} \overline{C_\alpha} U dz \tag{7.3}$$

Figure 7.1: Mean reactant A concentration field

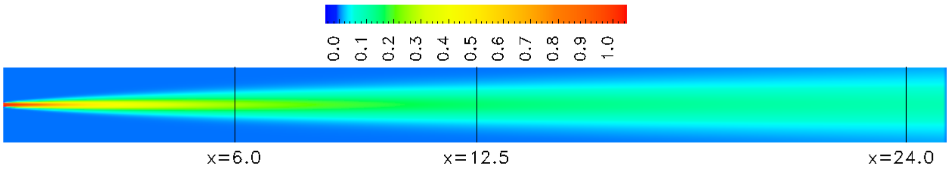

Figure 7.2: Mean reactant B concentration field

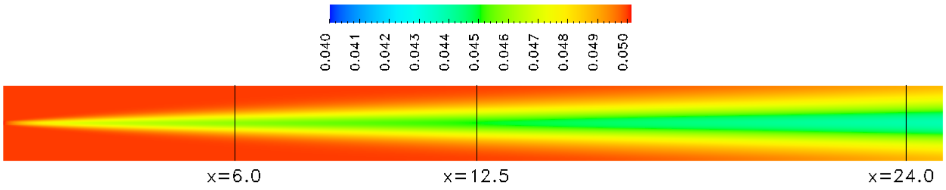

The relevant terms of the averaged momentum transport equation are the same as those presented in equation 3.40 for the case A in section 3. Although periodic boundary conditions for the streamwise direction are the obvious choice for the momentum quantities, the buffer region at the inlet of the computational domain was kept to check that non-reflecting boundary conditions applied over the momentum equations have no effect on the results. The balance of the x-momentum equation is shown in figure 7.4. The numbers used to identify the different contributions correspond to those used in equation 3.40.

The relevant terms of the mean concentration transport equation 7.1 can be written as:

Figure 7.3: Mean product P concentration field

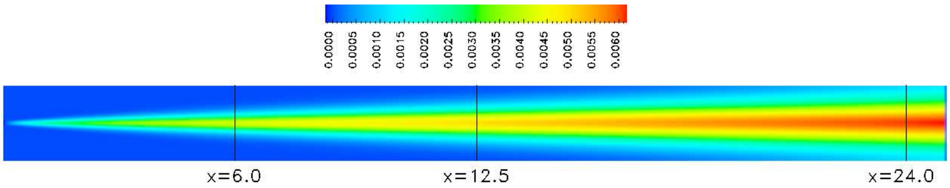

Figure 7.4: Mean momentum transport balance (reactive case)

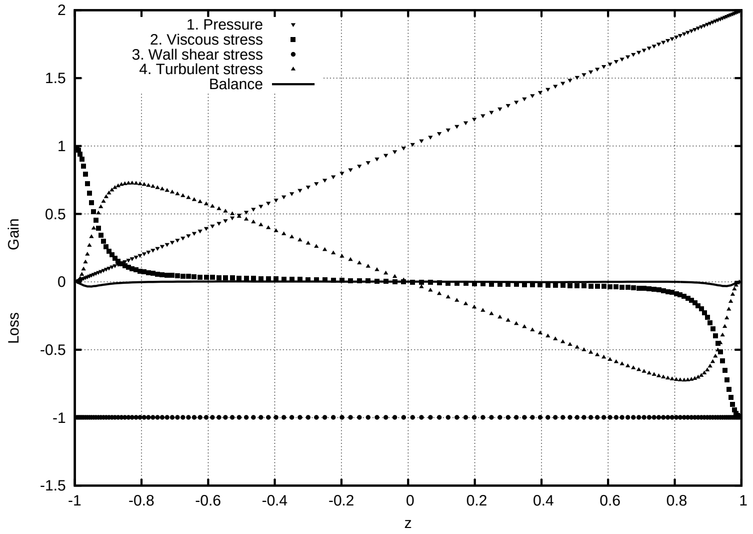

$$0 = \underbrace{-U\frac{\partial \overline{C_\alpha}}{\partial x}}_{1} + \underbrace{\frac{1}{Re_\tau Sc}\frac{\partial^2 \overline{C_\alpha}}{\partial x^2}}_{2} + \underbrace{\frac{1}{Re_\tau Sc}\frac{\partial^2 \overline{C_\alpha}}{\partial z^2}}_{3} - \underbrace{\frac{\partial}{\partial x}\left(\overline{C'_\alpha u'}\right)}_{4} - \underbrace{\frac{\partial}{\partial z}\left(\overline{C'_\alpha w'}\right)}_{5} \underbrace{\pm Da\left(\overline{C_A}\,\overline{C_B} + \overline{C'_A C'_B}\right)}_{6} \qquad (7.4)$$

The contribution of the different terms of the equation 7.4 for reactant A is shown in figure 7.5 at three selected streamwise positions. These profiles are very similar to those presented for the scalar concentration for case A. The reaction term is much smaller than the terms corresponding to the streamwise convection, the wall-normal turbulent flux and the wall-normal diffusion. The reaction advances as one moves downstream along the channel but, even at $x = 24.0$, the reaction term represents only a very small contribution to the budget of reactive A. It is obvious that at larger Damkhöler numbers this term would be larger but the problem would be more difficult to solve because the smaller time scales for the reactive transport equations would demand time-splitting schemes to capture the *fast* chemical reaction.

The time averaged balance for reactant B is shown in figure 7.6. In this case the reaction term become the most important contribution to the mean transport equation. The small magnitude of the value of the relevant terms make clear the need for larger averaging time, specially at downstream positions. In spite of this, the time averaged overall mass balance is fairly well satisfied.

Finally, the balance for the product P is shown in figure 7.7. As it happened for reactive B, the reaction term is the most important but the magnitude of the values of the relevant terms are small. As it was expected, the results for the mean relevant terms of equation 7.4 for the reactant B and product P are relative similar but antisymmetric with respect to $z = 0$. In the reacting plume, the product P is being generated at the same rate as reactant B is being consumed by the chemical reaction. This imply that the gradients have opposite signs so the convective and turbulent terms are antisymmetric. The same happens with the second derivative for the diffusive term and obviously for the reactive term as well.

Figure 7.5: Mean reactant A transport balance at x=6.0, x=12.5 and x=24.0

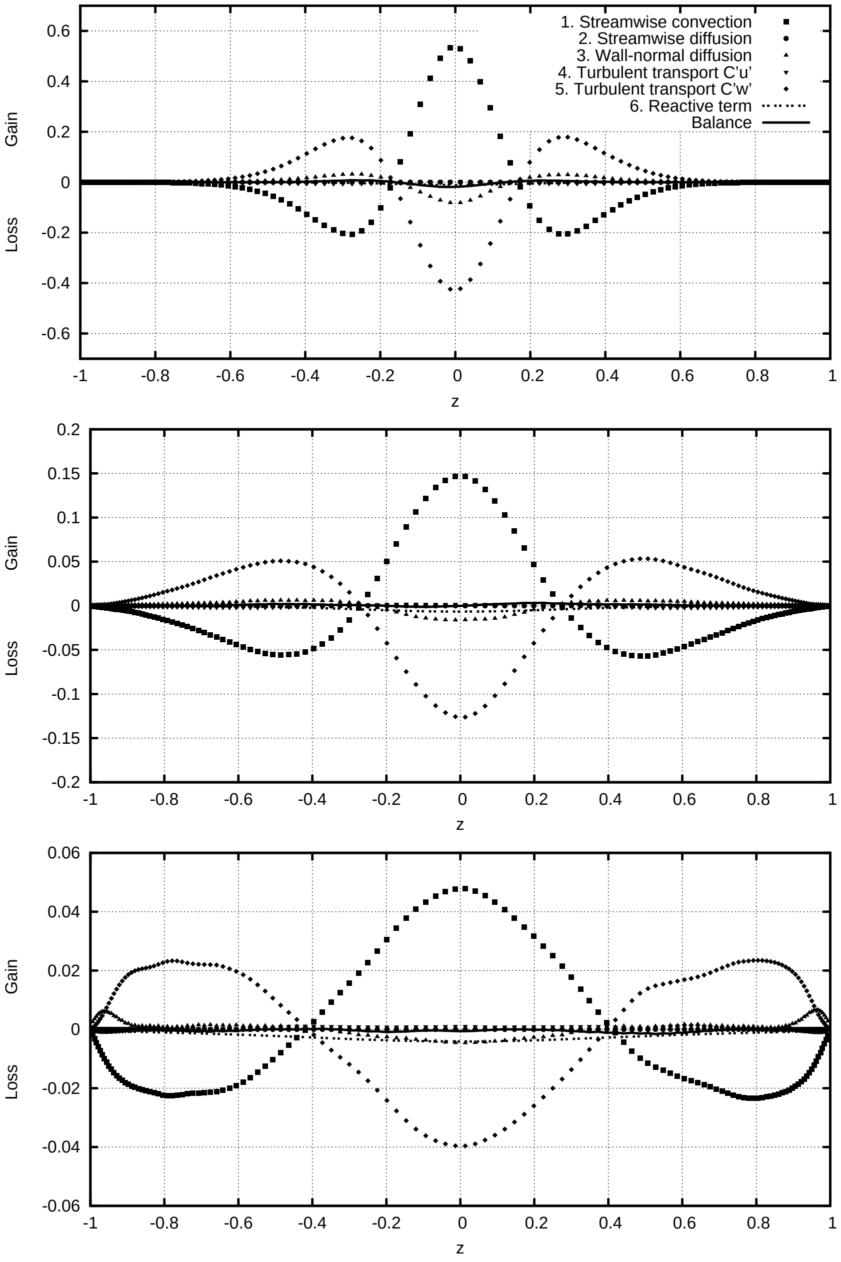

Figure 7.6: Mean reactant B transport balance at x=6.0, x=12.5 and x=24.0

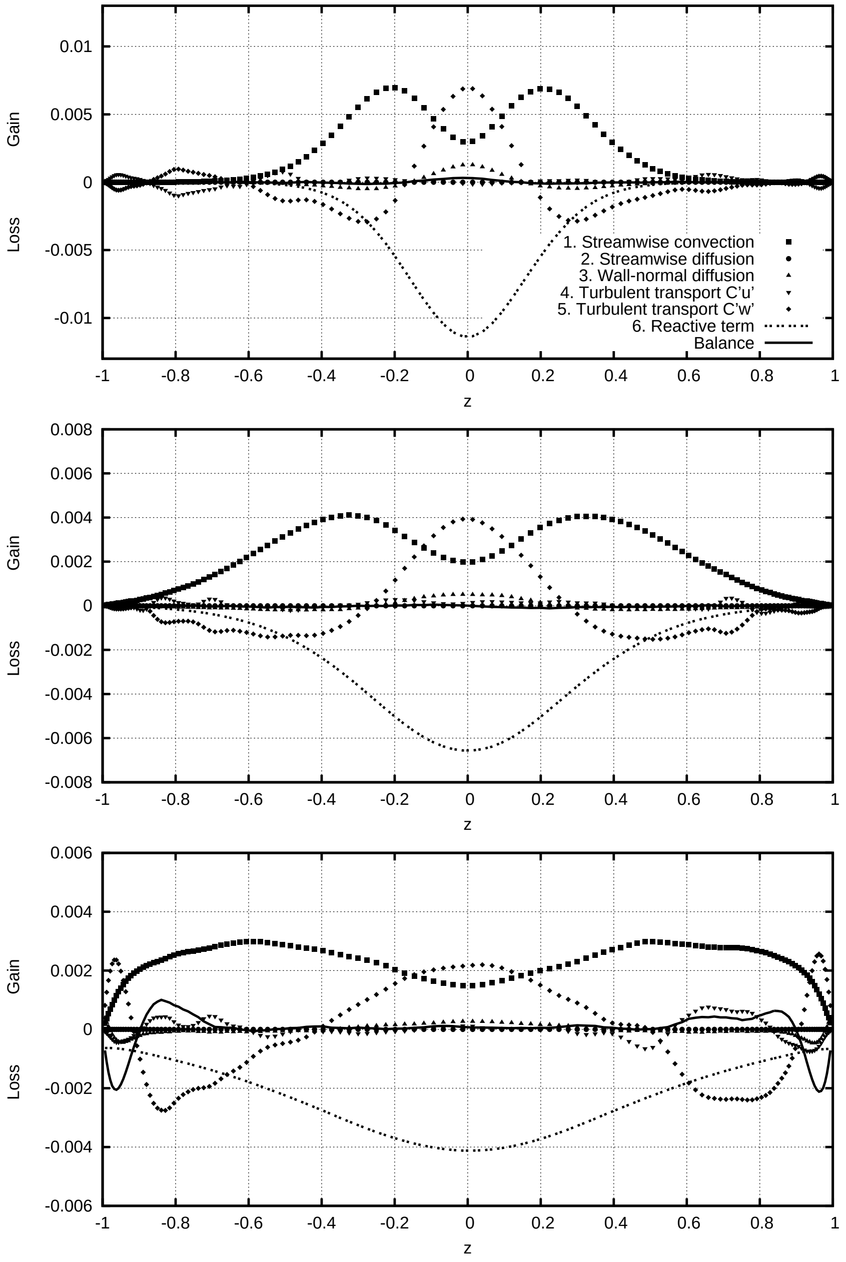

Figure 7.7: Mean product P transport balance at x=6.0, x=12.5 and x=24.0

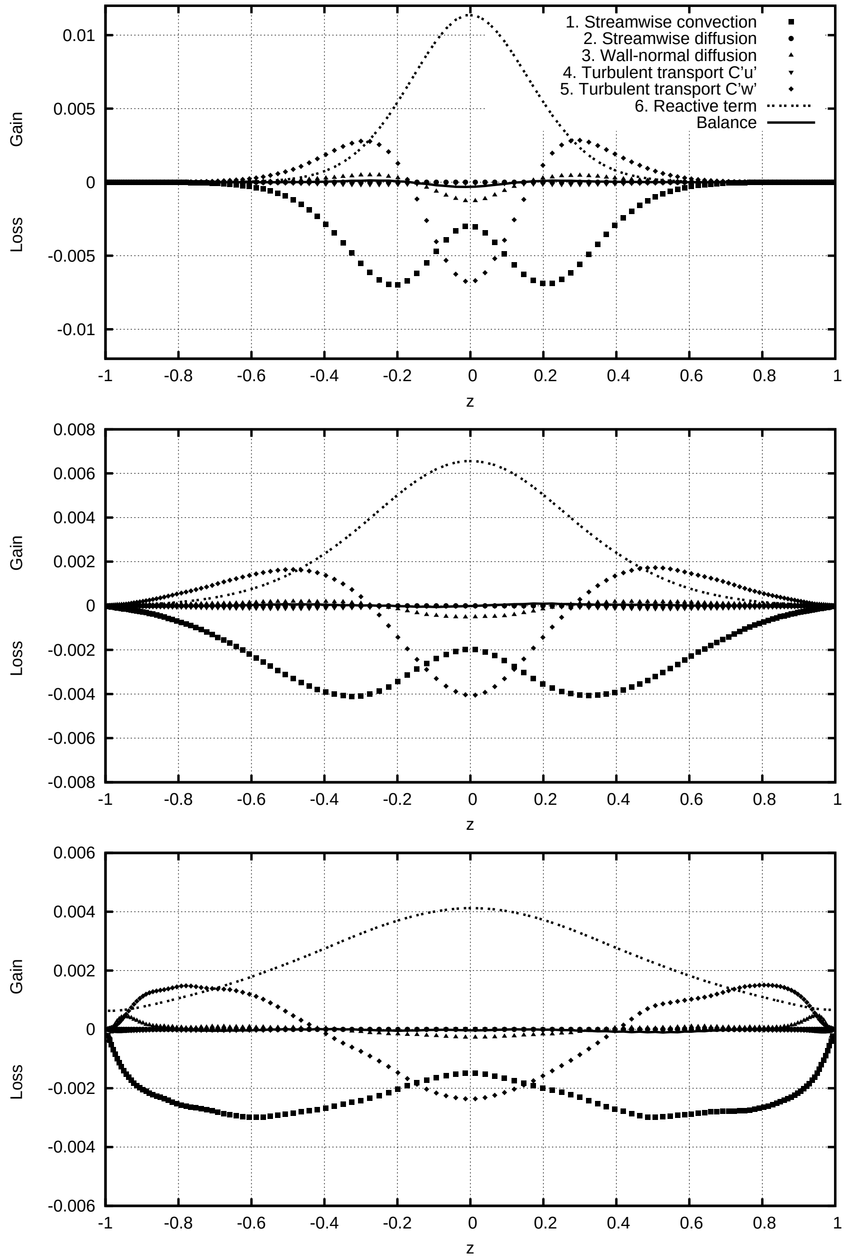

Chapter 8

Conclusions

8.1 Multigrid techniques

Multigrid has demonstrated to be the best option for solving Poisson type equations. This solver consumed CPU times one order of magnitude smaller than the conjugate gradient methods for all the cases studied. The cases considered included two synthetic cases with Dirichlet and Neumann boundary conditions with uniform and non-uniform grids and the pressure calculation case for a fully developed channel flow.

On the other hand, the scalability of multigrid is lower than that corresponding to conjugate gradient methods. The reason lies in the large communication requirements, specially at the beggining of the Full-Multigrid Algorithm where adequate initial solutions have to be found to initialize the smoother (SOR) step in each grid level. Using 8 processes, the typical value of *speed-up* for any of the synthetic cases for multigrid is between 2 and 3 while it ranges between 4 and 6 for conjugate gradient methods. For uniform grids the CG method requires smaller CPU times than Bi-CGSTAB although the *speed-up* is better than that for CG. For non-uniform grids the situation is opposite. The Bi-CGSTAB, more suitable for non-symmetric matrices, is between 1.1 and 1.7 times faster than CG although, in terms of *speed-up*, the CG exhibit better performance. Scalability differences between CG and Bi-CGSTAB were observed to be small for Neumann boundary conditions and for uniform and non-uniform grids while they were significant for Dirichlet boundary conditions.

For the pressure calculation of the turbulent flow in a fully developed channel, the CPU times for all three solvers were larger in comparison with the synthetic cases because the channel grid resolution is double than that used in the synthetic cases ($258 \times 130 \times 130$ and $130 \times 130 \times 130$ grid points respectively). Furthermore, the source terms for the synthetic cases and the fully-developed channel flow are very different in terms of complexity. In fact, for the last one, the source term of the Poisson equation shows a large range of scales because it is associated with a turbulent velocity field. In contrast, the source term of the synthetic cases is very smooth.

For instance, the CPU time in arbitrary units for the synthetic case with Neumann boundary conditions and a non-uniform grid with a stretching factor of $r = 1.01$ (which is the most similar to the pressure calculation in term of boundary conditions type and grid stretching) using 8 processes is 1 for CG and 0.5 for Bi-CGSTAB. For the pressure calculation in the fully developed channel flow, the CPU times in the same arbitrary units are approximately 1.5 for Bi-CGSTAB and 8.0 for CG. For multigrid, the synthetic case takes 0.04 time units and for the pressure calculation in the developed channel flow takes 0.4 time units.

8.2 Channel flow configurations

To check the accuracy of the computational code, the mean velocity, fluctuation intensities and friction coefficients of a fully developed channel flow at $Re_\tau = 150$ have been compared successfully with existing data.

Results of the fully developed channel flow at $Re_\tau = 180$ with a scalar source line vertically centered at the inlet of the channel also showed good agreement with DNS and experiments avaliable in the literature. The temperature r.m.s. profiles showed the two peaks associated with the inhomogeneity created by the walls of the channel flow at downstream positions away from the source line. The TVD discretization of the non-linear advective terms avoids the non-physical scalar concentration values associated with the sharp scalar gradients regions close the source.

The budget for the time averaged heat transport equation shows the contributions of the different relevant terms as the plume disperses. Close to the source the main terms are the streamwise convection and the diffusive and turbulent flux in the wall-normal direction. The diffusion and turbulent transport in the streamwise direction have no significant contributions. At this location, the profiles for the three main contributions are zero at $z = \pm 0.17\delta$ where $z = 0$ is the center of the channel and δ is the channel half width. These positions are where the gradient of the mean temperature with respect to the streamwise direction is zero and the position of the inflection point of the mean temperature profile in the wall-normal direction. This location approaches to the wall at larger streamwise positions. The magnitude of the contributions decreases as the position in the streamwise direction increases and the plume disperses. When the plume reaches the walls the wall-normal molecular diffusion shows significant values close to them.

The simulation of the mixed convection flow at $Re_\tau = 150$ and $Gr = 9.6 \cdot 10^5$ showed low-frequency fluctuations in the mean temperature and bulk velocity and required a large channel length ($8\pi\delta$) and a large sampling time period to converge the statistic quantities. The numerical diffusion associated with the *upwind* methods has been quantified comparing the QUICK and the central discretization scheme for the non-linear advective terms. It has been shown the damping of the fluctuation intensities and the consequent lower values for the r.m.s. profiles when using QUICK. The results of this simulation showed also good agreement with previous DNS data.

The aiding and opposing effects of the buoyancy on the flow driven mainly by a mean pressure gradient produce an increase of velocities and a decrease of the fluctuation intensities close to the hot wall. Oppositely, close to the cold wall, velocities are decreased and r.m.s. increased. The reference temperature, defined as the average between the temperatures of the walls (fluid a T_{ref} experiences no buoyancy), lies closer to the hot wall.

The budgets of the time averaged x-momentum and heat transport equations show that the turbulent transport in the direction normal to the wall has large values near the cold wall but is decreased near the hot one. Oppositely, the viscous stresses are larger near the hot wall and are decreased near the cold one.

The simulation of a buoyant plume required a buffer region to provide adequate boundary conditions. This increased the computational requirements significantly. The buoyancy forces drifted the temperature plume towards the top wall. This deflection produces positive values of the time averaged vertical velocity component which are small in comparison with its fluctuation intensity. The mean velocity profiles of the streamwise velocity component near the bottom wall collapsed on the universal profile using the wall scaling. However the profiles close to the top wall show smaller values of the streamwise velocity component in the central region of the channel. The fluctuation intensities of the streamwise velocity component are increased near the top wall and slightly decreased near the bottom one. The evolution of the mean velocity profiles at different positions in the streamwise direction show that at $x = 12.5\,\delta$ the plume evolves faster than close to the outlet and its development is more intense. In fact, the plume reaches the top wall near this position where the local friction velocity on the top wall has a maximum. On the other hand, the local friction velocity of the bottom wall decreases monotonically as the streamwise position is increased. The value of the mean pressure fluctuation gradient arising from the developing conditions of the flow is less than 7% of the mean pressure gradient. Its contribution to the mean x-momentum balance is small compared with other terms.

The mean temperature profiles at different streamwise positions show maxima near the top wall as the plume is deflected upwards The maximum value of the mean temperature profile is decreased as the position along the streamwise direction is increased and the width of the profile (associated with the plume vertical dispersion) is increased. This can be explained considering the vertical movement imposed by the plume deflection. The vertical plume dispersion is produced by the advective and diffusive transport mechanisms and it is enhanced in comparison with the non-buoyant case by the buoyancy effect. The r.m.s. profiles for temperature for the non-buoyant case showed two peaks symmetrically located around $z = 0$. In the buoyant case this symmetry does not exist and the intensity of fluctuations is decreased at locations far from the source. Near the source, the upper peak which is located close to the top wall is larger than that corresponding to the non-buoyant case.

The budget for the time averaged x-momentum transport equation shows that the wall-normal viscous and turbulent flux terms are the main contributions. Near the position where the plume reaches the top wall and evolves faster, the wall-normal and streamwise convective terms become significant contributions near the top wall but they are decreased near the channel outlet when the plume is already attached to the wall. Close to the inlet, the wall-normal viscous and turbulent flux terms have similar values for both regions close to the walls but farther they decrease close to the bottom wall and they increase close to the top one.

The relatively small positive value of the mean vertical velocity component explains the small contributions of the wall-normal convective and diffusive terms to the budget of the mean z-momentum transport equations. The buoyancy contribution, proportional to the mean temperature, is important and its maximum moves upwards as the position in the streamwise direction is increased. This term is always zero near the bottom wall because of the plume deflection towards the top wall. The pressure gradient evolves along the streamwise direction balancing the contribution of the buoyancy together with the wall-normal turbulent term.

The profiles for the mean heat transport equation contributions are similar to those at the non-buoyant case. Close to the source, the two main contributions, the streamwise convective term and the wall-normal turbulent flux, are very similar to those found in the non-buoyant case in the central region of the channel. The turbulent flux term in the upper zone of the channel close to the top wall is larger than that of the lower one since this quantity is zero at walls and its gradient in the wall-normal direction has to be larger in the upper zone. There is a small contribution of the wall-normal diffusion term specially significant in the central region of the channel. Once the plume reaches the top wall, the magnitude of the streamwise convective and the wall-normal turbulent flux terms in the region close to the top wall are as large as in the center of the channel. As it is observed in the non-buoyant case, the wall-normal diffusive term becomes significant near the top wall. The plume does not reach the bottom wall, and consequently this term in not important in this region. Close to the outlet, the wall-normal conductive contribution becomes more important and the wall-normal convective term becomes significant as well.

Preliminary results of a turbulent reactive flow in a fully developed channel have been also reported. The contributions of the different terms of the time averaged budget of the concentration of the chemical species show that for the most concentrated reactive (introduced through the line source) the reaction term is not important in comparison with the streamwise convection, the wall-normal turbulent term and the wall-normal diffusion. The molecular diffusion term increases near the walls where the plume reaches the walls. However the reaction terms of the budgets of the diluted reactive and the product have an important contribution in comparison with the other terms.

Chapter 9

Future work

The simulations performed in this work have considered different channel flow configurations involving heat and mass turbulent transport from discrete and wall sources. These flows are complex because transport of momentum, heat and mass can be coupled and the equations governing the flow depend on various parameters. This type of flow can be easily found in different industrial and environmental applications including combustion, electronic device cooling or atmospheric dispersion.

The results shown in this work were obtained using Direct Numerical Simulations which provides detailed information about the turbulent transport of momentum, heat and mass. However, in real world applications, this type of tools were not often suitable to provide answers due to prohibitive computational requirements. This could be the case of very large Reynolds numbers as those found in atmospheric boundary layer. Keeping this in mind, the future work issues providing continuity to this work, can be summarized as:

- Study the effect of the non-dimensional parameters (Grashof, Reynolds and Prandtl numbers) on the turbulent transfer of quantities for cases B and C. These parameters affect the ratio between the buoyancy force and the viscous force, the ratio between inertial forces and viscous forces and the ratio of momentum and thermal diffusivities, respectively. Probably a parametric study changing the Grashof number would be interesting because it has a main role in the development of the buoyant plume in case C. It is important to note that larger Grashof numbers imply larger computational resources.

- Simulate different chemical reaction mechanisms with or without heat generation effects and implement the dependence of reaction rate and the heat of reaction on temperature. In practice, the heat of reaction and the reaction kinetics constants depend on temperature. This effect can be studied in order to simulate real reactive systems.

- Filter the DNS to study the sub-grid scale effects on the flow and develop and propose subgrid scale (SGS) models for buoyant and/or reactive systems in wall-bounded flows.
- Built a computational atmospheric boundary layer scenario introducing rugosities for different types of terrain to study its effect on the dispersion of reactive contaminants released in the lower atmosphere. This model may allow to introduce different atmospheric conditions and other effects like radiation that can affect the reaction rates. This simulation would require a valid SGS model to simulate flows at very large Reynolds numbers as those found at the atmospheric boundary layer.

From a computational performance point of view, possible improvements for the current CFD code can include:

- Implement an adaptative grid refinement approach to optimize computational resources by using different grid resolutions according with the different multiscale turbulent features involved in the line source dispersion processes. A very fine grid can be used in the regions close to the source where the gradients are larger. This fine grid is embedded in progressively coarser grid levels for locations far from the source where gradients are not so important.
- Implement the multigrid strategy to solve the whole set of transport equations adapting the parallel multigrid solver that is being used for the numerical solution of the Poisson equation for the pressure calculation.

List of notation

C_α	Concentration for species α (mol/m^3)
Cp	Heat capacity $(J/mol\ K)$
Da	Damkhöler number
$\mathcal{D}$	Binary diffusion coefficient (m^2/s)
g_i	Gravity acceleration (m/s^2)
Gr	Grashof number
h	Enthalpy (J/kg)
H_S	Source line size (m)
$J_{\alpha j}$	Molecular flux of species α in the direction j $(mol/m^2 s)$
k	Reaction rate constant (2nd order) $(m^3/s\ mol)$
L	Domain size (m)
M	Mesh length of the turbulence-generating grid (m)
p	Pressure (Pa)
Pr	Prandtl number
r	Reaction rate $(mol/m^3 s)$
R	Universal Constant for gases $(J/mol\ K)$
Re_τ	Reynolds number based on the friction velocity
Sc	Schmidt number
T	Temperature (K)
t	Time (s)
u_τ	Friction velocity (m/s)
V	Volume (m^3)
x_i	Space coordinates in the direction i (m)
x	Spatial coordinates in the streamwise direction (m)
y	Spatial coordinates in the spanwise direction (m)
z	Spatial coordinates in the wall-normal direction (m)
u_i	Velocity component in the direction i (m/s)

u	Streamwise velocity component (m/s)
v	Spanwise velocity component (m/s)
w	Wall-normal velocity component (m/s)
Y_α	Density of species α

Greek letters

α_T	Thermal diffusivity (m^2/s)
β	Thermal expansion coefficient (K^{-1})
δ_{ij}	Kronecker delta
$\Delta\hat{H}_r^0$	Enthalpy of reaction (J/mol)
κ	Thermal conductivity ($W/m\ K$)
μ	Dynamic viscosity ($Pa\ s$)
ν	Kinematic viscosity (m^2/s)
ρ	Density (g/m^3)
τ	Shear stress (Pa)
Φ	Pressure correction (Pa)
ξ	Dissipation function (Pa/s)

Subscripts, superscripts and symbols

$(\ )_{rms}$	Root mean square
$(\ )_\tau$	Refered to u_τ
$(\ )_\alpha$	Refered to species α
$(\ )_n$	Normal direction
$(\ )_w$	Refered to wall
$(\ )^*$	Adimensional quantity
$\overline{(\ )}$	Time-averaged
$(\ )'$	Fluctuation

Bibliography

[1] Ildefonso Cuesta Romeo. *Estudi Numèric de fluxos laminars i turbulents en una cavitat cúbica*. PhD thesis, Escola Tècnica Superior d'Enginyeria Química, Tarragona, 1990.

[2] K. R. Sreenivasan. On local isotropy of passive scalars in turbulent shear flows. *Proc. R. Soc. Lond. A*, 434:165–182, 1991.

[3] B. I. Shraiman and E.D. Siggia. Scalar turbulence. *Nature*, 405:639–646, 2000.

[4] Z. Warhaft. Passive scalars in turbulent flows. *Annu. Rev. Fluid Mech.*, 32:203–240, 2000.

[5] G. I. Taylor. Diffusion by continuous movements. *Proc. Lond. Math. Soc. A*, 20:196–212, 1921.

[6] G. I. Taylor. Statistical theory of turbulence. IV-diffusion in a turbulent air stream. *Proc. R. Soc. Lond. A*, 151:465–478, 1935.

[7] M. S. Uberoi and S. Corrsin. Diffusion form a line source in isotropic turbulence. *Proc. R. Soc. Lond. A*, 151:465–478, 1935.

[8] A. A. Townsend. The diffusion behind a line source in homogeneous turbulence. *Proc. R. Soc. Lond. A*, 224:487, 1954.

[9] Z. Warhaft. The interference on thermal fields form line sources in grid turbulence. *Journal of Fluid Mechanics*, 144:363–387, 1984.

[10] H. Stapountzis, B. L. Sawford, J. C. R. Hunt, and R. E. Britter. Structure of the temperature field downwind of a line source in grid turbulence. *Journal of Fluid Mechanics*, 165:401–424, 1986.

[11] B. L. Sawford and J. R. C. Hunt. Effects of turbulence structure, molecular diffusion and source size on scalar fluctuations in homogeneous turbulence. *Journal of Fluid Mechanics*, 165:373–400, 1986.

[12] M. S. Anand and S. B. Pope. Diffusion behind a line source in grid turbulence. In *4th Symp. on Turbulent Shear Flows*, Karlsruhe, Germany, 1983. Springer.

[13] D. Livescu, F. A. Jaberi, and C. K. Madnia. Passive-scalar wake behind a line source in grid turbulence. *Journal of Fluid Mechanics*, 416:117–149, 2000.

[14] H. Stapountzis and R. E. Britter. Turbulent diffusion behind a heated line source in a nearly homogeneous turbulent shear flow. In *6th Symp. on Turbulent Shear Flows*, Toulouse, France, 1987. Springer.

[15] U. Karnik and S. Tavoularis. Measurements of heat diffusion from a continuous line source in a uniformly sheared turbulent flow. *Journal of Fluid Mechanics*, 202:233–261, 1989.

[16] M. K. Chung and N. H. Kyong. Measurement of turbulent dispersion behind a fine cylindrical heat source in a weakly sheared flow. *Journal of Fluid Mechanics*, 205:171–193, 1989.

[17] J. D. Wilson, T. K. Flesch, and S. E. Waters. Dispersion in sheared gaussian homogeneous turbulence. *Boundary-Layer Met.*, 62:281–290, 1993.

[18] M. S. Cho and M. K. Chung. Application of a reynolds stress/heat flux model to the turbulent thermal dispersion behind a line heat source in a uniformly sheared flow. *Numerical Heat Transfer A-Applications*, 32:715–732, 1997.

[19] D. J. Shlien and S. Corrsin. Dispersion measurements in a turbulent boundary layer. *International Journal of Heat and Mass Transfer*, 19:285–295, 1976.

[20] P. Paranthoen, A. Fouari, A. Dupont, and J. C. Lecordier. Dispersion measurements in turbulent flows (boundary layer and plane jet). *International Journal of Heat and Mass Transfer*, 31:153–165, 1988.

[21] J. E. Fackrell and A. G. Robins. Concentration fluctuations and fluxes in plumes from point sources in turbulent boundary layer. *Journal of Fluid Mechanics*, 117:1–26, 1982.

[22] B. J. Legg, R. M. Raupach, and P. A. Choppin. Experiments on scalar dispersion within a model plant canopy. part iii: an elevated line source. *Boundary-Layer Met.*, 35:277–302, 1986.

[23] S. Veeravalli and Z. Warhaft. Thermal dispersion from a line source in a shearless turbulence mixing layer. *Journal of Fluid Mechanics*, 216:35–70, 1990.

[24] B. M. Bara, D. J. Wilson, and B. W. Zelt. Concentration fluctuations profiles from a water channel simulation of a ground-level release. *Atmos. Environ.*, 26A:1053–1062, 1992.

[25] C. Tong and Z. Warhaft. Passive scalar dispersion and mixing in a turbulent jet. *Journal of Fluid Mechanics*, 292:1–38, 1995.

[26] J. Y. Vincont, S. Simoens, M. Ayrault, and J. M. Wallace. Passive scalar dispersion in a turbulent boundary layer form a line source at the wall and downstream of an obstacle. *Journal of Fluid Mechanics*, 424:127–167, 2000.

[27] S. L. Lyons and T. J. Hanratty. Direct numerical simulation of passive heat transfer in a turbulent channel flow. *International Journal of Heat and Mass Transfer*, 34:1149–1161, 1991.

[28] D. V. Papavassiliou and T. J. Hanratty. Transport of passive scalar in a turbulent channel flow. *International Journal of Heat and Mass Transfer*, 40:1303–1311, 1997.

[29] Y. Na and T. J. Hanratty. Limiting behaviour of turbulent scalar transport close to a wall. *International Journal of Heat and Mass Transfer*, 43:1749–1758, 2000.

[30] K. Kontomaris and T. J. Hanratty. Effect of molecular diffusivity on point source diffusion in the center of a numerically simulated turbulent channel flow. *International Journal of Heat and Mass Transfer*, 37:1817–1828, 1994.

[31] G. Brethouwer, B. J. Boersma, M. B. J. M. Pourquie, and F. T. M. Nieuwstadt. Direct numerical simulation of turbulent mixing of a passive scalar in a pipe flow. *Eur. J. Mech. B/Fluids*, 18:739–756, 1999.

[32] A. J. Vrieling and F. T. M. Nieuwstadt. Turbulent dispersion from nearby point sources-interference of the concentration statistics. *Atmospheric Environment*, 37:4493–4506, 2003.

[33] R. A. Lavertu and L. Mydlarski. Scalar mixing from a concentrated source in turbulent channel flow. *Journal of Fluid Mechanics*, 528:135–172, 2005.

[34] J. Kim and P. Moin. Transport of passive scalars in a turbulent channel flow. In J-C Andre et al., editor, *Turbulent Shear Flows 6*, pages 85–96. Springer-Verlag Berlin, 1989.

[35] D. V. Papavassiliou. Turbulent transport from continuous sources at the wall of a channel. *Journal of Heat and Mass Transfer*, 45:3571–3583, 2002.

[36] D. V. Papavassiliou and T. J. Hanratty. Transport of a passive scalar in a turbulent channel flow. *International Journal of Heat and Mass Transfer*, 40:1303–1311, 1996.

[37] J. D. Li and R. W. Bilger. The diffusion of conserved and reactive scalars behind line sources in homogeneous turbulence. *Journal of Fluid Mechanics*, 318:339–372, 1996.

[38] G. Brethouwer and F. T. M. Nieuwstadt. DNS of mixing and reaction of two species in a turbulent channel flow: A validation of the conditional moment closure. *Flow, Turbulence and Combustion*, 66:209–239, 2001.

[39] P. S. Bernard and A. L. Rovelstad. On the physical accuracy of the scalar transport modeling in inhomogeneous turbulence. *Phys. Fluids*, 6:3093–3108, 1994.

[40] Y. Wang and S. Komori. Application of a second-moment closure model to simulate the turbulent dispersion form an elevated source. *Heat and Mass Transfer*, 34:429–436, 1999.

[41] I. Iliopoulos and T. J. Hanratty. Turbulent dispersion in a non-homogeneous field. *Journal of Fluid Mechanics*, 392:45–71, 1999.

[42] J. Boussinesq. Théorie de l'Écolulement tourbillant. *Mem. Présentés par Divers Savants Acad. Sci. Inst.*, 23:45–50, 1877.

[43] D. Čuturić. Large-eddy simulation of turbulent channel flow significantly affected by buoyancy. Master's thesis, Chalmers University of Technology, Department of Thermo and Fluid Dynamics, Götebörg, Sweden, 2001.

[44] G. Jin and M. Braza. A nonreflecting outlet boundary condition for incompressible unsteady Navier-Stokes calculations. *Journal of Computational Physics*, 107:239–253, 1992.

[45] J. G. Blaschak and G. A. Kriegsmann. A comparative study of absorbing boundary conditions. *Journal of Computational Physics*, 77:109–139, 1988.

[46] F. H. Harlow and J. E. Welch. Numerical calculation of time-dependent viscous incompressible flow of fluid with free surface. *Physics of Fluids*, 8:2182–2189, 1965.

[47] S. V. Patankar. Series in computational methods in mechanics and thermal sciences. Mc Graw Hill, 1980.

[48] S. V. Patankar and D. B. Spalding. A calculation procedure for heat, mass and momentum transfer in three-dimensional parabolic flows. *International Journal of Heat and Mass Transfer*, 15:1787–1805, 1972.

[49] R. I. Issa. Solution of the implicit discretised fluid flow equations by operator-splitting. *Journal of Computational Physics*, pages 66–82, 1986.

[50] A. A. Amsden and F. H. Harlow. The SMAC method: A numerical technique for calculating incompressible fluid flows. Technical report LA-4370. Technical report, Los Alamos Scientific Laboratory, 1970.

[51] M .Braza. *Simulation numérique du décollement instationnaire externe par une formulation vitesse-pression. Application à l'écoulement autour d'un cylindre*. PhD thesis, Institut National Polytechnique de Toulouse, 1981.

[52] M. Braza, P. Chassaing, and H. Ha Minh. Numerical study and physical analysis of the pressure and velocity fields in the near wake of a circular cylinder. *Journal of Fluid Mechanics*, 165:79–130, 1986.

[53] J. B. Cazalbou. *Développement d'un code de calcul d'écoulements tridimensionnels instationnaires. Application à l'analyse physique de phénomènes de*

convection et d'instabilité. PhD thesis, Institut National Polytechnique de Toulouse, 1981.

[54] Joel H. Ferziger and Milovan Perić. *Computational Methods for Fluid Dynamics*. Springer-Verlag, third edition, 2002.

[55] B. P. Leonard. The ULTIMATE conservative difference scheme applied to unsteady one-dimensional advection. *Computer Methods in Applied Mechanics and Engineering*, 88:17–74, 1991.

[56] Barry Koren. A robust upwind discretization method for advection, diffusion and source terms. Technical report, Centrum voor Wiskunde en Informatica, 1993.

[57] B. P. Leonard, M. K. MacVean, and A. P. Lock. Positivity-preserving numerical schemes for multidimensional advection. *NASA Technical Memorandum 106055*, 1993.

[58] M. Vázquez, M. Ravachol, F. Charlot, and M. Mallet. The robustness issue on multigrid schemes applied to the navier-stokes equations for laminar and turbulent, incompressible and compressible flows. *International Journal for Numerical Methods in Fluids*, 45:555–579, 2004.

[59] P. Wesseling and C. W. Oosterlee. Geometric multigrid with applications to computational fluid dynamics. *Journal of Computational and Applied Dynamics*, 128:311–334, 2001.

[60] M. F. Paisley. Multigrid solution of the incompressible navier-stokes equations for density-stratified flow past three-dimensional obstacles. *Journal of Computational Physics*, 170:785–811, 2001.

[61] K. Morgan K. Sørensen, O. Hassan and N. P. Weatherill. A multigrid accelerated time-accurate inviscid compressible fluid flow solution algorithm employing mesh movement and local remeshing. *International Journal for Numerical Methods in Fluids*, 43:517–536, 2003.

[62] E. F. F. Botta and F. W. Wubs. Convergence behaviour of iterative methods on severely stretched grids. *International Journal for Numerical Methods in Engineering*, 36:3333–3350, 1993.

[63] William L. Briggs, Van Emden Henson, and Steve F. McCormick. *A Multigrid Tutorial*. SIAM, second edition, 2000.

[64] H. A. Van Der Vorst. Bi-CGSTAB: A fast and smoothly converging variant of Bi-CG for the solution of non-symmetric linear systems. *J. Sci. Stat. Comput.*, 3:631–644, 1992.

[65] R. Freund and N. Nachtigal. QMR: A quasi-minimal residual method for non-hermitian linear systems. *Numer. Math.*, 60:315–339, 1991.

[66] U. Trottenberg, C. Oosterlee, and A. Schller. *Multigrid*. Academic Press, 2001.

[67] C. Millar and J. R. Warling A. Asenov. Excessive over-relaxation method for multigrid poisson solvers. *Journal of Computational Electronics*, 1:1–5, 2002.

[68] I. M. Llorente and N. D. Melson. Robust multigrid smoothers for three dimensional elliptic equations with strong anisotropies. Technical report, NASA/ICASE, 1998.

[69] W. H. Press, B. P. Flannery, S. A. Teukolsky, and W. T. Vetterling. *Numerical Recipes in Fortran*. Cambridge University Press, second edition, 1992.

[70] K. Iwamoto. Database of fully developed channel flow. Technical report, The University of Tokyo, 2002.

[71] B. L. Sawford and P. J. Sullivan. A simple representation of a developing contaminant concentration field. *Journal of Fluid Mechanics*, 289:141–157, 1995.

[72] R. Moestam and L. Davidson. Numerical simulations of a thermocline in a pressure-driven flow between two infinite horizontal plates. *Physics of Fluids*, 17:075109(1)–075109(8), 2005.

[73] L. Davidson, D. Čuturić, and S. Peng. DNS in plane vertical channel with and without buoyancy. *Turbulence, Heat and Mass Transfer*, 4:401–408, 2003.

[74] B. P. Leonard. A stable and accurate convective modeling procedure based on quadratic upstream interpolation. *Computer Methods in Applied Mechanics and Engineering*, 19:59–98, 1979.